Assessment of Reactivity Equivalence for Enhanced Accident Tolerant Fuels in Light Water Reactors

A Dissertation Presented for the
Doctor of Philosophy
Degree
The University of Tennessee, Knoxville

Nathan Michael George
May 2015

Copyright © 2015 by Nathan Michael George
All rights reserved.

ABSTRACT

The neutronic behavior of accident tolerant fuel (ATF) concepts was simulated in light water reactors (LWRs) to establish design parameters to match reactivity lifetime requirements of standard UO_2 [uranium dioxide]/Zircaloy fuel. The two concepts discussed in this dissertation are fully ceramic micro-encapsulated (FCM) fuel and alternate cladding concepts. To compare the required fuel alterations against standard UO_2/Zircaloy fuel, a 2D lattice-physics based reactivity equivalence method was established to estimate excess reactivity at the completion of each weighted batch cycle.

In the case of FCM fuel, the uranium-based tristructural isotropic (TRISO) kernel and the surrounding particle layers/matrix material were altered to increase fissile loading. To match the lifetime of an 18-month pressurized water reactor (PWR) cycle, the FCM particle fuel design required roughly 10% additional fissile material at beginning of life (BOL) compared with that of a standard UO_2 rod.

When investigating alternate cladding concepts, cladding walls were thinned with the outer diameter unchanged, so the pellet volume and enrichment of UO_2 fuel were increased. In the PWR study, a cladding thickness of 350 μm [micrometer] was simulated. Austenitic stainless steels required an increase of about 0.5 wt % enrichment to match fuel cycle requirements, while the required increase in enrichment for FeCrAl was about 0.1%. Due to the presence of the channel box, the boiling water reactor (BWR) ATF designs required additional fissile material. With the FeCrAl cladding and channel box thicknesses halved, it was estimated that an average enrichment increase of 0.6% would be required. Verification of the 2D reactivity results was performed with a 3D full-core parametric study of a representative BWR demonstrating the applicability of the 2D reactivity equivalence method for the cases herein studied.

A LWR optimization code (LWROpt) was used to determine loading (LP) and control blade (CB) patterns for the ATF BWR concepts, so to help regain thermal and reactivity margins. Fuel performance was investigated with the BISON-CASL code using linear heat rate data from the optimized full-core results. The analysis demonstrated that varying power histories between FeCrAl and Zircaloy cladding significantly affect thermal expansion and centerline temperatures of the fuel rods.

TABLE OF CONTENTS

I. Introduction 1

Fully Ceramic Micro-encapsulated Fuel 1

Alternate Cladding Concepts in PWRs 2

Alternate Cladding Concepts in BWRs 3

II. Literature Review 6

History of Light Water Reactor Cladding 6

Fully Ceramic Micro-Encapsulated Fuel 7

Particle Layer Interaction 8

Thermal Conductivity 10

Alternate Cladding Concepts 12

Austenitic Alloys 12

Ferritic Alloys 13

Silicon Carbide 15

Fuel Performance Modeling 16

Reactor Physics Modeling and Simulation 17

Lattice Physics 18

Parametric Analysis 19

3D Full Core Simulators 19

III. PWR Methodology and Design Parameters 21

Pin Cell and Lattice Physics Modeling 21

Reactivity-Equivalent Physical Transformation for TRISO Fuel 23

Alternate Cladding Input Parameters 24

Lattice-Physics Based EOC Reactivity Equivalence Methodology 26

IV. BWR Methodology and Design Parameters 29

Lattice Physics Models 29

End of Cycle Reactivity Calculations 31

Full-Core BWR Simulations 35

Lattice Physics Cross-section Generation 35

NESTLE Neutronics Model 38

Alternate Cladding Full-Core Parametric Study....43
Loading and Control Blade Pattern Optimization....44
NESTLE Thermal Hydraulics Parameters....48
Fuel Performance Model....49
Coupling BISON-CASL and NESTLE....50
BISON-CASL Simulations of FeCrAl and Zirconium....50
V. PWR Results....54
Preliminary Pin Cell Calculations....54
Assessment of Insufficient Reactivity in FCM Fuel....54
Reactivity Penalty of Alternate Cladding Concepts....56
Parametric Study Matching Reactivity Lifetime Requirements....58
FCM Particle Geometry Manipulation....58
Modifications of Alternate Cladding Thickness and Fuel Enrichment....61
Spectral Results....65
FCM Fuel Spectra Evaluation....65
Alternate Cladding Spectral Hardening....68
Reactivity Coefficients....69
FCM Lattice Power Peaking Calculations....71
VI. BWR Results....74
Preliminary BWR Lattice Physics Results....74
Two-Dimensional Parametric Study....77
Full-Core BWR Models....80
Shuffle and Control Blade Optimization....85
Hybrid SiC/FeCrAl Core....92
Fuel Performance Results....94
Fuel Rod Power History Calculations....94
BISSON-CASL Results....97
VII. Conclusion/Future Work....100
References....103
Appendix....107

Appendix A – Sample 10 × 10 BWR Lattice Physics SCALE Input 108
Appendix B – Representative BWR NESTLE Input 114
Appendix C – Sample LWROpt Input 121
Vita 124

LIST OF TABLES

Table I. Density and Microscopic Thermal Neutron Absorption [3] 2
Table II. Cladding Compositions Used for Fuel Reactivity Calculations 25
Table III. Various Rod Geometries used for Reactivity Calculations 25
Table IV. Assumed Batch-dependent Assembly Counts, Core Volume Fractions, Relative Assembly Powers, and EFPD for a Typical Westinghouse PWR 26
Table V. Assumed Batch-dependent Assembly Counts, Core Volume Fractions, Relative Assembly Powers, and EFPD for a Typical General Electric BWR 34
Table VI. Branch Perturbation Specifications used in CASMO-4 38
Table VII: Control Blade Optimization Design Limits 47
Table VIII. Core properties for NESTLE BWR model 48
Table IX: Fuel performance geometry specifications 52
Table IX. Fuel Cycle Reactivity Models 59
Table X. Cycle Reactivity Difference [Δk_{core}] for Alternate Fuel Cladding Concepts from the Reference PWR Fuel with Zircaloy-4 Cladding 62
Table XI. ^{235}U Enrichment Matching Cycle Length Requirements 63
Table XII. Cladding Thickness Matching Cycle Length Requirements 64
Table XIII. Reactivity Safety Coefficient Perturbations in Moderator 70
Table XIV. Moderator Temperature Coefficient Map Throughout Depletion (pcm $\Delta\rho$/°F) with an 18° F Change in Coolant Temperature 70
Table XV. Full-core BWR Specifications for Zircaloy Base Case 82
Table XVI: Enrichment Requirements for Hybrid BWR Design 94

LIST OF FIGURES

Figure 1: Progression of BWR Analysis 5
Figure 2: TRISO fuel particle geometry [1] 7
Figure 3: Mechanical stresses induced on PV by surrounding PyC layers [15] 9
Figure 4: Irradiation induced failure of TRISO fuel layers [15] 10
Figure 5: Thermal conductivity of NITE-based SiC for FCM fuel matrix [12] 11
Figure 6: FCM Fuel rod temperature distribution 12
Figure 7: Arrhenius plot of the parabolic rate constants [20] 14
Figure 8: Comparison of creep rupture strengths of iron alloys 15
Figure 9: Westinghouse 17 × 17 PWR pin cell model 21
Figure 10: Westinghouse 17 × 17 PWR lattice model, with independent depletion mixtures indicated by different colors in the fuel pins 23
Figure 11: Reactivity-equivalent physical transformation process 24
Figure 12: Assumed PWR core configuration of batch-specific loading pattern 26
Figure 13: Infinite multiplication factor vs. effective full power days for various cladding materials in standard PWR 17 × 17 rod geometry 28
Figure 14: Modern 10 × 10 BWR lattice modeled with TRITON [44] 29
Figure 15: Hybrid SiC channel box design 31
Figure 16: Allocation of Lattices within BWR Fuel Bundle 32
Figure 17: General Electric BWR Quarter Core Exposure Map [47] 33
Figure 18: Relative Axial Power from Peach Bottom Tip Data 35
Figure 19: Axial zone parameters of modern 10 × 10 BWR bundle 36
Figure 20: a) Radial Exposure Map of Representative BWR Core in units of MWd/MTU, b) Hot Axial Power Profile of DOM Region 41
Figure 21: Axial zone configuration per bundle type 42
Figure 22: Assembly Configuration Optimization 43
Figure 23: Loading pattern optimization GUI 46
Figure 24: Control blade bank locations 47
Figure 25: Mesh of smeared pellet fuel rod model with 300 μm cladding 51
Figure 26: Infinite Multiplication factor vs effective full-power days for a range of UO2 kernel diameters 55
Figure 27: Infinite Multiplication factor with alternative uranium-based FCM fuels 56
Figure 28: Δk-infinity from Zircaloy-4 clad fuel vs. effective full power days 57
Figure 29: EOC net core reactivity vs kernel diameter for several PFs and BLs 59
Figure 30: EOC net core reactivity vs initial fissile fraction 60
Figure 31: Fuel parameters required to match the PWR lifetime 65
Figure 32: Average scalar flux throughout fuel lifetime: BOL (a), MOL (b), and EOL (c) 67
Figure 33: Neutron flux spectrum at BOL 68

Figure 34: Uranium mononitride FCM fuel power-sharing color-set 73
Figure 35: Standard PWR UO2 pellet-based fuel power-sharing color-set 73
Figure 36: Δk-infinity from Zircaloy-4 cladding and channel box for FeCrAl and SiC 75
Figure 37: FeCrAl reactivity penalty of individual fuel elements 76
Figure 38: Neutron flux spectrum as a function of energy 77
Figure 39: EOC Reactivity Values with respect to Fuel Design Changes in FeCrAl Loaded Bundles 79
Figure 40: Fuel parameters required to match the BWR lifetime 80
Figure 41: Full-core Zircaloy base case depletion 81
Figure 42: FeCrAl loaded core designs matching Zircaloy base case cycle length 83
Figure 43: Parametric evaluation of lattice physics and full-core models 84
Figure 44: CB withdrawal in notches for Zircaloy base case core 86
Figure 45: Relative power fraction of Zircaloy base case model at a) BOC b) EOC 87
Figure 46: Loading pattern optimizations for FeCrAl core with varying RPF limits 88
Figure 47: FeCrAl loading pattern with a) optimization code b) python GUI 89
Figure 48: Control blade withdrawal in notches for FeCrAl core 91
Figure 49: Bundle-averaged axial void distribution at MOC 92
Figure 50: Δk-infinity from Zircaloy-4 cladding and channel box for hybrid bundles 93
Figure 51: Equilibrium core exposure values for Zircaloy base case model 95
Figure 52: CASMO BOL pin cell relative peaking factors 96
Figure 53: Axial linear heat rate for limiting Zircaloy assembly through first cycle 96
Figure 54: Peak centerline temperature 98
Figure 55: Axial displacement throughout depletion 98
Figure 56: Radial displacement throughout depletion 99

ABBREVIATIONS

ATF	Accident tolerant fuel
BL	Buffer layer
BOC	Beginning of cycle
BOL	Beginning of life
BWR	Boiling water reactor
C2N	CASMO to NESTLE
CB	Control blade
DFM	Drift flux model
DH	Double heterogeneous
EFPD	Effective full power day
EOC	End of cycle
EOL	End of life
FCM	Fully ceramic micro-encapsulated
GE	General Electric Co.
GUI	Graphical user interface
GWd	Giga-watt day
HEM	Homogeneous equilibrium mixture
ID	Inner diameter
KD	Kernel diameter
LEU	Low-enriched uranium
LP	Loading pattern
LWR	Light water reactor
LWROpt	Light Water Reactor Optimization
MOC	Middle of cycle
MOL	Middle of life
MTC	Moderator temperature coefficient
MTU	Metric ton of uranium
MW	Mega-watt
MWd	Mega-watt day
NIST	National Institute of Standards and Technology
NITE	Non-infiltration and transient eutectic-phase
OD	Outer diameter
OF	Objective function
ORNL	Oak Ridge National Laboratory
PCI	Pellet cladding interaction
PF	Packing fraction
PV	Pressure vessel
PWR	Pressurized water reactor
RPF	Relative power fraction
RPT	Reactivity physical transformation
TIP	Traversing in-core probe
TRISO	Tristructural isotropic

I. INTRODUCTION

This dissertation investigates the utilization of ATFs in LWR systems. Advanced fuel candidates include: FCM fuel and alternate cladding concepts. Both candidates were examined to replace standard Zircaloy/UO_2 pellet fuel rods currently employed in all United States commercial reactors. FCM fuel and alternate cladding simulated in PWRs were modeled with 2D lattice physics codes. However more extensive research was performed on BWRs, concluding with full-core optimization in a 3D nodal simulator. The following sections describe in detail the significance of each individual study and how it pertains to the nuclear industry.

I.A. Fully Ceramic Micro-Encapsulated Fuel

Neutronic analysis was performed on TRISO particle fuel in a PWR environment. The study presents work completed in developing FCM-based PWR fuel lattice designs that perform similarly to that of current Westinghouse 17 x 17 UO_2 fuel elements with respect to reactivity, pin peaking, and power sharing factors [1]. The two-dimensional neutron transport code NEWT, from the SCALE software system, was the primary analysis tool used to model the lattice designs.

From a neutronics standpoint, modeling TRISO particle fuel presents various challenges in that the overall uranium density per unit volume in the core is significantly less than standard UO_2 pellet fuel. Due to particle packing fraction (PF) and physical density limits, as described in later sections, it was established early in the study that the TRISO particles would require enrichments in the upper end of the low enriched uranium envelope. Accordingly, 19.75% ^{235}U enrichment was assumed during the course of the study. Thus, modifications were made to the particle geometry and insertion of an alternative fuel form was investigated to increase fissile material the design and achieve three 18-month cycles of operation. A method for estimating the end of cycle (EOC) reactivity was implemented to compare each model to standard UO_2 pellet fuel.

In addition to the analysis done on reactivity lifetime requirements, the neutron spectrum throughout the fuel lifetime was investigated to observe any possible spectral hardening from the large enrichment deviation between FCM and standard pellet fuel. Finally, on a lattice level,

relative pin peaking factors and assembly power sharing were analyzed. Creating a fresh-feed–once-burned checkerboard color-set, multiple lattices were modeled to simulate adjacent assemblies with varying exposures.

I.B. Alternate Cladding Concepts in PWRs

Maintaining a focus on ATFs, a study was performed to neutronically simulate alternate fuel cladding concepts in PWR cores. The study focused on silicon carbide options (SiC/SiC composite) as well as specific iron-based options austenitic steels (310SS and 304SS) and ferritic steels (FeCrAl and APMT^{TM}) [2]. These cladding materials were compared with the reference zirconium alloy clad fuel pins using results from lattice physics depletion calculations.

Table I lists the microscopic thermal absorption cross sections that correspond to each alternate cladding material investigated. Materials with higher absorption properties are expected to have a greater effect on neutron economy as more neutrons are absorbed in the cladding before being captured in the UO_2 fuel region. Although the absorption properties of a given material are dependent on neutron energy, average thermal cross sections are representative of neutron energies after they have been slowed down by the moderator, which is the energy range where most fission reactions occur in a PWR.

Table I. Density and Microscopic Thermal Neutron Absorption [3]

Material	Density (g/cm^3)	Microscopic thermal neutron absorption cross section (barns)
Zircaloy	6.56	0.20
304SS	7.9	2.86
310SS	8.03	3.21
FeCrAl	7.1	2.43
APMT^{TM}	7.3	2.47
SiC	2.58	0.086

Due to the neutronic penalties associated with the higher absorbing materials, a parametric study was performed to determine the geometric conditions required to match cycle length requirements for each alternate cladding concept in a PWR. Perturbations to the cladding thickness as well as enrichment of the UO_2 fuel were investigated to increase the loading of fissile material in the design. A similar reactivity model as mentioned in the FCM study was used once again to compare each alternate cladding geometry/material change to that of standard Zircaloy-4 cladding. This methodology in addition to the specified input parameters associated with each cladding material will be discussed later in detail.

In keeping with the safety standards of operational PWRs, it is imperative that each cladding material maintain negative moderator temperature and void coefficients. Therefore, the study analyzed moderator temperature coefficients (MTC) and void fraction at BOL, middle (MOL) and end of life (EOL). Due to the hardening of the neutron spectrum that was discovered early on in the study when employing the iron-based alternate cladding materials, plutonium inventory was also investigated for each cladding concept.

I.C. Alternate Cladding Concepts in BWRs

Considering the high amount of steam present, the necessity for less oxidizing safety systems in BWRs is even greater than PWRs. Work has been done recently at Oak Ridge National Laboratory (ORNL) investigating the implementation of alternate fuel cladding in BWR systems. Iron-based/SiC cladding reacts with steam to produce free hydrogen at a much slower rate than Zircaloy. Use of these cladding materials would have mitigated hydrogen production during the accident at Fukushima Daiichi and may have prevented the explosions that ruined the reactor building and released radioactive material. However even iron-based/SiC cladding materials would likely have been unable to prevent core melting at such accident conditions. This dissertation develops the lattice physics simulation of advanced ATF BWR fuel bundles leading up to full-core modeling and optimization with the nodal diffusion code NESTLE.

It was considered early on that the cladding geometry alterations and enrichment levels required for 310SS, 304SS and APMT^{TM} to meet lifetime requirements of Zircaloy fuel were prohibitively high for commercialization. This is due to the higher neutron absorbing elements within these alloys; which in turn produce large neutronic penalties under normal operating conditions. Because of this, FeCrAl and SiC were of primary interest when modeling alternate cladding concepts in BWRs. The majority of fuel bundles modeled consisted of FeCrAl cladding and channel box. Despite various manufacturing concerns with SiC cladding, the material remains a strong candidate for the channel box. Therefore a side study was performed with FeCrAl cladding in combination with a SiC channel box. To improve the resistance to water corrosion, the SiC was layered with Ni and Cr.

In order to check the validity of each design on a material basis, the fuel performance of the alternate cladding was analyzed. Although a design might be considered neutronically optimized (with a given cladding material, enrichment and geometric specification), if the combination of materials involved are prone to failure during normal or accident scenarios, then the optimization process must be re-evaluated. Therefore, results from the fuel performance code, BISON-CASL will prove to be an added validation tool in analyzing the alternate cladding material.

Modeling an entire reactor requires many steps leading up to the full-core model. The following flow chart describes the progression of simulations throughout the BWR analysis. Each process performed along with the respective modeling shown in Figure 1 will be described in detail in the methodology section.

In accordance with Figure 1, lattice physics calculations were run first in order to obtain few-group cross-sections. Those cross-sections were then post-processed in a way that the nodal diffusion simulator can interpret them. After the full-core model was established, optimization of the core loading and CB patterns was performed to maximize cycle length and reduce power peaking all while maintaining criticality. Lastly, once the limiting fuel cells and bundles were established by the lattice physics and full-core models, the fuel performance of the limiting fuel rod was analyzed.

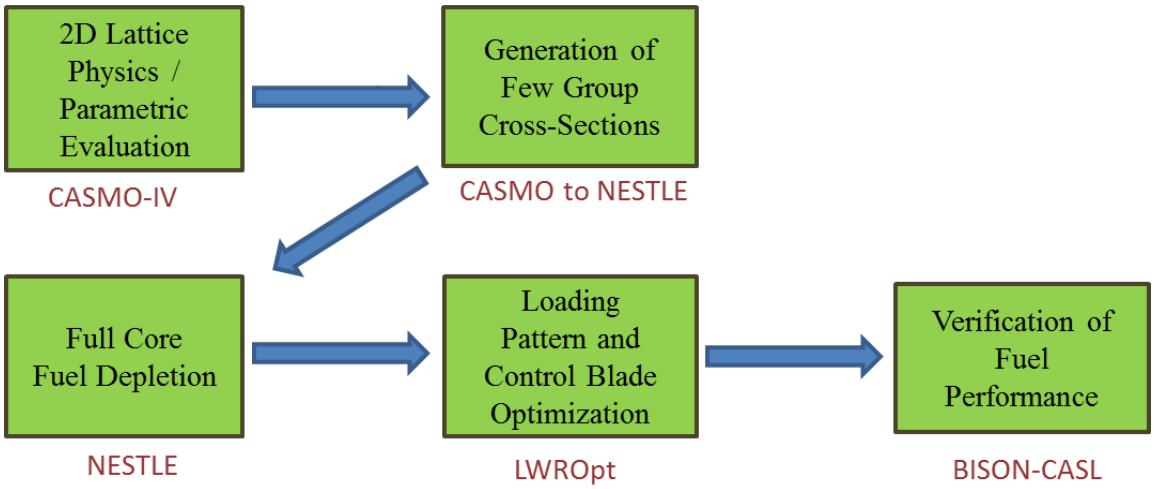


Figure 1: Progression of BWR Analysis

II. LITERATURE REVIEW

II.A. History of Cladding in Light Water Reactors

The United States has produced clean nuclear energy since the first power plant went critical in Shippingport, PA in 1957 [4]. Shippingport and nearly all other commercial plants that have operated in the US since then have been LWRs. These include PWRs and BWRs which use H_2O to cool and moderate the fuel rods in the reactor core. LWR fuel rods consist of UO_2 pellets that are surrounded by a protective cladding material. Representing the first line of defense, the cladding encapsulates dangerous radioactive fission products that accumulate after every fission reaction. In the 1950's, the US Navy Nuclear Propulsion program began using a zirconium-based alloy (Zircaloy) due to its excellent thermal conductivity, ability to withstand heavy neutron irradiation, and low propensity to absorb neutrons [2]. Since then, the vast majority of commercial reactors operating in the United States have used Zircaloy for the cladding material, spacer grids, and channel boxes (for BWRs).

Because of zirconium's poor oxidation qualities in the environment of high-temperature steam, stainless steel was investigated and utilized as an alternative cladding material in five U.S. LWRs up until the 1990s. The use of stainless steel reduced, but did not eliminate the problem of hydrogen generation [5]. Also, due to the higher absorption properties of these iron-alloys, the steel cladding was a detriment to the neutron economy in the core. After fuel cladding damage was discovered at Haddam Neck Plant, stainless steel cladding was no longer used in U.S. nuclear reactors [5]. Today all commercial U.S. nuclear plants operate with zirconium-based alloys for fuel rod cladding.

In March of 2011, Japan experienced a massive earthquake and tsunami causing total station blackouts, loss of coolant accidents and multiple core meltdowns at the Fukushima Daiichi BWR site located on the eastern shore of Japan. During the accident, the diesel generators that are used to pump backup coolant into the core were flooded and failed, causing the zirconium fuel rods to dramatically heat up and oxidize with the surrounding steam [6]. This oxidation process caused large amounts of hydrogen gas to accrue and eventually ignite producing dramatic explosions.

During the event, a large amount of radioactivity was released into both the atmosphere and the Pacific Ocean [6]. Although there have been zero deaths thus far linked to radioactive exposure from the incident, decommissioning of the facility is expected to take up to 30 to 40 years [7].

Since the event three years ago, ATF research has been given high priority by many scientific organizations around the world. National labs have been investigating innovative fuel designs that meet neutronic performance standards of UO_2 pellet fuel and perform safer under severe accident scenarios. However, before utilities consider changing out UO_2/Zircaloy fuel bundles that have operated exceptionally for 60 years, ATFs must not only be able to match reactivity lifetime requirements, but also satisfy the same safety and performance standards UO_2 pellet fuel has been licensed to meet.

II.B. Fully Ceramic Micro-Encapsulated Fuel

A recent concept for an innovative fuel form for use in LWRs has been proposed based on TRISO fuel particles embedded in a silicon carbide matrix. This fuel form is known as FCM fuel [1, 8]. TRISO fuel has been utilized previously in high temperature gas reactors and employs multiple barriers to prevent fission product release. A graphical representation of a TRISO fuel particle is shown in Figure 2.

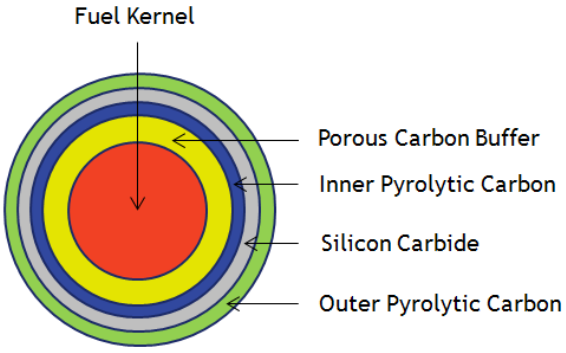


Figure 2: TRISO fuel particle geometry [1]

As shown in Figure 2, the particle consists of a uranium-bearing fuel kernel, typically uranium oxycarbide (UCO) or uranium mononitride (UN), surrounded by several layers of pyrolytic carbon (PyC) and silicon carbide (SiC). A porous carbon buffer surrounding the kernel attenuates fission fragments undergoing recoil release from the fuel kernel and accommodates internal gas buildup and dimensional changes. The outer layers consist of an inner PyC (IPyC) layer, a SiC layer, and an outer PyC (OPyC) layer. The PyC layers are dense pyrolytic carbon, typically about 90% of their theoretical density. The SiC layer acts as the main pressure vessel (PV) and provides a diffusion barrier to prevent fission product release from the particle. The PyC layers protect the SiC layer from chemical corrosion during TRISO particle irradiation and act as additional diffusion barriers to fission products, and the IPyC also protects the fuel kernel from corrosive gases used to deposit the SiC layer [9-11]. The TRISO fuel particles are surrounded by a SiC matrix; this combination of TRISO particles in a SiC matrix constitutes the FCM fuel concept.

The SiC matrix provides various advantages to traditional fuel that include: increased thermal conductivity, radiation damage resistance, environmental stability, and proliferation resistance [8]. As previously mentioned, oxidation of zirconium cladding is of major concern under accident scenarios of LWRs. The SiC matrix employed in FCM fuel is very resistant to oxidation by high-temperature steam, and is anticipated to reach high burnups under normal operating conditionals as well as accident scenarios [12].

II.B.1 Particle Layer Interaction

Arguably the strongest quality of FCM fuel is its ability to entrap dangerous fission products such as ^{131}I and ^{137}Cs within its multiple barrier design. The enclosure of these fission products is reliant on the material performance of each particle layer. Although there are four layers surrounding the fuel kernel, failure of the SiC PV layer almost always leads to complete failure of the particle. Therefore it is important to understand the inner workings of each layer, how it interacts with the PV, as well as the mechanisms that can lead to possible failure.

Although materials in the fuel region of a reactor will undergo irradiation from betas, alphas and other fission products, the majority of irradiation damage will come from the heavy neutron flux.

Neutrons traversing through a material have the potential to knock off surrounding atoms from their lattice sites causing a cascade of collision events leading to large defects in the material [13]. The accumulation of defects causes a densification process followed by swelling in the material and in turn causes a higher likelihood of failure [14].

In addition to the neutron irradiation environment, gas pressure in the particle increases from the arrival of gaseous fission products in the fuel kernel. As oxygen molecules from UCO react with carbon from the buffer and IPyC layers, CO and CO_2 gas begin to form. These added gas pressures push on the IPyC region causing stress on the SiC layer. The largest contribution of stress and strain on the PV however is from shrinkage and swelling of the PyC layers. Figure 3 illustrates the forces acting on the SiC layer which can cause eventual particle failure [10].

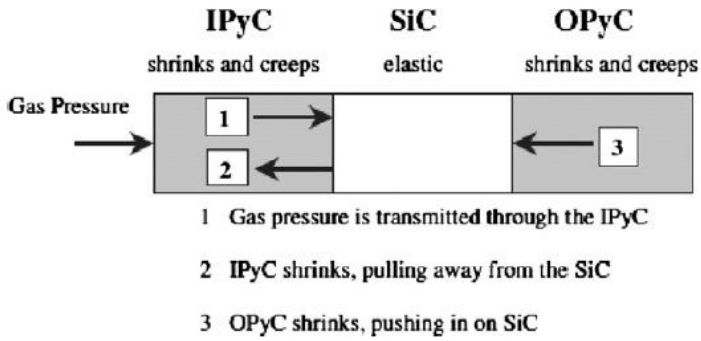


Figure 3: Mechanical stresses induced on PV by surrounding PyC layers [15]

As PyC is exposed to heavy neutron irradiation, a densification process first occurs. When voids begin to arise from vacancy accumulation, the material begins to swell. Once the tensile stress on the SiC layer from these forces exceeds that of its fracture strength, the PV will rupture. Figure 4 shows a crack propagating through a TRISO particle from the fuel kernel all the way through the SiC layer [15]. Since three of four layers have been compromised, if the particle was exposed to anymore irradiation, it would likely fail and release gaseous fission products.

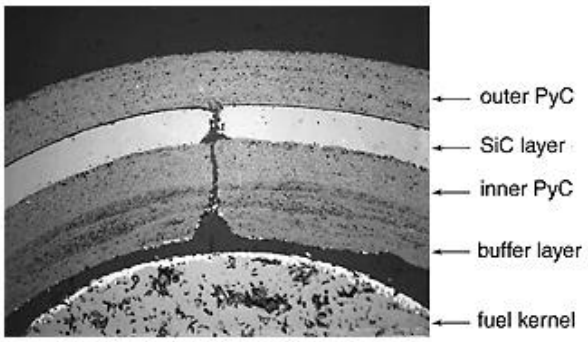


Figure 4: Irradiation induced failure of TRISO fuel layers [15]

II.B.2 Thermal Conductivity

The production of the FCM matrix is based on a non-infiltration and transient eutectic-phase (NITE) technology. High density, unirradiated NITE SiC displays excellent thermal conductivity properties compared to that of a UO_2 fuel pellet. Also, the addition of embedded TRISO particles has been shown to have little or no effect on the conductivity of the matrix. A wide range of conductivity values is found upon irradiation of the material as well as fluctuations in temperature. Figure 5 represents the thermal conductivity of unirradiated and irradiated NITE SiC compared to UO_2 and Zr metal as a function of temperature [12]. After irradiation, the thermal conductivity of NITE SiC is significantly higher than that of UO_2 at representative LWR temperatures.

When employing particle fuel in LWR systems, the overall fuel volume is dramatically decreased compared to standard UO_2 pellet fuel. UN has been utilized due to its higher heavy metal density than UO_2. Therefore, the thermal conductivity of UN was also used when determining an overall homogenized thermal conductivity in the FCM RELAP model.

Figure 6 is a visual representation of the temperature distribution found in both systems. Using the RELAP model, temperature was outputted radially at five different axial locations of the fuel channel. From here, a modified MATLAB script was used to visually display each axial slice.

The bulk coolant temperature for the model was set to 560 K which was used as an initial boundary condition.

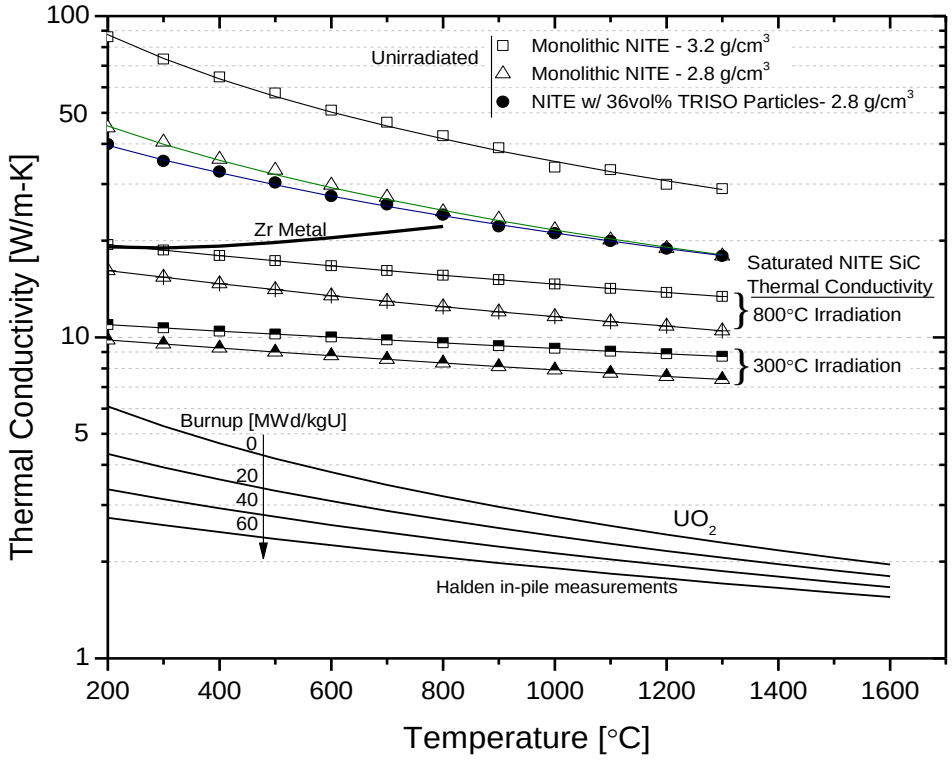


Figure 5: Thermal conductivity of NITE-based SiC for FCM fuel matrix [12]

Figure 6 clearly demonstrates how the centerline fuel temperature is significantly lowered when replacing UO_2 pellet fuel rods with FCM fuel. It is important to note that these models were done with thermal conductivity values at zero exposure and are also representative of one fuel rod channel and not an entire fuel lattice.

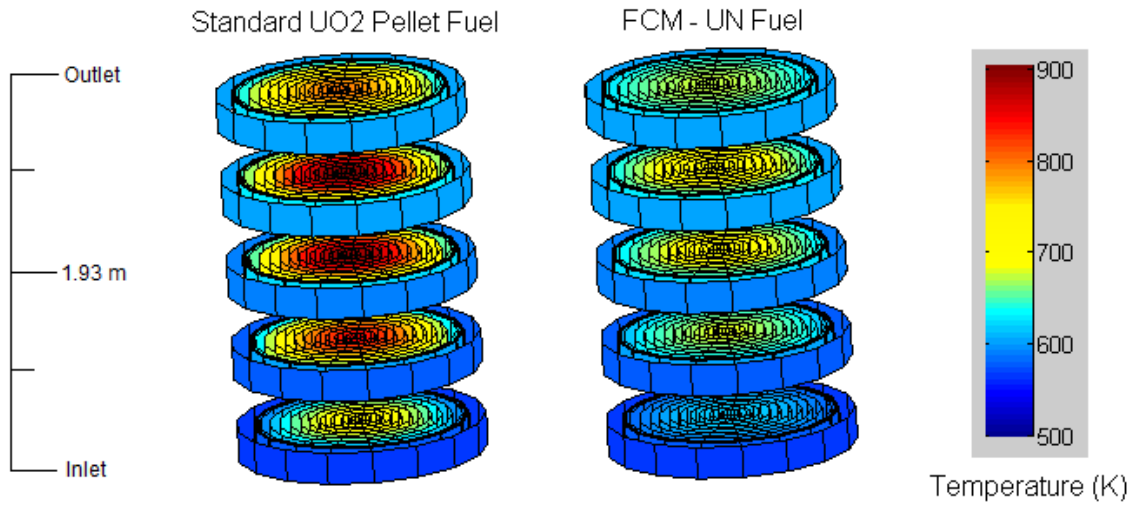


Figure 6: FCM Fuel rod temperature distribution

II.C. Alternate Cladding Concepts

In a LWR system, the onset of physical and chemical degradation phenomena takes place at temperatures above approximately 800°C, where zirconium alloy fuel cladding balloons and bursts [16]. As the core temperature increases, oxidation of the cladding and high temperature steam accelerates core degradation processes [17].

Since Fukushima, major efforts have been put forth to investigate the usage of alternate cladding materials in LWRs. A few of the candidate concepts include austenitic and ferritic alloys as well as SiC/SiC composite cladding. These materials have the ability to significantly reduce oxidation kinetics in high temperature steam environments when compared to zirconium alloys, which in turn could reduce heating and hydrogen generation rates [18-21].

II.C.1 Austenitic Alloys

The austenitic cladding concepts include alloys such as 310SS and 304SS. Type 304SS represents the generic 18Cr-8Ni type used in the early decades of nuclear energy until the 1990s

[22]. Although 304SS was abandoned in U.S. reactors because of its high absorption properties, and damage found in the Haddam Neck Plant, major performance improvements have been made in the past few decades on iron-based cladding concepts for nuclear fuel applications.

Type 310SS is a newer alloy that contains higher amounts of chromium and nickel. The additional chromium allows for a protective layer of Cr_2O_3 to form around the rod which retards cladding oxidation in the environment of high temperature steam [19]. 304SS which contains significantly less chromium and more iron than that of 310SS, maintains higher permeability properties of iron oxide, and is thus similar to zirconium alloys that form zirconium oxides in the presence of high temperature H_2O [20]. The large amounts of Ni, Cr and Fe within these alloys contribute to their high neutron absorption properties.

II.C.2 Ferritic Alloys

Ferritic alloys, FeCrAl and commercial APMT^{TM} contain significant amounts of aluminum which, under high temperature oxidation conditions, produces a protective Al_2O_3 layer that is even stronger than that formed in austenitic steals [20]. Similar to Cr_2O_3, Al_2O_3 is less permeable than ZrO_2, making its oxidation properties considerably stronger in the presence of high temperature steam.

Figure 7 plots the parabolic rate constant as a function of temperature for multiple zirconium alloys, 310SS, 304SS and APMT^{TM}. This oxidation constant, represents the rate at which the oxide grows, becoming parabolic the thicker the oxide layer becomes [20].

As shown in Figure 7, 310SS and APMT^{TM} (which reacts similarly to FeCrAl) have a much lower parabolic rate constant than that of zirconium alloys and 304SS. Zircaloy and historic 304SS cladding are thus more likely to spall and corrode in a reactor environment due to the excessive oxygen diffusion through the material [20]. This is due in part by 310SS and FeCrAl containing more chromium and aluminum, respectively, than 310SS.

The high material strength of iron-based alloys compared to that of zirconium alloys allow for manipulation of the cladding geometry. If additional fuel material is needed, ferritic and austenitic cladding materials can be partially thinned without losing their mechanical integrity.

Figure 8 plots the creep rupture stress of cladding materials as a function of temperature [20]. Despite zirconium having a higher melting point, its rupture stress limit at higher temperatures is less than that of the alternate cladding candidates APMT^{TM} and 310SS.

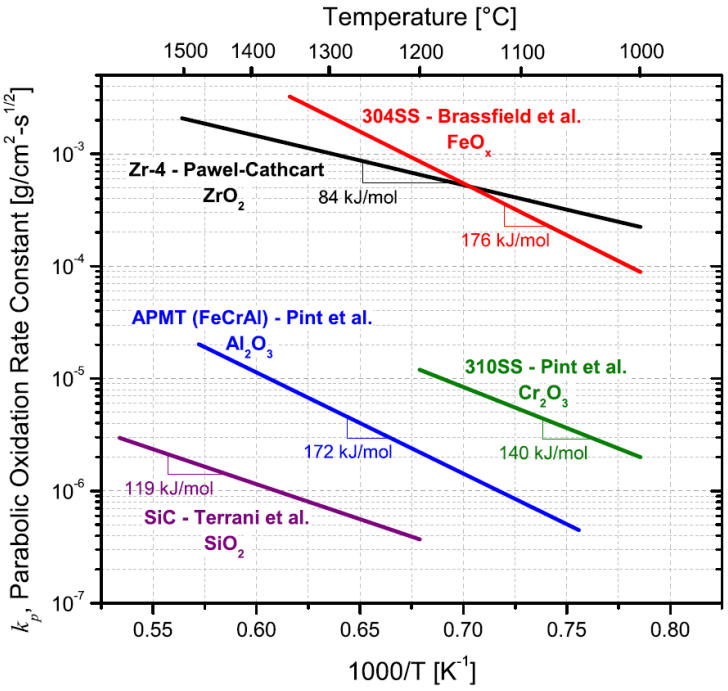


Figure 7: Arrhenius plot of the parabolic rate constants [20]

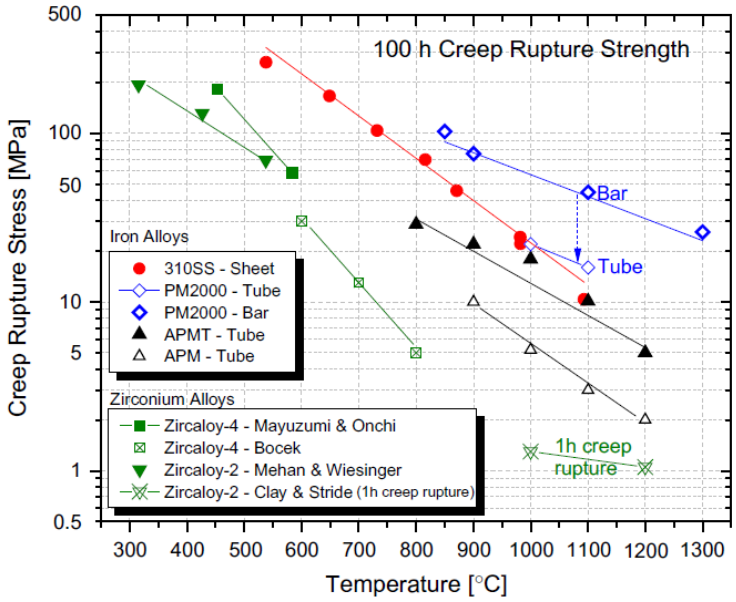


Figure 8: Comparison of creep rupture strengths of iron alloys

II.C.3 Silicon Carbide

Although silicon carbide (SiC) has been used in high temperature gas reactors, the material has not yet been utilized as cladding for light water cooled nuclear fuel. Regardless, SiC/SiC composites (SiC fibers embedded in SiC matrix) have gained commercial interest in high-temperature, hostile environments [23]. Material data suggests that the SiC displays excellent performance in a LWR environment and is known to be very stable in the presence of very high fast neutron fluences. While zirconium based alloys produce hydrogen induced degradation mechanisms, the phenomenon is virtually non-existent in SiC/SiC composites [24].

In a UO_2/zirconium alloy fuel environment, the UO_2 pellet swells upon thermal expansion and irradiation growth while the zirconium cladding undergoes creep, which in turn closes the gap region and causes pellet cladding interaction (PCI). In UO_2/SiC system however, the cladding material would not undergo a creep towards the pellet. Therefore PCI is a function of the rate at which the pellet swells in relation to swelling of the SiC material. Under a reactivity insertion accident or ramp in power, the delay of closure between the pellet and gap is crucial in reducing

the chances of a rod failing. If a reasonably large gap is initially considered, then the space between the pellet and cladding in a UO_2/SiC fuel design would never fully close throughout the lifetime of the fuel [23].

A disadvantage in utilizing SiC includes the poor thermal conductivity properties within the SiC/SiC composite material. Extended separation of the cladding and pellet region as well as its poor conductivity would lead to increased fuel centerline temperatures if implemented in a LWR system. Another challenge when utilizing SiC as a cladding concept is the lack of a concrete solution on how to seal the cladding tube after the fuel pellets have been loaded. This is due to the inability of SiC composites to melt, but rather sublimate at 3003 K, making welding impossible [24].

Figure 7 shows the oxidation rate of SiC is a small fraction of zirconium based alloys at high temperatures. This becomes an extreme advantage under accident scenarios. At 1473 K, zirconium-based alloy cladding ductility would be lost in 5 minutes of exposure to high temperature steam. After 15 minutes of exposure, the material would disintegrate upon reflooding of the core. On the contrary, SiC cladding, having a much slower oxidation process, would survive for hours at temperatures of 1673 K [24].

II.D. Fuel Performance Modeling

There are numerous failure mechanisms within a reactor that can lead to the release of radioactive material. As pellet and cladding temperatures increase from the intense core conditions, pressure in the gap can fluctuate. Although grid to rod fretting is the number one cause of fuel failure, PCI is also of major concern. On the other hand, the overall thermal conductivity of the rod decreases when the cladding does not come into contact with the pellet for an extended period of time. This can lead to exceedingly high centerline temperatures of the fuel. PCI, fission gas buildup and irradiation creep/swelling are factors that need to be analyzed when investigating alternate cladding material.

BISON-CASL (formerly PEREGRINE) is a finite-element simulation tool for nuclear fuel elements that is based on the MOOSE (Multiphysics Object Oriented Simulation Environment) framework and utilizes capabilities from the BISON fuel-modeling tool developed by Idaho National Laboratory. It utilizes Jacobian-Free Newton-Krylov method to solve fully coupled and fully implicit partial differential equations while leveraging the scalability of parallel computing. Because of the expandability of the MOOSE framework, BISON-CASL can incorporate a host of materials as well as behavioral models for fuel and fuel cladding. It has the capability to model complex thermo-mechanical behavior of discrete and smeared fuels, the fuel rod gap and plenum, and various cladding materials over time [25-27].

Though primarily used for LWR applications, BISON-CASL has the ability to analyze TRISO fuel designs as well as metal fuel in rod and plate form [28]. Models have been implemented in BISON-CASL to analyze thermal and irradiation creep and growth of Zircaloy as a cladding material [29]. However the code can model specified compositions of alternate cladding candidates by creating fuel performance material libraries [30].

II.E. Reactor Physics Modeling and Simulation

When considering all of the different full-core analyses one can perform: neutronics, material performance, thermal hydraulics, fluid dynamics, it is nearly impossible to accurately model all of the inner workings of a reactor with the same code. For the scope of this dissertation, the final objective was to simulate BWR ATF fuel in a 3D nodal simulator with thermal hydraulic feedback. Accomplishing this allows for analysis of core properties, such as reactivity and linear heat rate coupled with feedback mechanisms such as coolant density, fuel temperature and CB insertion fluctuations. However before this process can be done, many steps must first take place analyzing the fuel in zero, one and two-dimensions. The following section will discuss the availability of various 2D neutron transport and full core simulators that are used for research and industry applications.

II.E.1 Lattice Physics

When performing reactor physics calculations, there are two types of neutron transport codes available: stochastic and deterministic. Stochastic neutron transport codes use probabilistic algorithms such as Monte Carlo to approximate the k-effective eigenvalue, while deterministic codes solve the Boltzmann's Equation using discrete ordinates or method of characteristics. In order to calculate interaction probabilities as a function of particle energy, cross-section data from libraries such as ENDF and JEFF can be utilized.

Stochastic codes that are currently maintained for reactor applications include: MCNP, SERPENT, KENO and SHIFT. These codes use a certain number of specified particles (histories) per generation to calculate an approximate answer to an exact geometry layout. By tracking the particles position, direction and energy, interaction probabilities from the reactor's compositions are evaluated and the eigenvalue can be calculated to a certain standard error. With the exception of KENO[1], all of these codes utilize a continuous energy spectrum when binning a particle's energy ([1]Continuous Energy-KENO in development).

Nuclear vendors: General Electric (GE), Westinghouse, AREVA, etc. use deterministic transport solvers when optimizing fuel bundles prior to their construction. CASMO is an industry sponsored code developed by the Swedish company, Studsvik. CASMO uses Method of Characteristics to solve the two-dimensional transport solution [31]. PARAGON, used at Westinghouse, solves the 2D lattice calculations based on collision probability and interface current coupling methods. Written in FORTRAN 90/95, PARAGON uses advanced numerical methods such as the Successive over Relaxation method to significantly reduce computational runtimes [32].

Various non-industry deterministic codes include: NEWT, MPACT and DENOVO. MPACT, which is developed at the University of Michigan, also uses Method of Characteristics to solve the neutron transport problem. NEWT and DENOVO however, use a specified Sn quadrature through discretized elements and energy groups. All of these codes have the capability to generate homogenized few-group cross-sections. This is crucial if 3D calculations are to be done in a 3D core simulator, as will be discussed in following sections.

II.E.2 Parametric Analysis

When performing a neutronic parametric study on advanced fuel designs such as ATFs, numerous iterations of models need to be investigated and run before a design can be optimized. Before a fuel can be considered for commercialization, the design must be able to meet standard licensing criteria including: reactivity lifetime requirements, core power peaking, reactivity coefficients, etc. However, all of these checks cannot be done thoroughly with one model. First, the fuel must contain sufficient fissile material in order to meet cycle length requirements.

In a later section, this dissertation will display methodology for setting up a pass/fail system for FCM in PWRs and alternate cladding in both PWR and BWRs. Based off of the linear reactivity model [33], the methodology is called the EOC Reactivity Method [1]. The goal of this methodology is to greatly improve the speed and ease in which parametric analyses are performed when attempting to simulate full-core conditions with only lattice physics results.

II.E.3 3D Full Core Simulators

As aforementioned, accurately modeling a full core reactor is no small feat. Aside from Consortium of Advanced Simulation of Advanced LWRs, (ongoing at ORNL), coupling neutronics with thermal hydraulics, material degradation, computational fluid dynamics, etc. is virtually non-existent in coding packages today. However, there are various 3D simulators available that offer coupled thermal hydraulics with neutron diffusion. Some of these codes include: PARCS, NESTLE and SIMULATE; all of which first require generation of few-group cross-section from lattice physics codes modeling on an assembly level.

Sponsored by the NRC, PARCS solves the multi-group neutron diffusion equation with direct coupling to the thermal hydraulic code TRACE [34]. Developed and maintained at The University of Tennessee, NESTLE uses the Nodal Expansion Method to solve the eigenvalue problem in steady-state and transient conditions [35]. The Homogeneous Equilibrium Model (HEM) and Drift Flux Model (DFM), both available in NESTLE, provide thermal hydraulic coupling with LWR systems; however ongoing work is being done to allow simulation of liquid salt-cooled reactors. Also developed by Studsvik, SIMULATE is a nodal code made for PWRs

and BWRs. CASMO, which conducts the lattice physics calculations generates the few-group cross section data required for SIMULATE [31].

III. PWR METHODOLOGY AND INPUT PARAMETERS

III.A. PWR Pin Cell and Lattice Modeling

To model the neutronic behavior of the FCM fuel as well as alternate cladding materials in a PWR environment, simple 2D pin cell analyses were performed using SCALE/TRITON from SCALE 6.1.2 [2, 36, 37]. The CENTRM module from SCALE was used to produce resonance-shielded 238-group cross sections based on ENDF/B-VII.0 [38] nuclear data. TRITON couples the 2D radiation transport code NEWT with ORIGEN for isotopic decay and depletion calculations.

Modeling the fuel as a single repeating pin cell with reflective boundary conditions allowed for a large number of cases to be run in a short time, with each case containing numerous perturbations and iterations. Figure 9 depicts the TRITON model of the reference case pin geometry based on a Westinghouse 17 × 17 PWR fuel rod. The polygonal geometry is the TRITON representation of a cylindrical geometry.

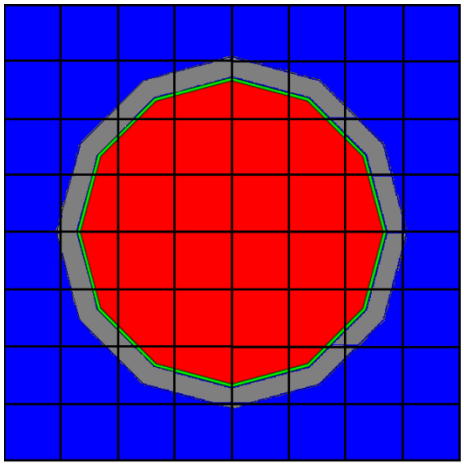


Figure 9: Westinghouse 17 × 17 PWR pin cell model

The inner red region represents the UO_2 pellet fuel used in all cases. The surrounding green and gray rings denote the gas gap and cladding material, respectively. Finally, the blue surrounding region represents the borated water coolant. Throughout this study, P/D and the pellet-cladding gap were kept constant at 1.326 and 82.55 μm, respectively. An average value of 630 ppm boron was placed in the water coolant to simulate the letdown of boron concentration from beginning of cycle (BOC) to EOC.

During the alternate cladding study, when performing pin cell calculations in SCALE, the temperature of the fuel was kept at an average of 900 K, while the cladding and gap were modeled at 600 K [39]. However, due to a reduction in conductivity when using SiC cladding, the temperature of the fuel was raised to 1,100 K, and the temperature of the cladding and gap were raised to 700 K [23]. The borated water in the system was modeled at 580 K at a constant density of 0.7119 g/cm^3 for all cases.

When modeling FCM fuel, particles were simulated with the double heterogeneous (DH) module in SCALE. Equally spaced in a lattice configuration within the fuel region of Figure 9, the particles were encapsulated in a SiC matrix. It was clear early on that a core consisting of UO_2-fueled FCM fuel assemblies would not sustain three 18-month cycles as is typical for currently operating PWRs. Even with 19.75% enriched uranium and a kernel diameter (KD) of 500 μm, the total fuel volume in the design is not sufficient to reach the three cycles achieved by current PWR designs at enrichments of up to 5% ^{235}U. Thus changes to the particle geometry and insertion of an alternative fuel form were investigated to increase the fissile loading in the FCM design.

In addition to pin cell calculations, 17 × 17 PWR lattices were also modeled in SCALE. By constructing a quarter lattice of 8.5 × 8.5 pins with reflective boundary conditions on each side, an infinite array of 17 × 17 pin lattices was modeled. This technique was used to verify eigenvalue calculations done on a pin cell level and to analyze fuel pin power peaking of the FCM fuel. Pin power peaking factors were evaluated using the relative pin power arrays calculated by SCALE/TRITON. These are used to compare hotspot locations from pin to pin in a

typical fuel assembly. Figure 10 represents a quarter lattice printout from SCALE of a PWR assembly.

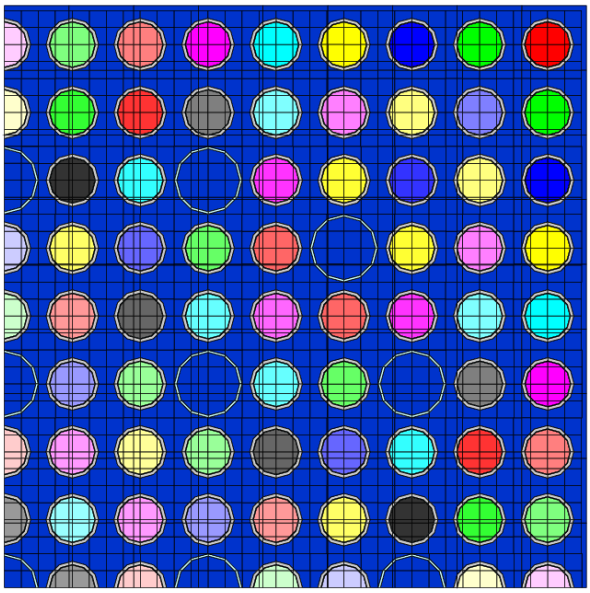


Figure 10: Westinghouse 17 × 17 PWR lattice model, with independent depletion mixtures indicated by different colors in the fuel pins

III.B. Reactivity-Equivalent Physical Transformation for TRISO Fuel

When modeling the FCM fuel, the larger 2D problems were proven to be too computationally expensive to practically model the DH designs with SCALE. Therefore modeling techniques were investigated to circumvent this problem. In particular, a modified version of the reactivity-equivalent physical transformation (RPT) method was used to simulate an equivalent pin that exhibits the same reactivity characteristics as those of a DH treatment. Figure 11 depicts the manipulation of TRISO fuel in a SiC matrix by homogenizing the DH fuel zone into a single-heterogeneous zone [40].

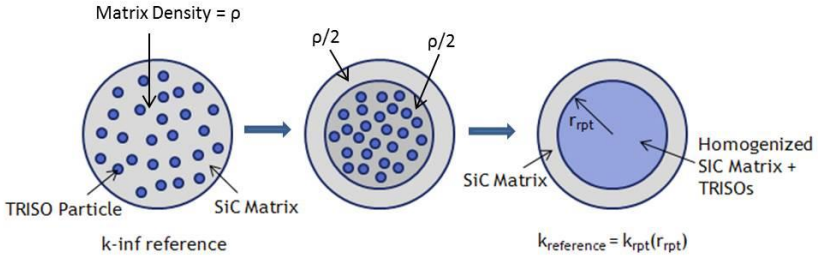


Figure 11: Reactivity-equivalent physical transformation process

As shown in Figure 11, the fuel and matrix regions are compacted and smeared into a smaller cylinder, which in turn raises PF, resonance escape probability, and reactivity. This is needed because when the fuel and matrix are homogenized, the resonance escape probability decreases, thus increasing resonance self-shielding in ^{238}U. To counterbalance the effective decrease in reactivity, the radius of the matrix and fuel region is modified until the multiplication factor is equal to that of the original DH configuration [40]. The resulting homogeneous fuel can then be modeled with standard single-heterogeneous approaches.

III.C. Alternate Cladding Input Parameters

Table II provides the cladding materials examined in this study along with their detailed elemental compositions. This list includes a baseline zirconium alloy (Zircaloy-4), austenitic stainless steels (304SS and 310SS), generic and commercial variants of iron-chromium-aluminum alloys (FeCrAl and APMT^{TM} [41] respectively), and SiC.

For reactivity calculations, a number of fuel rod geometries were considered. A standard PWR 17 × 17 fuel bundle [42] with 4.9% enriched urania (UO_2) pellets was chosen as the reference case. Table III provides the various geometries used during reactivity calculations. Case 1 is the reference case; the other cases increase heavy metal and fissile loading in the assembly by either increasing the pellet diameter at the expense of reducing cladding thickness (Cases 2–4) or increasing uranium enrichment (Cases 5–8). Analyses were performed for all cladding material

options for Cases 1–8; Case 9 was analyzed only for SiC to represent the thicker cladding structures demonstrated to date for SiC-based materials [43].

Table II. Cladding Compositions Used for Fuel Reactivity Calculations

Material		Fe	Cr	Al	Zr	Ni	Sn	Mn	Mo	Y	Si	Hf	C
Zircaloy		0.15	0.1		98.26		1.49						
304SS		71.35	18.9		0	8.35		0.7	0.27		0.42		
310SS	wt %	52.55	25.22		0	19.51		1.9	0.122		0.7		
FeCrAl		75	20	5	0				0		0		
APMT™		69.79	21.6	4.9	0.1				2.8	0.12	0.53	0.16	
SiC											70.08		29.92
Zircaloy		0.24	0.17		98.43		1.15						
304SS		70.44	20.04			7.84		0.7	0.16		0.82		
310SS	at %	51.72	26.66			18.27		1.9	0.07		1.37		
FeCrAl		70.2	20.11	9.69									
APMT™		65.84	21.89	9.57	0.06				1.54	0.07	0.99	0.05	
SiC											50		50

Table III. Various Rod Geometries used for Reactivity Calculations

Case #	ΔUO_2 Volume	Pellet OD [mm]	Gap Thickness [μm]	Clad ID [mm]	Clad OD [mm]	Clad Thickness [μm]	U enrichment
1 (ref)	0	8.1915	82.55	8.3566	9.4996	571.5	4.9%
2	3.5%	8.3345	82.55	8.4996	9.4996	500	4.9%
3	8.5%	8.5345	82.55	8.6996	9.4996	400	4.9%
4	13.7%	8.7345	82.55	8.8996	9.4996	300	4.9%
5	0	8.1915	82.55	8.3566	9.4996	571.5	5.5%
6	0	8.1915	82.55	8.3566	9.4996	571.5	6.0%
7	0	8.1915	82.55	8.3566	9.4996	571.5	6.5%
8	0	8.1915	82.55	8.3566	9.4996	571.5	7.0%
9	-14.9%	7.5565	82.55	7.7216	9.4996	889	5.5%

Notes: OD = Outer Diameter; ID = Inner Diameter.

III.D. Lattice-Physics Based EOC Reactivity Equivalence Methodology

An analytical method was applied to the single-pin depletion results to approximate a multi-batch loading scheme in a modern PWR. That way, when changes were made to the cladding, enrichment or particle geometry (FCM fuel), reactivity could be compared between each model and the Zircaloy-cladding pellet fuel reference case. Figure 12 shows a typical core configuration found in a three-batch Westinghouse PWR. Table IV provides batch-specific parameters that were used and are typical for the type of loading scheme portrayed in Figure 12; core volume fractions and relative assembly powers were used to determine the EFPD for each batch of fuel at the EOC.

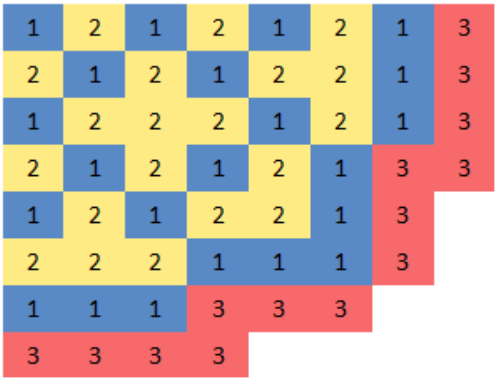


Figure 12: Assumed PWR core configuration of batch-specific loading pattern

Table IV. Assumed Batch-dependent Assembly Counts, Core Volume Fractions, Relative Assembly Powers, and EFPD for a Typical Westinghouse PWR

Batch (e_b)	**Number of Assemblies**	**Core Fraction Vol % (V_b)**	**Relative Assembly Power (P_b)**	**EFPD Achieved at EOC**
1	73	38%	1.25	627
2	68	35%	1.19	1221
3	52	27%	0.40	1420
Total	**193**	**100%**	-	-

The core fractional volume was defined for each depletion cycle. For example, Cycle 1 consists of 73 assemblies and, thus, makes up 38% of the 193 total assemblies present in a PWR core. The relative assembly power factor (P_b) is the energy output per batch relative to the average energy of all cycles (from a typical Westinghouse PWR). The total EFPD represents the cycle EFPD obtained by weighting the EFPD increment for each batch by its core volume fraction. Batch 3 represents the discharged fuel with 1,420 EFPD.

The magnitude of the infinite multiplication factor (k-infinity) at 627, 1,221, and 1,420 EFPD was used to estimate the EOC $\overline{\Delta k}_{core}$ for each fuel geometry that was simulated. In doing this, a method similar to the Linear Reactivity Model [33] was developed [1]. The EOC reactivity for each case was compared to that of a reference case (standard PWR fuel rod containing UO_2 pellets). The core average eigenvalue difference can be estimated using Eq. (4.1):

$$\overline{\Delta k}_{core} = \frac{\sum_b x_b\left(e_b\right) P_b V_b}{\sum_b P_b V_b} \quad . \tag{3.1}$$

In this equation, x_b is the difference in k-infinity between the fuel design under consideration and that of the reference case as a function of exposure (e_b). The EOC EFPD values from Table IV were used to quantify the level of exposure each batch received. The power weighting factor (P_b) approximates the power distribution in the core to provide a measure of contribution of each fuel batch to the overall core reactivity. Finally, the number of assemblies per fuel batch found in a given cycle of a PWR core is denoted by V_b.

Although the method was used for both fuel forms studied thus far, Figure 13 shows the EOC EFPD at the end of each batch cycle when comparing alternate cladding materials. With the exception of SiC, all alternate cladding concepts fall well short of Zircaloy cladding. The EOC reactivity method will be used in later sections when presenting results of the parametric design studies.

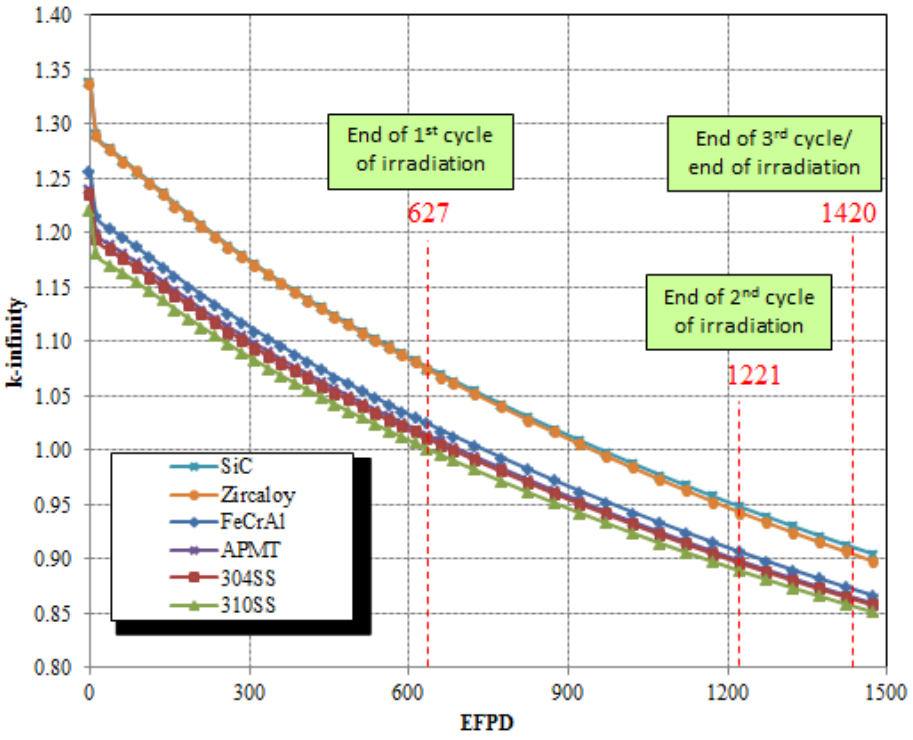


Figure 13: Infinite multiplication factor vs. effective full power days for various cladding materials in standard PWR 17 × 17 rod geometry

IV. BWR METHODOLOGY AND DESIGN PARAMETERS

IV.A. Lattice Physics Models

The abundant heterogeneities found in commercial BWR bundles preclude modeling a single fuel rod as a reasonable approximation for an entire fuel bundle or reactor when analyzing BWR fuel at the lattice physics level. In contrast to the previous analysis done on PWRs, BWR heterogeneities include axial and radial enrichment and gadolinium loading variations, partial-length (vanishing) fuel rods, plus a significant range of axial void distributions. Therefore, initial lattice physics calculations were performed using the 2D discrete ordinates module TRITON from SCALE6.1 in order to model the BWR fuel bundles.

It was important in this study to model modern bundle designs that would be commercially relevant in today's standards. Therefore bundle designs representative of modern 10 × 10 enrichment/gadolinium layouts were chosen for this simulation. TRITON models were assembled to produce lattice arrays such as the one shown in Figure 14 [44-46] which is representative of a modern GE12 or GE14 10 × 10 bundle.

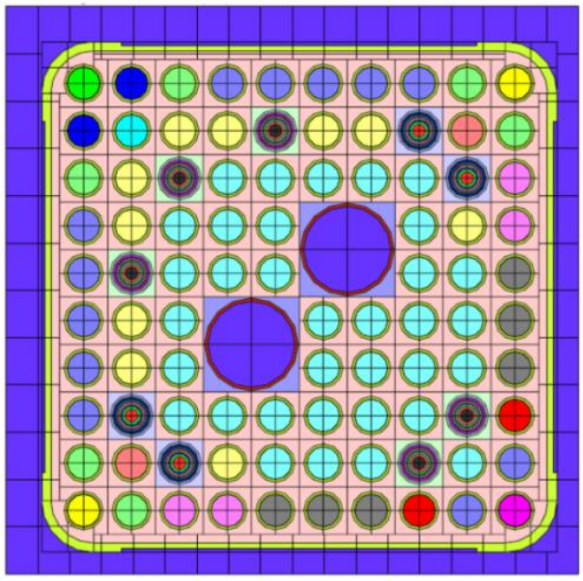


Figure 14: Modern 10 × 10 BWR lattice modeled with TRITON [44]

The lattice shown in Figure 14 contains 92 UO_2 fuel rods, 9 of which are loaded with gadolinium to hold down reactivity and help control power peaking. The two large circles in the center of the array represent water holes used for increased moderation. A channel box surrounds the 10 × 10 array and allows for an isolated flow of coolant to that of the adjoining bundles. The temperature of the UO_2 pellet was modeled at 950 K while the cladding and coolant was set to 622 K and 540 K, respectively. For the initial base case, the surrounding coolant was modeled with a 40% void. Reflective boundary conditions were modeled around the lattice, essentially simulating an infinite array of fuel bundles.

Initially, Zircaloy was modeled in the cladding and channel box in order to establish a base case. Next, all forms of Zircaloy were replaced with the less oxidizing FeCrAl to assess the neutronic penalty. The base case cladding and channel box thickness for the Zircaloy model was set to 600 and 1600 μm, respectively. When replacing Zircaloy with the higher absorbing FeCrAl, the cladding and channel box thickness was reduced in order to decrease absorption events and increase the heavy metal loading within each fuel pin.

In addition to the Zircaloy and FeCrAl fuel bundles, a hybrid bundle was modeled with a SiC/Ni/Cr channel box and FeCrAl cladded fuel pins. Figure 15 presents a portion of the lattice displaying the thickness of each channel box layer. For this design, the cladding thickness of FeCrAl was set to 300 μm, while the SiC layer of the channel box was kept at the base case thickness of 1600 μm.

The fuel design shown in Figure 15 was modeled in CASMO by homogenizing the channel box layers. Conserving the mass of each layer, the SiC, Ni and Cr densities were smeared into one composition surrounding the 10 × 10 array of UO_2/FeCrAl fuel pins. This was permissible as the mean free path of a thermal neutron is significantly less than the thicknesses of the Ni and Cr layers.

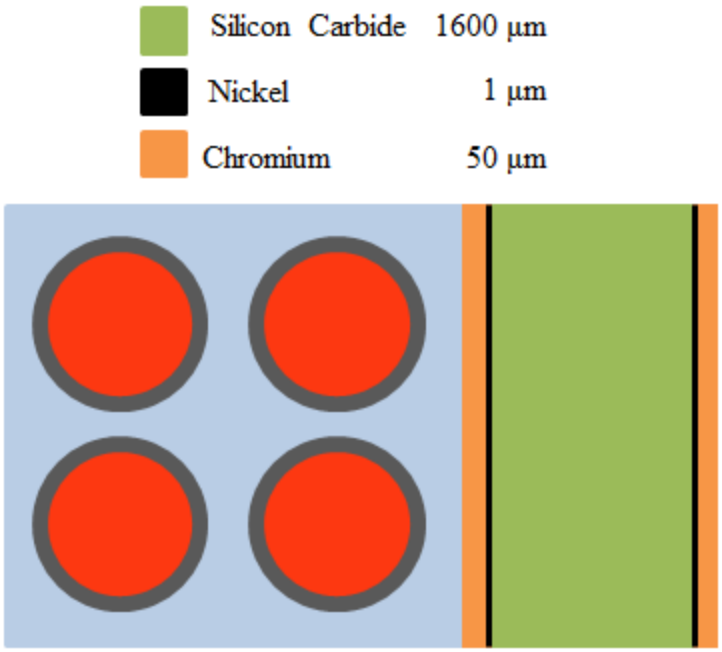


Figure 15: Hybrid SiC channel box design

IV.B. End of Cycle Reactivity Calculations

A methodology was established for BWR systems similar to that of the PWR reactivity method [17]. Due to all of the standard heterogeneities found in a BWR, it was important that modern commercialized assemblies were used. Representative enrichment and gadolinium layouts for GE 10 × 10 bundles were developed on the basis of a report published by Michael Fensin [45]. Three different enrichment/gadolinium arrays were used to for the EOC lattice physics method to represent the three major fuel zones found in modern BWR bundles; namely, the Power Shaping Zone (PSZ), the Dominant Zon (DOM), and the Vanishing (VAN) regions, from bottom to top, respectively. The PSZ and DOM zones contain 92 fuel pins with UO_2 enrichment ranging from 2.00% to 4.90% U-235 and maintain a weighted average enrichment of 4.11%, which was used as a basis to compare enrichment increases when replacing the Zircaloy cladding with that of FeCrAl.

The representative 10 × 10 bundles contain partial-length rods represented in the VAN region. The VAN, containing 14 vanishing rods, has a total of 78 UO_2 fuel rod locations. Figure 16 displays where each of the three lattices that were described above is located axially within the fuel bundle. Although not drawn directly to scale, the partial-length rods are shown to disappear in the vanishing region.

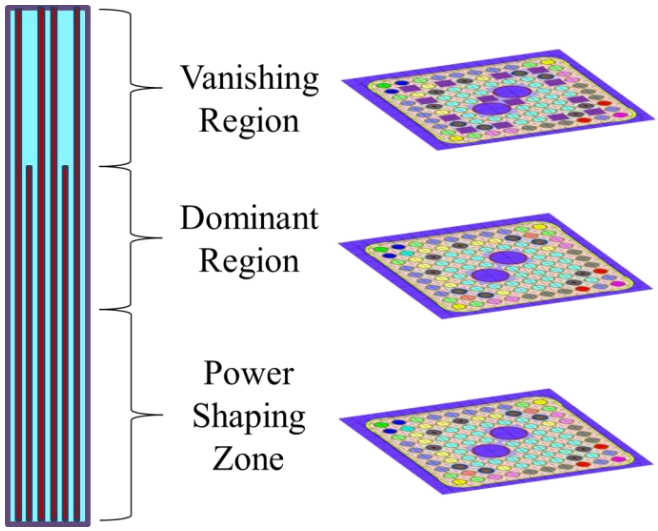


Figure 16: Allocation of Lattices within BWR Fuel Bundle

Similar to the PWR EOC method, numerous cases were run during the parametric study to encompass the design space. To expedite the calculation time of full fuel lattices (as opposed to pin cell calculations), CASMO-4 was utilized instead of TRITON. CASMO enabled the UO_2 enrichment and clad/channel box thickness of the fuel bundles could be manipulated and re-run within a reasonable timeframe.

Next, an assembly LP of a realistic and representative core would need to be established to determine the number of EFPD each cycle would obtain. In keeping with modern BWR designs, representative exposure data was found from cycle 17 of Peach Bottom Unit 2 (PB2C17) [47].

The core utilized a three-batch scheme and operated with GE14 fuel bundles, making it consistent with the EOC method. Figure 17 illustrates an exposure map from PB2C17 displaying BOC burnup for each bundle in units of giga-watt days per metric ton of uranium (GWd/MTU).

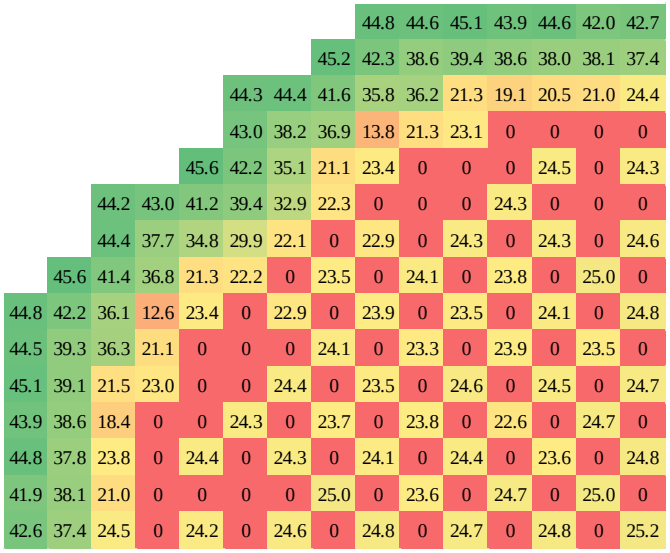


Figure 17: General Electric BWR Quarter Core Exposure Map [47]

Red locations indicated with a zero burnup represent fresh feed assemblies, while depleted cells in yellow and green represent once and twice burnt assemblies, respectively. Using the values shown in Figure 17, Table V was gathered to establish the achieved number of EFPD for each cycle similar to that of the PWR methodology.

Using a python script, k-infinity was obtained at the exact EFPD shown in Table V by interpolating between the high-fidelity CASMO time steps. These k-infinity values were then used in equation 3.1 to estimate the EOC $\overline{\Delta k}_{zone}$ for each axial slice of the fuel bundle simulated. The EOC reactivity for each case was compared to that of the reference (standard Zircaloy lattice).

Once $\overline{\Delta k}_{zone}$ was calculated for each axial slice, $\overline{\Delta k}_{bwr}$ could be found for the entire core by weighting each $\overline{\Delta k}_{zone}$ with two additional factors: axial height of each zone (H_Z) and power

factor of each zone (P_Z). Both H_Z and P_Z are a function of the axial zones pertaining to (z). The current method contains three zones, (PSZ, DOM and VAN). In determining the average power factors, a generic BWR power shape was desired. Using traversing in-core probe (TIP) data taken from the Peach Bottom Unit 2 Operations Report [48], the relative axial power factors were plotted in Figure 18. The data points relative to height were divided into three axial sections and the average relative power throughout that region was calculated at the bottom of each zone: (PSZ in blue, DOM in red, VAN in green).

Table V. Assumed Batch-dependent Assembly Counts, Core Volume Fractions, Relative Assembly Powers, and EFPD for a Typical General Electric BWR

Batch (e_b)	**Number of Assemblies**	**Core Fraction Vol % (V_b)**	**Relative Assembly Power (P_b)**	**EFPD Achieved at EOC**
1	272	36%	1.36	**883.1**
2	276	36%	1.02	**1547.1**
3	216	28%	0.53	**1890.4**
Total	**764**	**100%**	-	-

It should be noted that for this EOC reactivity method, the natural enriched regions at the top and bottom of each assembly were neglected. The purpose of the EOC method was to allow for a high number of quick calculations when performing the parametric study. Additional regions of the bundles were considered when creating the full-core models that will be described in later in the study. Using the weighting factors from Figure 18 and the $\overline{\Delta k}_{zone}$ calculated by equation 3.1 for each slice, an overall $\overline{\Delta k}_{bwr}$ was calculated for the entire representative core.

$$\overline{\Delta k}_{bwr} = \frac{\sum_z \overline{\Delta k}_z H_z P_z}{\sum_z H_z P_z} \tag{4.1}$$

Thus, if a $\overline{\Delta k}_{bwr}$ value of 0.000 was calculated, the design parameters fit to the alternate cladding fuel bundle would meet reactivity lifetime requirements of the standard Zircaloy model. However if a sub-zero $\overline{\Delta k}_{bwr}$ was calculated, then a decreased cycle length would result.

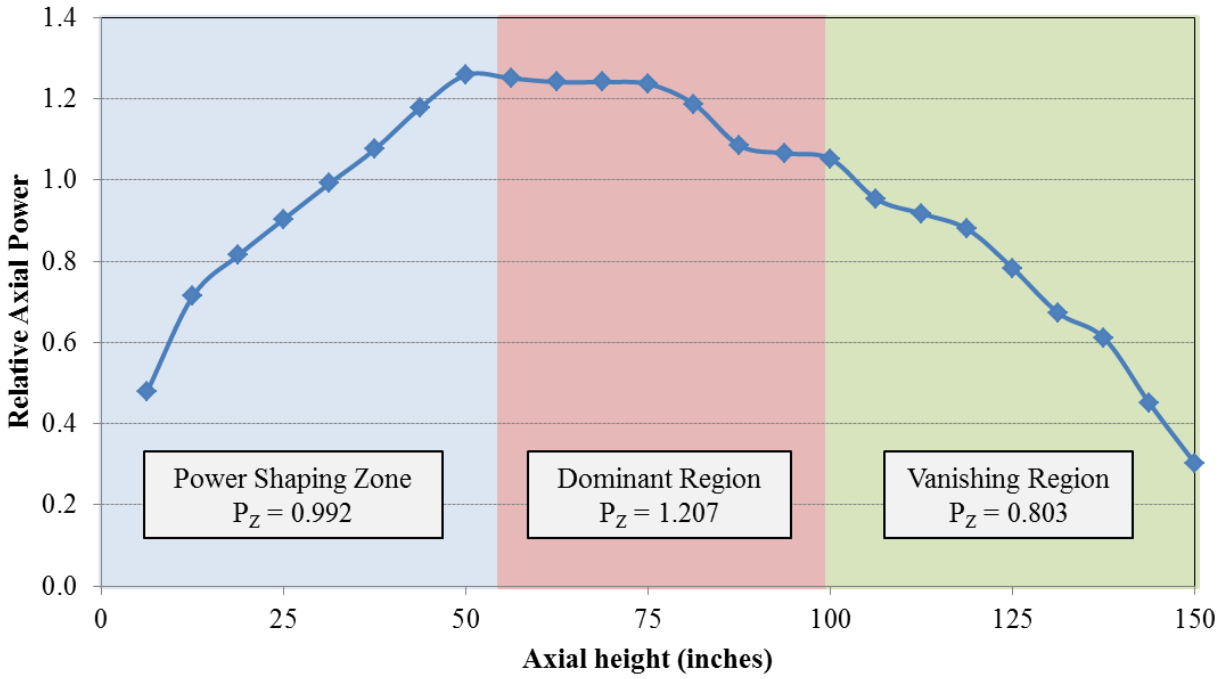


Figure 18: Relative Axial Power from Peach Bottom Tip Data

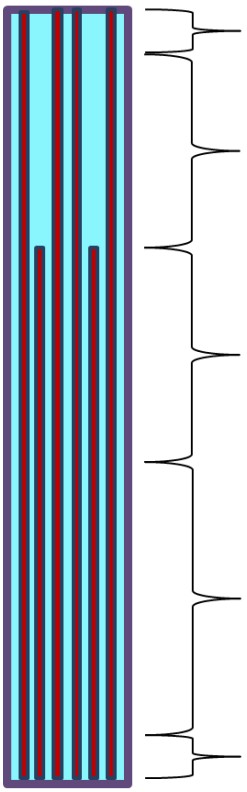
IV.C. Full-core BWR Model

IV.C.1. Lattice Physics Cross-section Generation

The full-core 3D BWR simulations were carried out with the latest version of the NESTLE nodal diffusion simulator which is currently maintained at the University of Tennessee [49-51]. In order to run NESTLE models, few-group cross-sections needed to be obtained from a lattice physics code. During this study, the lattice physics calculations were performed with the

Studsvik's code, CASMO-4, which uses the Method of Characteristics to solve the 2D neutron transport equation in 70 energy groups with ENDF/B-VI cross-section libraries.

Although only three axial slices were modeled for the EOC reactivity method, it was important to increase the accuracy when establishing a 3D full-core model. Therefore, the natural enriched regions that are located at the top and bottom of a standard BWR fuel assembly were modeled in CASMO. Throughout the study, UO_2 enrichment was perturbed in the three middle zones (PSZ, DOM and VAN). However the enrichment in the natural zone was always kept at 0.71% ^{235}U. In accordance with the PSZ and VAN, respectively, the lower NAT zone contains 92 UO_2 fuel pins, while the top NAT zone contains 78 due to vanishing rods. Figure 19 represents the five layer BWR assembly which provided all of the axial layers necessary to model the representative core.



Axial Zone	Number of Fuel Cells	Average Weighted UO_2 Enrichment
Upper Natural	78	0.71%
Vanishing	78	4.00%
Dominant	92	4.11%
Power Shaping	92	4.11%
Lower Natural	92	0.71%

Figure 19: Axial zone parameters of modern 10 × 10 BWR bundle

Before replacing the Zircaloy cladding and channel box, it was important to establish a realistic base case model. The enrichments shown in Figure 19 represent the conditions used for Zircaloy base case core, however fuel parameters (such as enrichment) were eventually perturbed when swapping out the cladding/channel box. Since empty fuel locations took place of higher enriched fuel pellets, the weighted enrichment average of the VAN region is slightly less than the DOM and PSZ regions.

For each lattice run in CASMO, branch perturbations of fuel properties were also executed. Before the diffusion equation can be solved in NESTLE at a particular fuel temperature or coolant void fraction, etc., cross-section data must first be established by the lattice physics code that encompasses the thermal hydraulic parameter ranges expected in the core. Therefore, each of the five axial slices from Figure 19 was run in CASMO at the base case conditions, but also with a high and low fuel temperature and void fraction with and without CB insertion.

In a BWR, the void fraction of the coolant can range from liquid phase to almost a 100% void near the top of the core. Because of this, determining the base case void level at each axial zone became paramount. If the initial void level at a given node did not correlate with what the thermal hydraulic model anticipated, the accuracy of the calculated eigenvalue would be off. Therefore numerous CASMO cases were run with varying nominal void conditions at each of the five zones. Then the outputted few-group cross-section data was re-run in NESTLE until reasonable axial void profiles were produced.

A CB is located in the northwest corner of each array. The cruciform blade thickness is 0.792 cm and consists of homogenized water and steel surrounding 0.50 cm B_4C cylinders. The base case and all branch perturbations were run with the CB fully withdrawn and fully inserted. Table VI represents 10 total cases performed in CASMO in order to obtain the necessary few-group cross-section data.

By depleting the10 cases in CASMO to 65 GWd/MTU, all of the required cross-section data was available for a full-core model in NESTLE. The CASMO output presents the data in the form of macroscopic cross-sections. NESTLE on the other hand reads the data in the form of polynomial coefficients as a function of each perturbation. Therefore, a python script was written to parse the

cross-section data from CASMO. As the python script is essentially bridging the gap between the lattice physics calculations and the 3D nodal code, the module was named CASMO to NESTLE (C2N).

Table VI. Branch Perturbation Specifications used in CASMO-4

Cases	Branch	Fuel Temperature (K)	Coolant Void Fraction (by axial zone)					Control Blade
			Lower NAT	PSZ	DOM	VAN	Upper NAT	
1	**Base Case**	950	5%	20%	40%	80%	80%	withdrawn
2								inserted
3	**Fuel Temperature**	1200						withdrawn
4								inserted
5		600						withdrawn
6								inserted
7	**Coolant Void Fraction**	950	100%					withdrawn
8								inserted
9			0%					withdrawn
10								inserted

IV.C.2. NESTLE Neutronics Model

The NESTLE nodal simulator was selected to model the full core BWR neutronics because of its availability at the University of Tennessee (where it is updated and maintained) and its proven ability to model many types of reactors [50]. The code solves the neutron diffusion equation with thermal hydraulic feedback under steady-state and transient core conditions. Due to the unavailability of public BWR core models containing advanced 10 × 10 fuel bundles, many assumptions and approximations as well as design experience, were used to assemble a representative BWR core to be used as the basis for this analysis.

Due to the quarter-core symmetry present in most commercial reactors, the model was reduced to $1/4^{th}$ its actual size and contained cyclic inner boundary conditions. Intuitively, zero flux

boundary conditions were used at the outer periphery of the reflector region. Homogenized cross-section data for sub-cooled water was placed from the bottom of the active fuel region to 9 inches below and extending 12 inches from the periphery of the core, radially. Similar to the upper NAT region shown in Table VI, cross-section data used for the reflector located 9 inches above the active fuel region was calculated with an 80% void. Prior work by J. Galloway proved to be very helpful in the development of a representative BWR core model [52].

As stated in section IV.C.1, few group cross-sections are to be fed into NESTLE to calculate core reactivity. By running the branch conditions in CASMO shown in Table VI: reactivity can be calculated for changes in the core such as: control rod insertion as well as fuel temperature and coolant void fluctuations. Equation 4.2 calculates the updated cross-sections when thermal properties in the core change [35].

$$\hat{\Sigma}_{xg} = a_{1_{xg}} + \sum_{n=1}^{2} a_{(n+1)_{xg}} (\Delta\rho_c)^n + a_{4_{xg}} \Delta T_C + a_{5_{xg}} \Delta \sqrt{T_{F_{eff}}} + \sum_{n=1}^{3} a_{(n+5)_{xg}} \left(\Delta N_{sp}\right)^n \quad (4.2)$$

Equation 4.2 considers coolant temperature changes as well as fluctuations in soluble boron (when modeling a PWRs). For the sake of modeling the representative BWR core, it was assumed that the moderator would be free of burnable absorbers, and any change in coolant temperature would directly affect the void of the fluid (essentially density). Therefore, for the simulations of the BWR core at hand, equation 4.2 can be simplified to the following:

$$\hat{\Sigma}_{xg} = a_{1_{xg}} + \sum_{n=1}^{2} a_{(n+1)_{xg}} (\Delta\rho_c)^n + a_{4_{xg}} \Delta \sqrt{T_{F_{eff}}} \quad (4.3)$$

Therefore, if an increase in fuel temperature occurs during the depletion sequence, the delta of its square root from that of the base case temperature (950 K) is calculated. This delta is multiplied by the fitting coefficient determined from C2N denoted by the variable a, and a new cross-section can be calculated. The variables: x and g from equation 4.3 represent the cross-section type and neutron energy group number, respectively. From there, the updated cross-section is fed into the spatially discretized neutron diffusion equation in order to calculate the eigenvalue (k)

with the nodal expansion method in NESTLE. The simplified diffusion equation along with the matrix expressions used to solve for k-effective are shown in equations 4.4 and 4.5 [53].

$$-\nabla \cdot D_g \nabla \phi_g + \Sigma_{tg} \phi_g = \sum_{g'=1}^{G} \Sigma_{sgg'} \phi_{g'} + \frac{\chi_g}{k} \sum_{g'=1}^{G} \nu_{g'} \Sigma_{fg'} \phi_{g'} \tag{4.4}$$

$$A\phi = \frac{1}{k} F\phi \tag{4.5}$$

C2N provides the majority of factors needed to solve the diffusion problem including: diffusion coefficient, thermal, scattering and fission cross-sections, number of neutrons born in fission as well as the fission neutron yield. The fast and thermal flux values are solved relative to the power at a given node which leads to the calculation of k-effective. Although NESTLE has the ability to simulate the fuel with up to four neutron energy groups, two were used to simulate the BWR fuel, fast and thermal. The energy group cutoff initially set in the CASMO calculations was 0.625 eV.

It was determined that the most viable way to compare alternate cladding material to that of Zircaloy would be under equilibrium core conditions. Therefore, the core model assembled consisted of three fuel batches: fresh feed, once burnt and twice burnt assemblies. Representative BOC exposure map and axial power profile were established [45] which are shown in Figure 20.

In Figure 20a the blue bundles denoted with -1 represent fresh feed assemblies, while the yellow/orange and red cells represent once and twice burnt assemblies, respectively. Burnt assemblies are ranked from lowest to highest according to exposure. Consistent with most commercial US core designs, twice burnt assemblies that have been exposed the most are place on the periphery of the core.

Exposure data was initially calculated for Zircaloy cladding with a thickness of 600 μm and a fuel pellet radius of 0.440 cm. When replacing Zircaloy with FeCrAl in the parametric study, the FeCrAl cladding was thinned to 300 μm which thus increased the pellet radius to 0.470 cm. By doing this, thermal absorptions would be reduced and the heavy metal loading in the core would increase. Therefore a correction factor multiplier was added to the radial exposure map when

modeling FeCrAl. Values in the exposure file were thus multiplied by $0.440^2/0.470^2$ to account for this increase in MTU.

a. b.

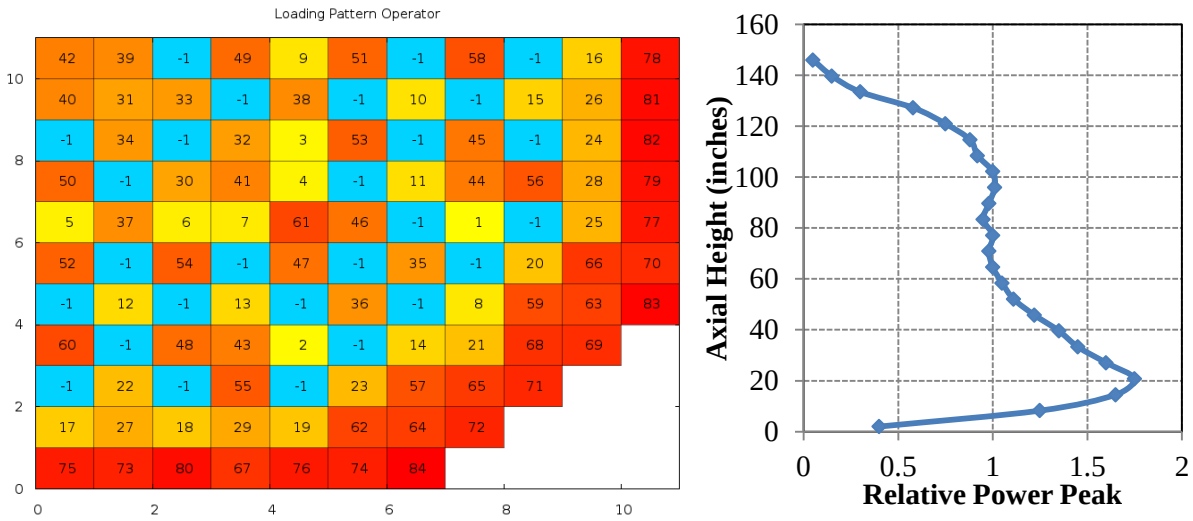


Figure 20: a) Radial Exposure Map of Representative BWR Core in units of MWd/MTU, b) Hot Axial Power Profile of DOM Region

With a power density of 55.66 kw/l, the total power of the representative core comes to 1910 mega-watt (MW) thermal. As shown in Figure 20a, there are 111 fuel assemblies present in the quarter core exposure map which 4 times more bundles in a full core. During the study, two different assembly types were used in the BWR core, both of which were comprised of a combination of axial zones from Figure 19. The following figure represents the two different bundle configurations used in the study.

Although the assemblies are very similar, there is one distinct difference between the two, and that is the power shaping zone. This region contains more gadolinium rods than that of the dominant region, making it useful for suppressing reactivity in the bottom of the core. In core design, these varying assemblies are strategically placed in the core to minimize power peaking.

Therefore a quick study was performed by running multiple arrays with varying assembly configurations. Although numerous cases were depleted in NESTLE, the following four are shown in Figure 22. The radial nodes denoted with the numbers 1 and 2 represent assembly type 1 and type 2. Cells listed with the number 3 represent reflector assemblies consisting of water that surround the periphery of the active fuel region.

The two different assembly designs containing Zircaloy cladding/channel boxes were shuffled radially and re-run in NESTLE in order to investigate the relative peaking factors and reactivity lifetime. After numerous iterations, it was concluded that Case 3 was the most suitable core design in minimizing relative peaking factors and extending the EFPD reached. For the remainder of the investigation, Case 3 was used when comparing bundles with alternate cladding material to that of the Zircaloy base case model.

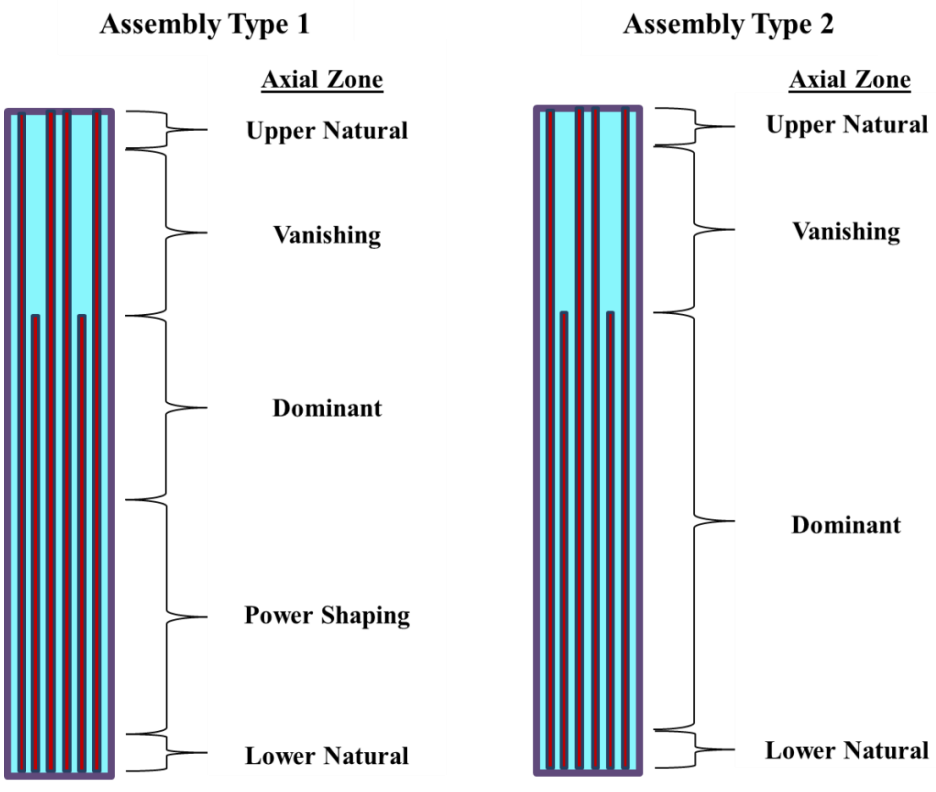


Figure 21: Axial zone configuration per bundle type

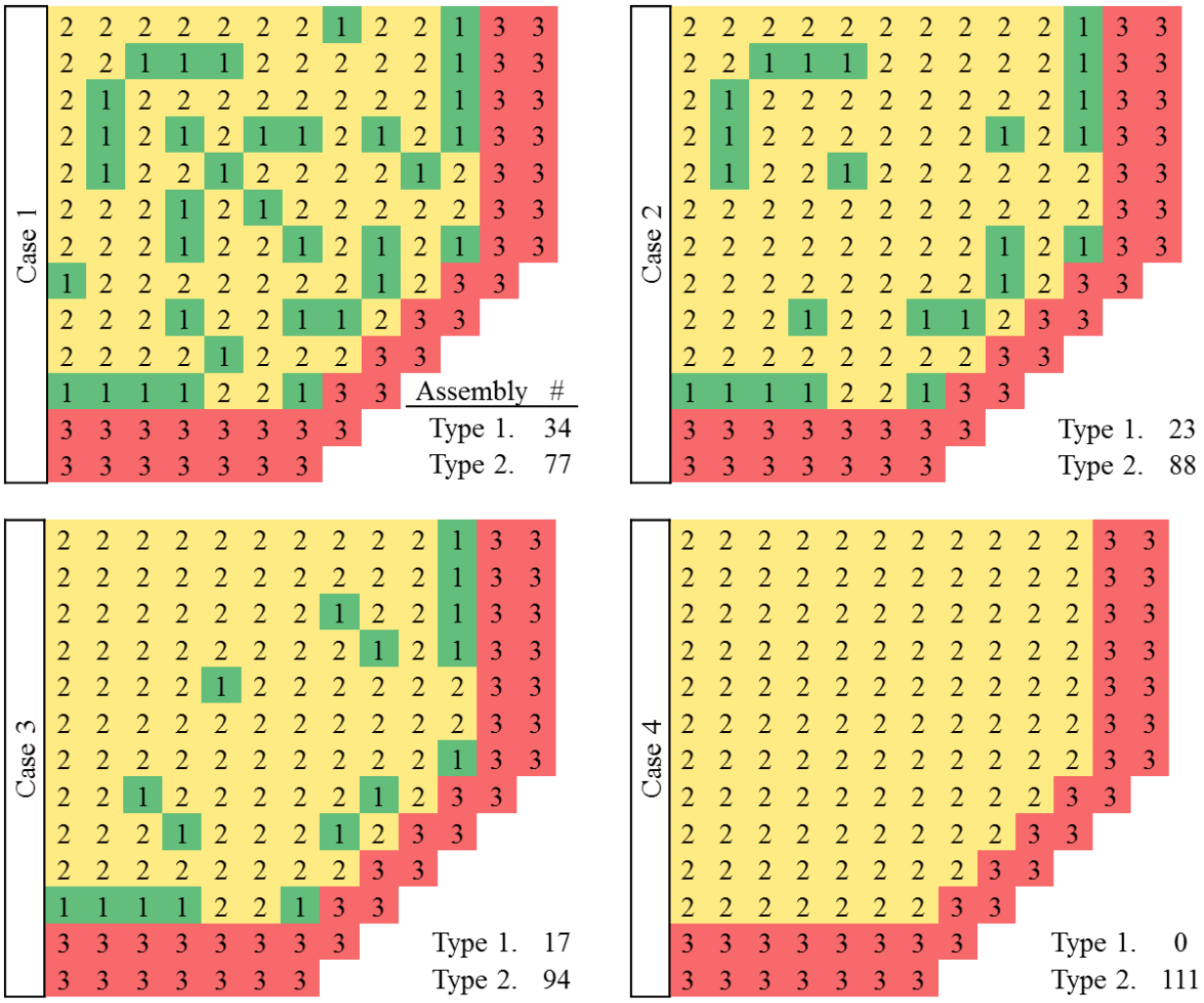


Figure 22: Assembly Configuration Optimization

IV.C.3. Alternate Cladding Full-Core Parametric Study

Once a full-core BWR base case model was established, a parametric study using NESTLE could be done with FeCrAl. Initially, depletion was performed with the same fuel design, by replacing Zircaloy for FeCrAl without changes to enrichment, cladding or channel box thickness. After performing an uncontrolled/excess reactivity calculation at BOC, k-effective values

resulted subcritical. This was expected in light of the lattice physics results previously performed for the EOC reactivity method. Therefore, similar to the 2D analysis, the cladding and channel box thicknesses were reduced, while enrichment and pellet diameter of the UO_2 fuel were increased to match the cycle length of the full-core Zircaloy base case.

For each modification to the fuel design during the parametric study, new 2D lattice physics calculations were run for each of the 3 major axial zones to produce updated cross-section data. With the updated cross-section data, the FeCrAl full-core models were re-run until the EOC k-effective equaled that of the Zircaloy base case EOC k-effective, thus matching cycle lengths. The goal of this full-core parametric study was to establish the same bundle modifications in the FeCrAl bundles that were required in the 2D EOC Reactivity Method. Although exact matches were not expected, if similar results were recorded, then the EOC Reactivity Method would be considered verified as a quicker and useful scoping tool than full core calculations.

If alternate cladding materials were to be commercialized, nuclear utilities would not be in favor of large scale changes to the operation of the reactor. Thus, aside from the lattice physics models used to generate the lattice cross-sections and the exposure data (for thinned cladding), the full-core NESTLE model was not otherwise altered when modeling FeCrAl. Since all of the cases run maintained the same outer diameter of the fuel rod, thermal hydraulic parameters were assumed constant for both Zircaloy and FeCrAl models. Initially, an identical LP shown in case 3 of Figure 22 was used for the FeCrAl full-core model as well. These factors were kept constant in order to establish a consistent comparison between the cladding types.

IV.C.4 Loading and Control Blade Pattern Optimization

The full-core parametric study described above was used to determine the changes required of the FeCrAl fuel bundles to match cycle length requirements of the Zircaloy base case. However this base case consists of an assembly optimization pattern designed for a Zircaloy core. Therefore, in order to further optimize the FeCrAl core design neutronically, a unique LP was established using LWROpt, a computer code for optimizing assembly loading and CB patterns developed by Dr. Keith Ottinger from the University of Tennessee. LWROpt uses parallel simulated annealing for LP optimization and evaluates candidate LPs with NESTLE. Since

LWROpt is parallel, large numbers of nodal simulations can be performed until a near optimum core design is found. The quality of a LP is determined by an objective function (OF), which is calculated based on a number of weighted constraints: k-effective, nodal and radial exposure, nodal and radial relative power fraction (RPF) and assembly expense. The CB optimization uses the same OF as the LP search to evaluate candidate CB patterns but uses heuristic rules to generate CB movements.

It was determined that for this analysis, optimizing loading and CB patterns for multiple cycles simultaneously would be too computationally expensive. Therefore, the equilibrium representative BWR core for FeCrAl was initially optimized by shuffling the assembly LP, and was followed by a separate CB pattern optimization. The objective of the shuffle optimization was to find the LP with the highest possible EOC k-effective value while maintaining reasonably low RPFs. Using the Haling depletion option, a single depletion step was used for the entire cycle by assuming a constant power profile or "Haling Power Distribution" [53].

Since LWROpt does not consider start up and shutdown reactivity margins, some optimized LPs contained clusters of fresh feed assemblies. Therefore, in order to optimize the configuration on a small scale (moving a few assemblies by hand), a python graphical user interface (GUI) was created that allows the user to move assemblies one at a time. By parsing the NESLTE input and exposure files the GUI creates an initial LP, assemblies can then be added, removed and/or exchanged by dragging and dropping and a new input and exposure file can be generated and evaluated in NESTLE. Figure 23 shows a screenshot of a LP being manipulated with the GUI.

Once a shuffle pattern was established that maximized the cycle length, enrichment levels of the FeCrAl lattice could be lowered again to match the Zircaloy base case cycle length. One of the primary objectives of this dissertation was to minimize the high level of enrichment required of the FeCrAl bundles while still maintaining a proper cycle length.

Once the LP for the FeCrAl core was finalized, CB optimization for the FeCrAl and Zircaloy cores was performed. Using the CB search algorithm in LWROpt, the CBs were divided into four separate banks which were rotated with one bank being used to control the core for each depletion step. Figure 24 shows the location of the cruciform CBs color-coded according to their

CB bank for a quarter core model. Blades were inserted axially at 6-inch intervals consistent with standard commercial operation for BWRs of this size.

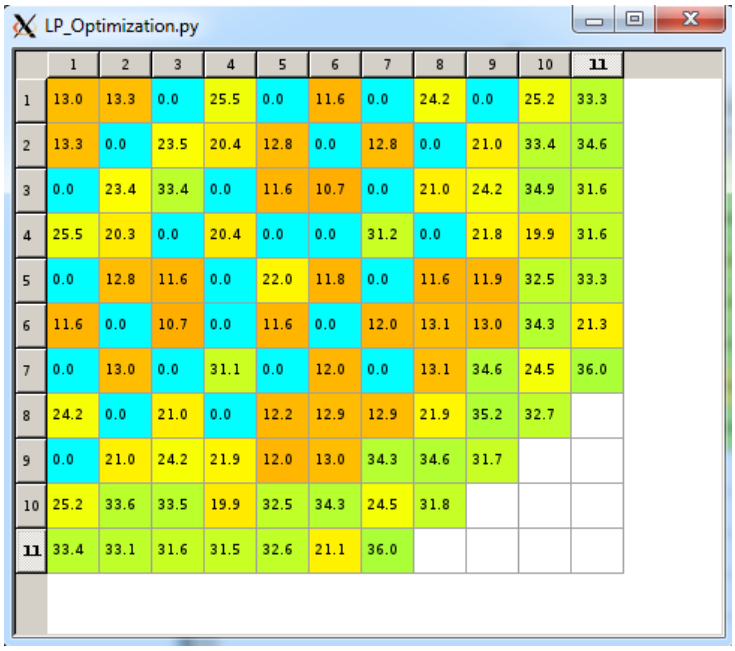


Figure 23: Loading pattern optimization GUI

The full-core NESTLE model was re-run by varying the insertion of CBs until the constraints listed in Table VII were met at each depletion step. Weighting factors were attached to each constraint in relation to its importance. Since maintaining criticality and reducing the radial RPFs were of primary concern during the CB optimization the keff and RPF constraints were given more weight than the exposure constraints.

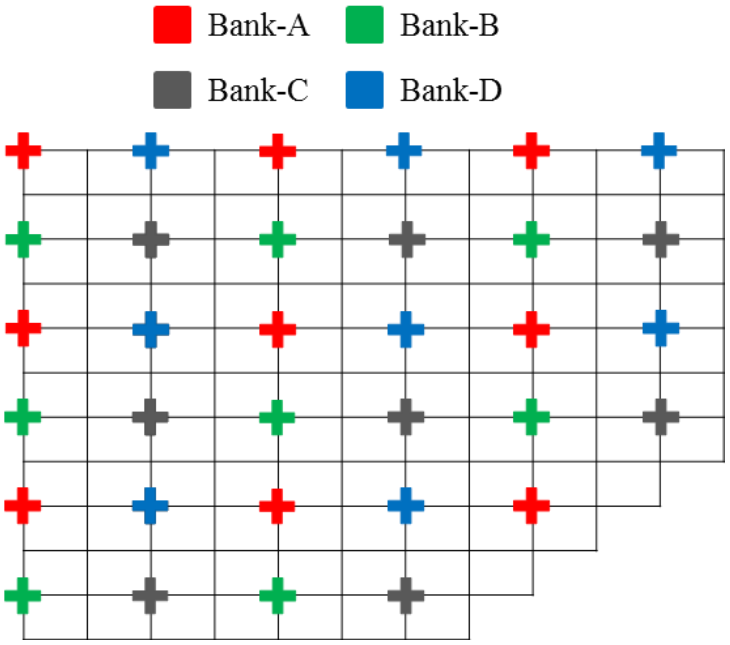


Figure 24: Control blade bank locations

Table VII: Control Blade Optimization Design Limits

Constraint	Limit
Maximum k_{eff}	1.001
Minimum k_{eff}	1.000
Radial RPF	1.6
Nodal RPF	2.0
Maximum Assembly Exposure	55 GWd/MTU
Maximum Nodal Exposure	65 GWd/MTU

IV.C.5. NESTLE Thermal Hydraulic Model

As previously stated, the nodal simulator NESTLE couples thermal hydraulic feedback effects within its criticality calculations. Therefore, coolant and fuel mechanics properties were gathered in simulating the advanced BWR design. Since the representative core shares many similarities with previously simulated reactors, some of the properties of water were gathered from existing Peach Bottom NESTLE models. In addition, throughout the alternate cladding parametric study, a fixed outer diameter was used so that the thermal hydraulic models would not be compromised when comparing designs. Therefore, the same coolant properties were used when modeling the base case Zircaloy and FeCrAl cladded cores. Table VIII lists the crucial core properties used in the thermal hydraulic model.

Table VIII. Core properties for NESTLE BWR model

Parameter	Value	Units
Bundle Pitch	6.0	in
Hydraulic Diameter	0.429	in
Flow Rate	6.15×10^7	lb/hr
Inlet Temperature	527.5	^oF
Fuel Specific Heat	0.0811	BTU/lb-^oF
Saturation Coolant Density	2.330	lb/ft^3
Coolant Saturation Energy	1192	BTU/lb
Core Pressure	1035	psia

The saturation properties for water listed in Table VIII were calculated using National Institute of Standards and Technology (NIST) [54] software with respect to the core pressure. Due to the negative MTC that exists in LWRs, the density of the coolant plays a major role in the thermalization of the neutron spectrum and thus reactivity. Thus, fluid densities were calculated by steam tables containing water properties such as temperature, pressure, entropy, etc. The temperature of the fuel pellet is heavily dependent on the power of the core at a given time step.

Therefore the average and surface temperature is calculated with polynomial equation as a function of linear power density. Once calculated, these properties are fed directly into equation 4.3 in order to update the cross-section data used to calculate the diffusion equation.

The two-phase coolant present in a BWR can be modeled in a variety of ways, ranging on the desired level of complexity. The DFM was thus chosen to simulate the flow within the thermal hydraulic model of NESTLE. As opposed to the HEM which is typically used for PWRs, the DFM does not assume that the liquid and vapor velocities are identical. However, rather than solving the mass, momentum and energy equations explicitly for both fluids, the DFM reduces the six equations down to four: continuity of mass for the vapor and the entire mixture, momentum for the mixture and energy for the mixture [55].

When calculating the energy and momentum equations, there are three different approaches available in NESTLE used to relate the void fraction of the coolant with the other known parameters. Each model was run in NESTLE, varying the coolant density of each axial zone (described in section VI.C.1.). After numerous criticality calculations were performed, the Zuber-Findlay Model (ZFM) was chosen due to its ability to reliably converge at each time step under the fluctuating condition of the representative BWR core.

IV.D. Fuel Performance Model

BISON-CASL was used when analyzing the fuel performance changes accompanying the use of FeCrAl cladding over traditional zirconium-based alloys in a BWR environment. These calculations were carried out in collaboration with another research group at UTK which specializes in fuel performance evaluations and is led by Prof. Brian Wirth. Thus, Mr. Ryan Sweet, a PhD graduate student at UTK in Dr. Wirth's research group undertook these simulations. The following section will describe how the reactor physics results from NESTLE were generated and used for eventual fuel performance analysis in BISON.

IV.D.1 Coupling BISON-CASL and NESTLE

BWR linear heat rates were taken from the NESTLE neutronics results and fit axially to a 2D-RZ fuel rod model of BISON-CASL. It was decided that the most limiting fuel rod throughout the depletion cycle would be chosen for analysis in the fuel performance code. To determine which rod was limiting, axial and radial data was taken from the NESTLE equilibrium core as well as the CASMO lattice physics results. First, the hottest burning fuel assembly was chosen in NESTLE according to the hottest radial RPF throughout the depletion. Using this assembly, the axial RPFs were gathered at each time step of the depletion sequence. These RPFs from the assembly-level were then fit to the hottest RPF fuel pin value from the CASMO depletion calculations. Multiplying the pin weighted RPF values to the average power of one fuel node effectively equated to the linear heat rate at each node at each time step.

This supplied sufficient data for the BISON-CASL model for the first cycle; however the goal of the fuel performance model was to simulate the entire life of the fuel rod. Therefore, using the EOC burnup data from the first assembly, an assembly within the equilibrium core that contained a similar BOC exposure was chosen to simulate the second cycle. This process was repeated again to produce linear heat rate values for all three 18-month cycles.

Nodal temperatures were transferred from the thermal hydraulic results of NESTLE for implementation in the fuel performance model. Throughout the depletion cycle, fluctuations in bulk coolant temperature were captured and used for boundary condition settings to establish the fuel rod temperature profile in BISON-CASL. Lastly, the peak fast fluxes were gathered from both the Zircaloy and FeCrAl CASMO models at an energy range between 1 and 10 MeV.

IV.D.2 BISON-CASL Simulations of FeCrAl and Zirconium

Using the data provided from the NESTLE full-core results, a 2D BISON-CASL simulation input and a geometric fuel rod model **(**shown in Figure 25) were developed. The fuel in the geometric model is simplified by using a single smeared fuel pellet spanning the length of the rod. Red cells indicate the UO_2 fuel region while blue represents the cladding.

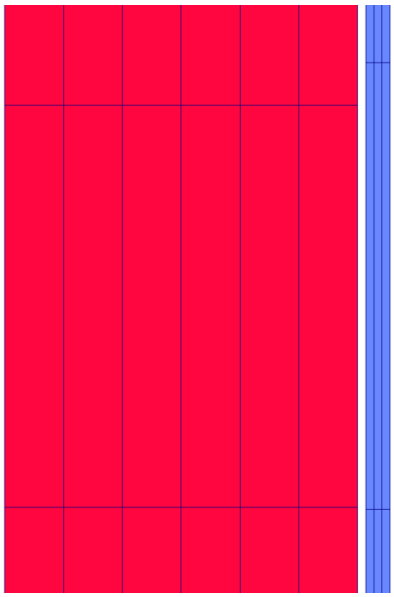


Figure 25: Mesh of smeared pellet fuel rod model with 300 μm cladding

BISON-CASL simulations utilize the provided power history and axial peaking factors of the fuel rod to determine to the power produced in the fuel rod at a specific time. This, in turn, allows the temperature to be calculated along with other dependent material properties through the lifetime of the fuel. To simulate the UO_2 fuel, these properties were determined using previously developed models including; NFIR data on thermal properties based on temperature and burnup dependence; temperature dependent mechanical properties; fuel swelling, densification, and relocation; thermal and irradiation creep; and fission gas release. The gap and plenum regions of the fuel are modeled by heat transfer from the fuel to the clad and an applied pressure on the inside of the cladding and outside of the fuel which is based on the composition and amount of fission gas released into the regions as well as the volume that it occupies. Models used for the Zircaloy cladding include thermal and mechanical properties based on temperature dependence, thermal and irradiation creep, and irradiation growth [26].

In order for BISON-CASL to simulate different materials, models of these materials must be created first. These models contain data about the chemical, mechanical, and thermal properties

of the material, and are as complex or simple as the situation warrants. Material models for FeCrAl were made using datasheets for several FeCrAl alloys [41]. Various material properties were taken and fit to curves based on its dependencies for use in the BISON-CASL models. These models are based on available thermophysical, mechanical, and irradiation properties and include thermal conductivity, specific heat, elastic modulus, density, thermal strain, and irradiation swelling among others [26].

Three simulations were run using BISON-CASL to analyze differences in the fuel performance between FeCrAl and traditional Zircaloy cladded fuel elements during normal reactor operation. The simulations are designed to demonstrate the irradiation swelling effect in FeCrAl cladding, as well as Zircaloy cladding to allow a comparison of the two cladding types. The axial and radial displacements are useful for determining if the cladding will expand or swell too during operation. If the cladding elongates excessively in the axial direction, the fuel risks bowing or deforming due to size constraints; if the cladding radius increases too much, the fuel risks increased contact with the fuel assembly spacer grid and possibly increased fretting wear. The fuel rods geometries were generated based on the rough specifications of the representative BWR core, and the expected requirements of using a FeCrAl alloy (Shown in Table IX).

Table IX: Fuel performance geometry specifications

Cladding Type	Fuel Radius (microns)	Gap Thickness (μm)	Cladding Thickness (μm)	Fuel Length (m)	Cladding Length (m)	Enrichment (% U-235)
Zircaloy	4400	100	600	3.66	4.08	4.11
FeCrAl	4700	100	300			4.68

For the preliminary comparison of the FeCrAl alloy simulations and the Zircaloy simulations the peak fuel centerline temperature, the axial and radial elongation, and the gap closure time were

compared. Determining the fuel centerline temperature is useful in fuel performance to gauge how close the UO_2 fuel is to its melting temperature (~3100K). As the fuel reaches the melting temperature, it will begin to deform and compromise the fuel geometry. The onset of gap closure is important because it marks the onset of phenomena including increased heat transfer from the fuel to the cladding by eliminating the gap. This in turn increases tensile azimuthal stresses in the cladding as the fuel is adds additional forces to the inner surface of the cladding.

V. PWR RESULTS

The following section presents work completed on ATFs in PWR environments: FCM fuel and alternate cladding concepts. The section begins with pin cell level calculations which include a parametric study optimizing both fuel forms to meet reactivity lifetime requirements of standard PWR fuel. Neutron flux analysis was completed revealing spectral shifts in the fuel as a function of exposure. Moderator reactivity coefficients and void fractions of the alternate cladding materials were compared to standard Zircaloy cladding. Finally, moving on to lattice level calculations, pin peaking and power sharing comparisons were made between FCM fuel and standard UO_2 pellet fuel assemblies. It is very important to note, all results pertaining to FCM fuel were done using Zircaloy cladding. Whereas, results pertaining to alternate cladding materials were done using UO_2 fuel pellets. The two studies were done completely independent of one another and do not overlap in any way.

V.A. Preliminary Pin Cell Calculations

V.A.1 Assessment of Insufficient Reactivity in FCM Fuel

Single pin cell calculations were performed using SCALE to compare the UO_2 FCM design to that of a standard PWR pin cell. Initially, the multiplication factor of the FCM fuel was plotted vs exposure by varying the KD from 500 to 1,000 μm. By increasing KD and keeping the outer layer thicknesses constant (buffer layer (BL) = 100 μm, IPyC = 35 μm, SiC = 35 μm, and OPyC = 40 μm), the PF of the fuel to the matrix and particle materials increases. This allows more fuel to be inserted and is advantageous in attempting to maximize the reactivity of the fuel. Given fuel fabrication and performance considerations, increasing KD beyond 1,000 μm was not considered.

Figure 26 provides the results of the calculations, presenting the differences in the multiplication factor by increasing KD. With UO_2 fuel, none of these cases provided sufficient reactivity to

obtain an 18-month batch cycle. It is not possible to load sufficient fissile fuel with these fuel design parameters.

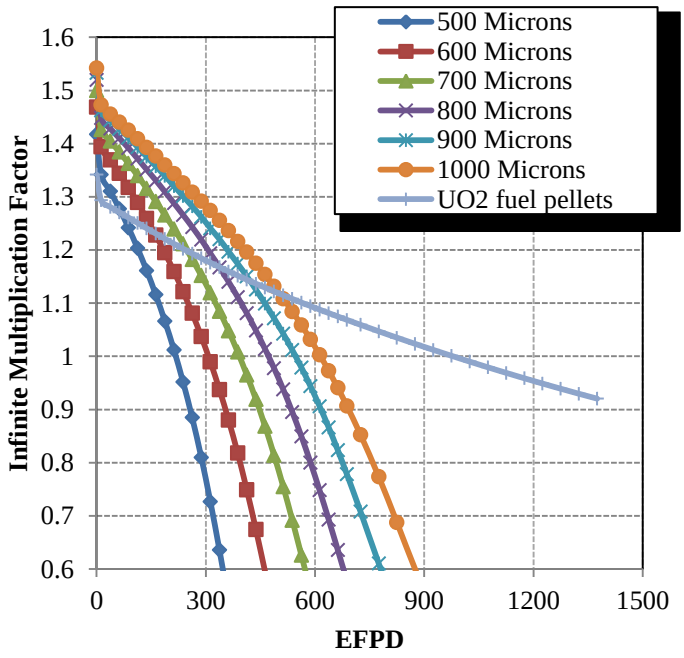


Figure 26: Infinite Multiplication factor vs effective full-power days for a range of UO2 kernel diameters

To obtain higher uranium loadings, UN and mixed UCO kernels were simulated with identical geometries to those of the UO_2 FCM fuel. As shown in Figure 27, UCO fuel, with a slightly higher density of 10.924 g/cm^3 [56] (9.77 g U/cm^3), versus 10.50 g/cm^3 (9.26 g U/cm^3) for UO_2, did not provide a significant increase in fuel cycle length. However, UN, with a density of 14.33 g/cm^3 (13.53 g U/cm^3), provided 40% greater uranium density than UO_2. This increased uranium density coupled with an increase in KD, while maintaining constant coating layer thicknesses significantly increased the amount of fissile material in the particle. Figure 27 illustrates the reactivity differences between the three uranium-based fuels while holding KD constant at 1,000 μm.

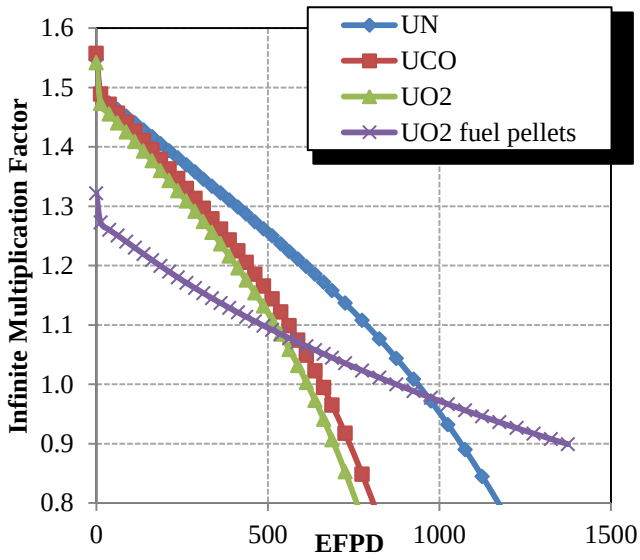


Figure 27: Infinite Multiplication factor with alternative uranium-based FCM fuels

The results in Figure 27 indicate that UN outperforms the other FCM fuels on the basis of reactivity; thus, UN chosen as the primary fuel in the FCM design for the remainder of this work. It should be noted that there remains a rapid drop-off in k_{inf} from around 750 EFPD that occurs because of the lack of plutonium in FCM fuel compared with the standard UO_2 pellet case.

V.A.2. Reactivity Penalty of Alternate Cladding Concepts

Figure 28 displays the neutronic penalty/advantage associated with utilization of alternate cladding materials as a function of EFPD. For this initial calculation, fuel rods were modeled with a standard PWR 17 × 17 geometry. All cases were depleted for 1,475 EFPD to encompass the expected value (1,420 EFPD) after three 18-month cycles in PWR. The differing neutron absorption properties are easily shown in this figure when viewing the large difference in k-infinity between the alternate cladding concepts and the Zircaloy reference case.

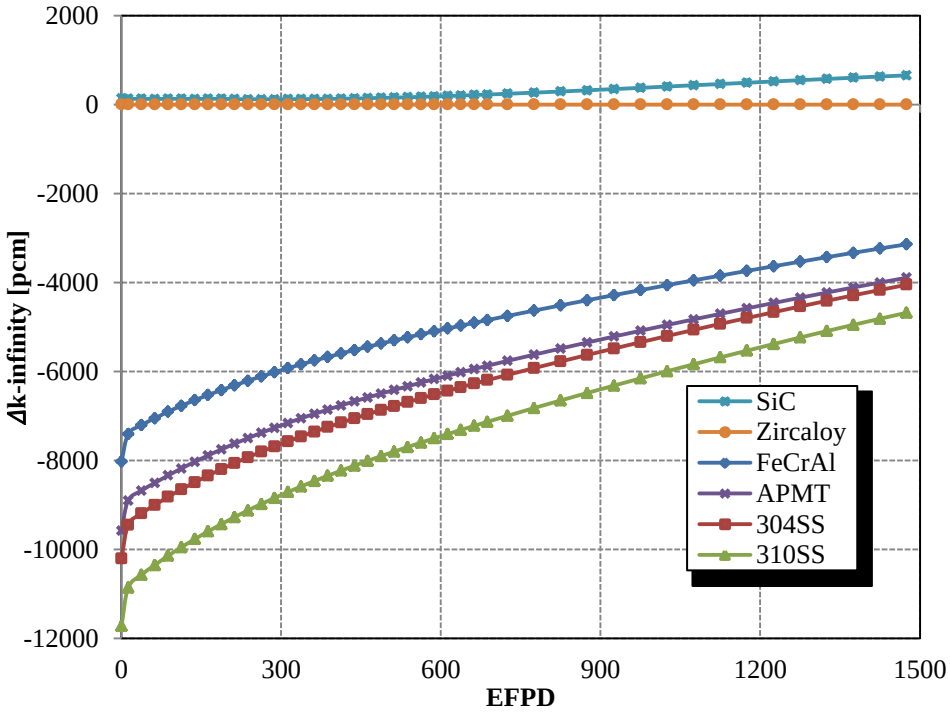


Figure 28: Δk-infinity from Zircaloy-4 clad fuel vs. effective full power days

The drop in reactivity found for 310SS, 304SS, APMT^{TM}, and FeCrAl corresponds to a significant reduction in operational cycle length. As shown in Figure 28, Δk-infinity for those cladding materials decreases throughout the cycle. This phenomenon is due to increased plutonium breeding throughout the cycle in the presence of a harder neutron spectrum, and will be further analyzed in Section V.C.2. The reactivity penalties at the end of three 18-month cycles for austenitic stainless steels (304SS and 310SS) were found to be -4.2% and -4.8% Δk-infinity respectively, while the ferritic alloys (FeCrAl and APMT^{TM}) were slightly less negative at -3.2% and -4.0%. The less absorbing SiC cladding produced a positive 0.6% Δk-infinity at EOL.

V.B. Parametric Study Matching Reactivity Lifetime Requirements

V.B.1 FCM Particle Geometry Manipulation

Despite using the high-density UN fuel in a 1,000-μm fuel kernel, reactivity lifetime requirements were not met with the initial particle geometry and matrix specifications when comparing FCM fuel to standard UO_2 pellet fuel. Therefore, variations in the particle layers and PFs were evaluated to increase the volume fraction of the fuel region. Limiting values for these augmentations suggested by fuel fabrication experts have been deemed largely inconsequential to fuel performance under irradiation. By increasing the fuel KD and PF and decreasing the surrounding BL, a greater uranium loading can be achieved, thus increasing reactivity and fuel cycle length while maintaining sufficient volume for fission gas accumulation.

Due to the significantly lower amount of ^{238}U per unit volume of the FCM core, plutonium production during reactor operation is significantly reduced. As will be discussed later, the ^{235}U density per unit volume of the core is comparable to that of conventional oxide-fueled LWRs (given the high enrichment in FCM fuel). However, the reduction in ^{238}U results in reduced plutonium breeding. Accordingly, the reactivity of the FCM fuel drops sharply compared to typical LWRs due to a reduction in the fission contribution from the ^{239}Pu.

To investigate the impact of operating cycle length with fuel loading, numerous variations of the FCM design were considered by changing the PF, BL thickness, and KD. BLs of 50 and 100 μm were considered. By reducing the BL, the volume fraction of the fuel is increased within the particle, thus allowing additional HM in the system. PF was varied between 45% and 50%, and the fuel KD was varied from 800 to 1,350 μm. A total of 10 cases were analyzed in combination. The second, third, and fourth particle layers were held constant at 35, 35, and 40 μm, respectively, for all cases to maintain the structural integrity of the particle.

Using the Equivalent Reactivity Model, 10 FCM fuel cases (Table IX) were modeled and compared with a 5% enriched UO_2 PWR pin cell. This enrichment is the maximum currently licensed and is assumed to be representative of today's operating reactors that operate 18-month cycles.

Table X. Fuel Cycle Reactivity Models

	1	2	3	4	5	6	7	8	9	10
Kernel Diameter (µm)	800	800	1000	1000	1350	800	800	1000	1000	1350
Buffer Layer (µm)	50	100	50	100	100	50	100	50	100	100
Packing Fraction	45%	45%	45%	45%	45%	50%	50%	50%	50%	50%

By applying the Equivalent Reactivity Model to the multiplication factor results, the net EOC reactivity was plotted in Figure 29 as a function of KD. When the estimated EOC net core reactivity difference between the FCM and the standard UO_2 fuel is equal to or greater than zero, the design is expected to have sufficient fissile fuel to match three 18-month batch cycles. This breakeven point is represented by a thick horizontal line at 0.000 in Figure 29.

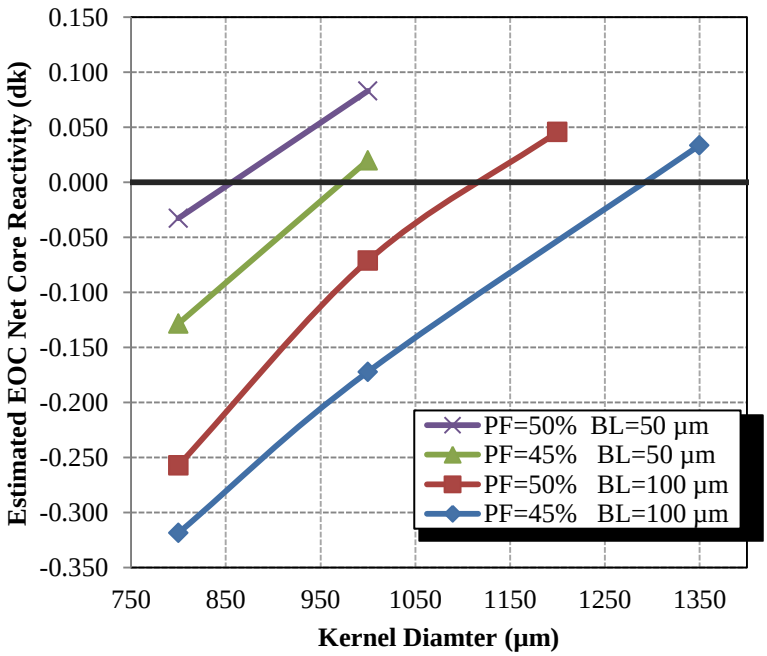


Figure 29: EOC net core reactivity vs kernel diameter for several PFs and BLs

When KD and PF are increased and the carbon buffer region is decreased, the overall volume fraction of the fuel kernel increases. This in turn allows for more HM to be included per unit volume of the core. As shown in Figure 29, when the BL is set at 100 µm or the PF at 45%, the KD required to reach equivalent core reactivity is increased. A discussion on maximum PF for coated fuel particles inside a graphite matrix is offered by Morris and Pappano [57]. Although PFs above 40% are noted to be possible, they are deemed challenging from a fuel fabrication standpoint.

To quantify the results on a basis of fuel mass, the amount of fissile fuel per design was chosen as the independent variable, represented in Figure 30. For each case, the fissile fuel content was calculated and plotted on the abscissa versus EOC net core reactivity. Again, the location on the x-axis where the linear regression line crosses the breakeven line corresponds to the amount of fissile material required to reach the equivalent lifetime of a typical PWR.

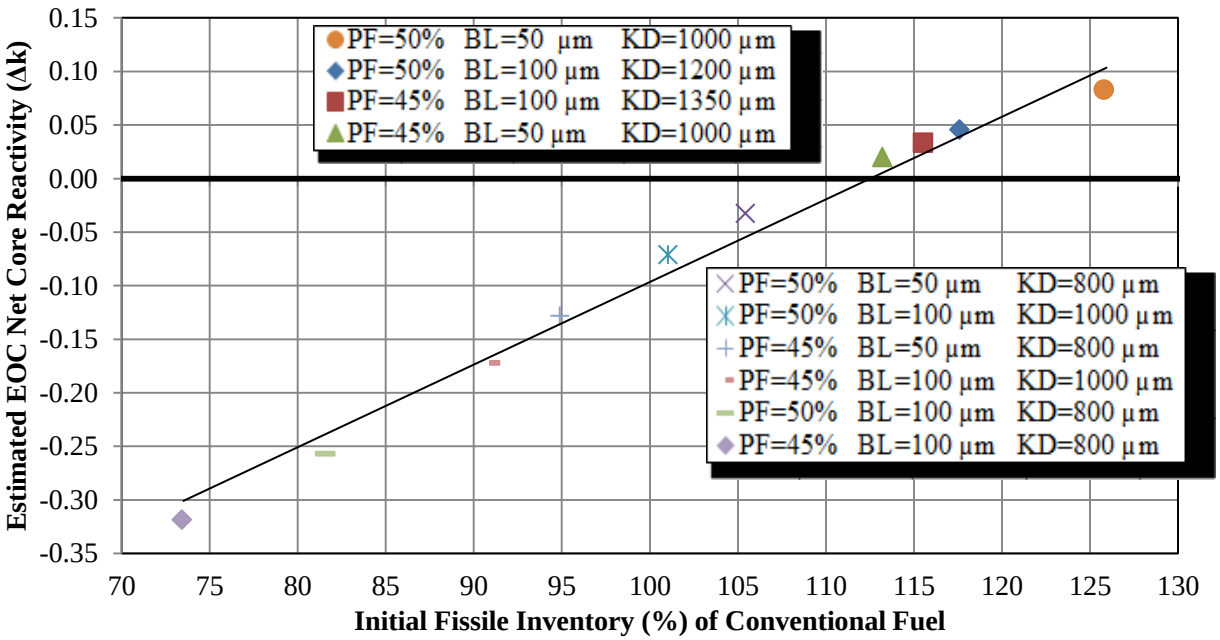


Figure 30: EOC net core reactivity vs initial fissile fraction

Figure 30 shows a distinct linear trend throughout the 10 cases, signifying that EOC net reactivity is affected not by the details of the mechanical design of the fuel particles and their PFs but primarily by the amount of fissile material present. This is an important observation that assists fuel developers in engineering the fuel compact through an optimized balance of KD, coating layer thicknesses, PFs, and even rod diameter. Following this trend line, it is concluded that 19.75% enriched FCM fuel would require approximately 10% more fissile material than a 5% enriched PWR lattice for the fuel to reach three 18-month PWR cycles. A reactor containing solely FCM assemblies at 19.75% enriched uranium would equate to 511 grams of total uranium per rod (radius of 0.412 cm) or 140 kg of uranium per assembly (in comparison to about 450 kg uranium per assembly for standard PWR fuel). Although the mass of ^{235}U in the core between the two fuel concepts is roughly the same, the ^{238}U mass has been significantly reduced. This results in much lower plutonium breeding and much larger burnups per unit mass of HM in FCM fuel. Similar results were recorded in a study done by R. A. Shapiro when analyzing various ATFs [58].

Although only 10 FCM geometries are shown here, other combinations have been tested that meet the 110% fissile material criteria to achieve three 18-month cycles of operation. Consistent results have shown that reasonable combinations of BL, PF, KD, and even fuel rod diameter that supply sufficient fissile material mass (110% fissile material criteria) will produce an EOC net core reactivity equivalent to that of a typical PWR.

V.B.2. Modifications of Alternate Cladding Thickness and Fuel Enrichment

To enhance the reactivity and increase the cycle length for those materials, modified fuel rod geometries or increased enrichment in the fuel are necessary. Accordingly, fuel rod designs conforming to Cases 2–8 in Table III are considered for alternate cladding concepts. For SiC, the cladding thickness was also increased in Case 9 to be representative of the thicker cladding structures demonstrated to date for SiC-based materials.

Table X displays the $\overline{\Delta k}_{core}$ corresponding to each cladding material for Cases 1–9. The specific power in MW/MTU corresponds to the constant power of 18.0 MW/assembly modeled through the depletion cycle. Positive and equivalent $\overline{\Delta k}_{core}$ values with respect to the reference case

(Case 1 with 4.9% enriched urania in Zircaloy-4 cladding) are highlighted in Table X. When the difference is zero, identical cycle lengths to the reference scenario are achieved.

Table XI. Cycle Reactivity Difference [Δk_{core}] for Alternate Fuel Cladding Concepts from the Reference PWR Fuel with Zircaloy-4 Cladding

Case #	Clad Thickness (μm)	^{235}U Enrichment	Specific Power (MW/MTU)	304SS	310SS	FeCrAl	APMT^{TM}	SiC
1 (ref)	571.5	4.9%	38.33	-0.054	-0.062	-0.042	-0.052	0.004
2	500	4.9%	37.03	-0.041	-0.048	-0.030	-0.038	-
3	400	4.9%	35.31	-0.023	-0.028	-0.014	-0.021	-
4	300	4.9%	33.71	-0.006	-0.010	0.001	-0.005	-
5	571.5	5.5%	38.33	-0.027	-0.036	-0.015	-0.025	-
6	571.5	6.0%	38.33	-0.006	-0.015	0.006	-0.004	-
7	571.5	6.5%	38.33	0.014	0.005	0.026	0.016	-
8	571.5	7.0%	38.33	0.033	0.024	0.045	0.035	-
9	889	5.5%	45.04	-	-	-	-	0.000

Note: Positive and equivalent $\overline{\Delta k_{core}}$ values with respect to the reference case (Case 1 with 4.9% enriched urania in Zircaloy-4 cladding) are in highlighted cells.

Upon decreasing the cladding thickness and increasing the UO_2 fuel pellet volume by nearly 14%, FeCrAl was the only metallic alternate cladding material to meet lifetime requirements while maintaining a constant 4.9% fuel enrichment. SiC, which has slightly lower neutron absorption than Zircaloy (shown in Table I), exceeded 0.000 without any geometric alterations to the base case conditions. When setting up a conservative SiC model with a cladding thickness of 889 microns, increasing enrichment to 5.5% adds sufficient fissile material to meet lifetime requirements. Combinations of decreased cladding thickness and enrichment were investigated next.

The necessary enrichment to match the fuel cycle length of the reference case was calculated in this section for various alternate cladding concepts. Given the higher strength of iron-based alloys when compared to zirconium-based alloys, a reduced cladding thickness of 350 μm was considered for these cases. This is consistent with historic utilization of these materials as fuel

cladding in LWRs [22]. The cladding thicknesses for the SiC and Zircaloy cases were kept at 571.5 μm, which represents a typical thickness for a Westinghouse PWR fuel rod. Although a broad range of alloys was initially considered, the subsequent calculations will focus on Zircaloy, FeCrAl, 310SS, and SiC as cladding materials.

Therefore, with these new geometric properties, enrichment was interpolated until an EOC value of 0.000 (+/- 0.001) was obtained from the respective k-infinity results. After multiple iterations, the enrichment and geometry combinations shown in Table XI were used for the remaining neutronics calculations. For all cases, an outer rod diameter of 0.94996 cm was kept constant, therefore maintaining a pitch-to-rod ratio of 1.326 so that the thermal hydraulics in the PWR system would not be affected drastically if commercialized.

Table XII. ^{235}U Enrichment Matching Cycle Length Requirements

	Cladding Thickness (μm)	**Required ^{235}U % Enrichment for Equivalent EOC Value (0.000)**
Zircaloy (Standard Fuel)	571.5	4.90
FeCrAl	350.0	5.06
SiC	571.5	4.81
310SS	350.0	5.39

Cladding materials 310SS and FeCrAl were modeled with an increased pellet diameter and reduced cladding thickness, while maintaining a constant pellet-clad gap thickness. This allows for increased heavy metal loading, thus reducing the ^{235}U enrichment required to match PWR cycle lengths when using Zircaloy. Because of reduced neutron absorption in the clad for SiC, a reduction in enrichment below 4.9% was possible while matching the reference EOC k-infinity.

In addition to interpolating enrichment with a fixed cladding thickness, the necessary cladding thickness for each material to achieve identical EOC k-infinity to that of the base case was also

interpolated by fixing the enrichment of the UO_2 fuel at 4.9% ^{235}U. Table XII provides the cladding thicknesses required for a 0.000 (+/- 0.001) EOC value. The amount of clad thinning presented in the following table is done purely on a neutronics basis to match lifetime requirements and does not account for the thermo-mechanical fuel performance constraints of the cladding concepts (e.g., maintaining cladding integrity during operations).

Table XIII. Cladding Thickness Matching Cycle Length Requirements

	^{235}U % Enrichment	**Cladding Thickness (µm) Required for Equivalent EOC Value (0.000)**
Zircaloy (Standard Fuel)	4.90	571.5
FeCrAl	4.90	302.2
SiC	4.90	606.7
310SS	4.90	226.3

The geometric and enrichment specifications from Tables XI and XII were gathered into a single plot, Figure 31, representing all simulations with parameter combinations expected to meet reactivity lifetime requirements in a PWR environment. The blue data point at the intersection of the abscissa and ordinate represents the Westinghouse 17 × 17 base case Zircaloy pin containing 4.9% enriched uranium and a cladding thickness of 571.5 µm. Fitting the data, a linear trend is shown when modifying fuel parameters. Any combination of enrichment and cladding thicknesses left and upward of the linear trend line shown for each material is expected to meet or exceed cycle length requirements.

As mentioned previously, 310SS and FeCrAl contain elements with higher neutron absorption than Zircaloy; if enrichment is kept constant, a greater heavy metal loading is needed for these materials to match the cycle length of Zircaloy. This is achieved by using a thinner cladding while maintaining a constant P/D. Increased levels of ^{235}U enrichment also could help maintain the cycle length achieved by Zircaloy, but additional enrichment will increase fuel fabrication

costs. From a safety and economic standpoint, data points closer to the bottom right of the plot signify fuel parameters that are more desirable because the enrichment and total heavy metal loading in the fuel are lowest, and clad integrity should be highest.

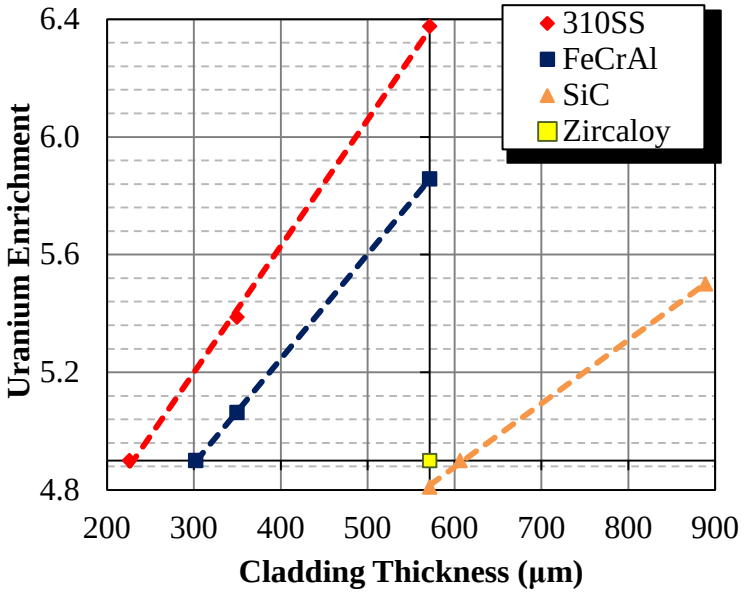


Figure 31: Fuel parameters required to match the PWR lifetime

V.C. Spectral Results

V.C.1. FCM Flux Spectra Evaluation

The neutron flux spectra of FCM fuel and conventional PWR UO_2 fuel were compared at BOL, MOL and EOL. A depletion model was run first to output the isotopic inventory of the fuel regions at each time step for both models. In the FCM model, TRISO particles were modeled in SCALE with an 800 µm diameter fuel kernel and standard coating thicknesses: 70 µm buffer, 35 µm IPyC, 35 µm SiC and 35 µm OPyC layers. These TRISO dimensions are similar to the design

specifications used in previous studies [12]. A 42% PF of particles to SiC matrix was modeled with enlarged fuel rods at a radius of 0.558 cm. An enlarged fuel radius was used so that sufficient fissile material was present to match lifetime requirements of a UO_2 fuel rod. Thus a fair comparison between spectra could be made between FCM and standard fuel. Using the resulting isotopics, the neutron flux was calculated across a plane perpendicular to the axial direction of the rod at the center spanning across the entire cell (fuel, cladding, and moderator). Normalized flux per unit lethargy was thus plotted at the aforementioned time steps, and spectral hardening throughout the lifetime was analyzed.

Focusing on the thermal peaks at 0.1 eV, a definite spectral shift is shown throughout the lifetime of the fuel. The FCM thermal peak is significantly lower than conventional UO_2 fuel at BOL until a gradual shift occurs where the thermal peak of the FCM fuel becomes greater at EOL. As Figure 32 contains normalized values, it is clear that the FCM spectrum is softened from BOL to EOL, while the conventional UO_2 fuel spectrum appears to harden. This is because at BOL, the FCM fuel has about 10% more fissile material than conventional fuel, and thus thermal neutrons are being absorbed at a greater rate. However near EOL, the fissile inventory in the FCM fuel is drastically depleted, while the conventional fuel is breeding significantly more plutonium. This reduction of highly absorbing isotopes in the FCM fuel causes the inventory of thermal neutrons to increase near EOL, while the increased plutonium inventory in standard UO_2 fuel causes its thermal spectrum to harden.

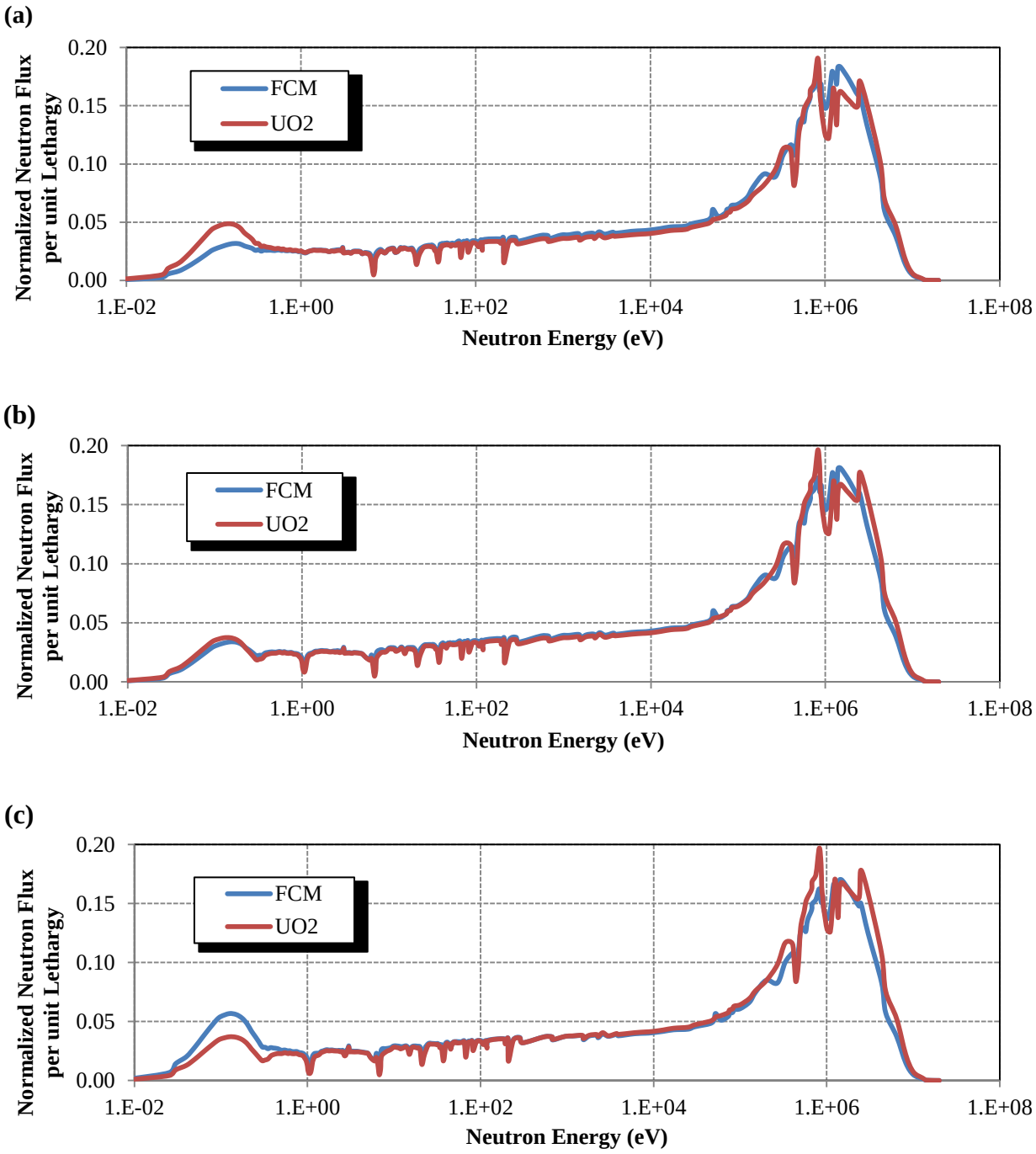


Figure 32: Average scalar flux throughout fuel lifetime: BOL (a), MOL (b), and EOL (c)

V.C.2. Alternate Cladding Spectral Hardening

Spectral hardening was investigated next for the Fe-based, SiC and Zircaloy cladding materials under consideration. For this study, the neutron flux was calculated across a plane perpendicular to the axial direction of the rod at the center height spanning across the entire cell (fuel, cladding, and moderator). Lethargy was then calculated for each point so that the normalized flux per unit lethargy could be plotted at each of the 238 energy groups. Figure 33 corresponds to the flux spectra at BOL.

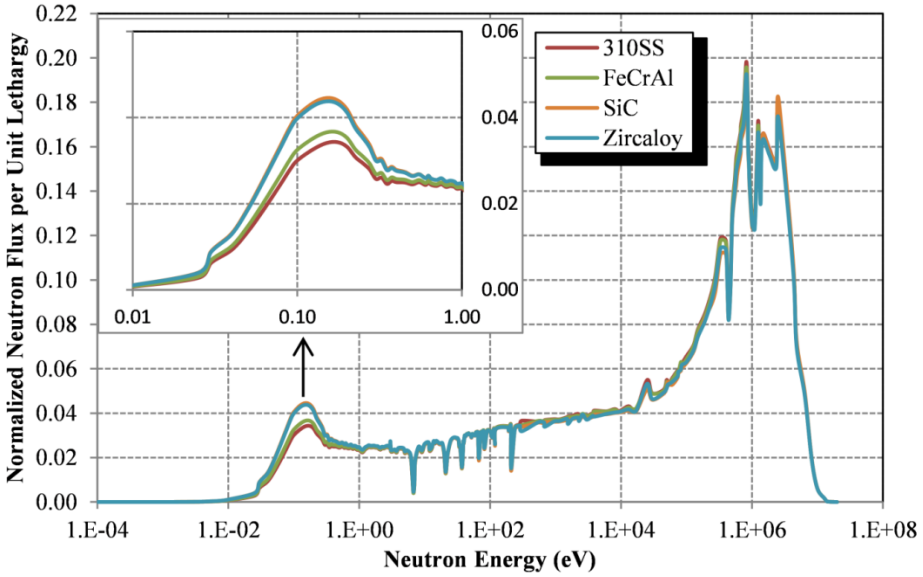


Figure 33: Neutron flux spectrum at BOL

The spectrum also was plotted at MOL and EOL. Analysis of the thermal peaks indicates that cladding materials containing higher absorbing isotopes produce a harder neutron spectrum throughout the depletion cycle. More thermal neutrons are being absorbed in the FeCrAl and 310SS cladding; therefore, the fraction of fast neutrons in the system increases. Thus, the thermal peak shown in the top left corner of Figure 33 is lower for the higher absorbing materials and higher for Zircaloy and SiC. For all four cases, a hardening of the spectrum was found from BOL

to EOL as the thermal peaks at 0.1 eV decrease and the fast peaks at 1 MeV increase. This phenomenon is due to the depletion of overall fissile material and, in turn, an increased accumulation of fission products and actinides in the system.

V.D. Reactivity Coefficients

In keeping with the safety standards of operational PWRs, it is imperative that each cladding material maintains negative moderator and void coefficients. Because only minor changes were made to the fuel enrichment, the Doppler coefficient was expected to be consistent with that of standard PWR fuel and was therefore not investigated in this study. Thus, moderator temperature and void reactivity responses were calculated for each alternate cladding case by perturbing the conditions of the coolant. To simulate the effective density changes of water for each temperature perturbation, a Fluid Properties Database Program from the NIST was used [54]. When simulating the presence of superheated steam in the coolant, the density of water was decreased by the fraction of the void in the system. Table XIII summarizes the temperature and density perturbations made for each alternate cladding study. Perturbations branch from the nominal base case conditions, which are a moderator temperature of 580 K (0.7119 g/cm^3) and 0% void. In all of the cases, the boron concentration was maintained at the average conditions of 630 ppm, and therefore the analysis is for representative fuel burnups rather than for accurate operating conditions; that effect is observed independently below.

To change the temperature and density parameters throughout the depletion cycle, branch perturbations were run in the SCALE model. Rather than deplete the fuel separately with each change in moderator property, a nominal model was run with the base conditions described above. From there, the isotopics of the nominal model were used at each timestep simulating instantaneous perturbations. Table XIV represents the MTC at BOL, MOL, and EOL. For these calculations as well as the remaining spectral and radial analyses done in later sections, thickness and enrichment specifications were taken from Table XI.

Table XIV. Reactivity Safety Coefficient Perturbations in Moderator

Moderator Temp Coefficient		Moderator Void Coefficient	
Temperature (K)	**Density (g/cm^3)**	**Void (%)**	**Density (g/cm^3)**
560	0.7521	**0%**	**0.7119**
570	0.7329	5%	0.6763
575	0.7227	10%	0.6407
580	**0.7119**	20%	0.5695
585	0.7005	40%	0.4271
590	0.6883	60%	0.2848
600	0.6612	80%	0.1424

Note: Nominal conditions are in bold.

Table XV. Moderator Temperature Coefficient Map Throughout Depletion (pcm $\Delta\rho$/°F) with an 18° F Change in Coolant Temperature

	BOL	**MOL**	**EOL**
Zircaloy	-14.8	-25.8	-34.5
310SS	-16.9	-25.9	-34.4
FeCrAl	-16.5	-26.1	-34.5
SiC	-14.4	-25.5	-34.1

These results show a negative MTC for each cladding material for a range of fuel burnups. As the fuel is depleted, less fissile material is present in the system, making reactivity more sensitive to changes in the moderator temperature and thus number density of water molecules. If a traditional boron letdown were to be simulated per cycle, the MTC at BOL would be less negative because of the additional boron in the moderator. Conversely, the MTC at EOL would be more negative because of the near zero boron concentration in the system. The analysis initially was done at a constant boron level (630 ppm) to compare each cladding material relatively at a range of fuel burnups. Because the limiting case for MTC is when the boron

concentration is highest during the cycle, the BOL coefficient was calculated for each case with 1,300 ppm boron, which is representative of BOL boron conditions for a modern PWR. As expected, MTC for each alternate cladding material was slightly more positive with additional boron. Consistent to Table XIV, SiC and Zircaloy produced the least negative MTC values at -9.4 and -8.8 pcm/°F, respectively, while 310SS and FeCrAl were slightly more negative at -12.2 and -11.6 pcm/°F, respectively.

In analyzing the void coefficient, the change in k-infinity upon the onset of superheated steam in the coolant was analyzed for each clad material. A steady decrease in k-infinity was found when the void fraction in the system coolant was increased. The minimal variance that was found among all four cases, including the Zircaloy base model, indicates that each cladding material will maintain operational standards similar to the other materials.

V.E. FCM Lattice Power Peaking Calculations

An important part of determining the suitability of a nuclear fuel design is the ability to obtain acceptably low fuel-rod power peaking. If individual pins from an array are more reactive than the others, hot spot locations can arise, which reduces the design margin to thermal limits. Although unrealistic, a completely flat profile across the lattice would be ideal for control of the reactor. Using the RPT method to model the FCM fuel, relative pin powers were plotted in a quarter lattice. A maximum peaking value of 1.043 was recorded for the FCM design, representing excellent power sharing across the FCM assembly compared to the standard UO_2 with a maximum peaking rod of 1.055.

Similarly to the pin peaking in a fuel lattice, maintaining relatively equal power sharing from lattice to lattice is also crucial in the operation of an LWR. After depleting a quarter lattice for one cycle, the isotopics can be inserted into a new input file as a once-burned lattice. Combining a once-burned and a fresh-feed lattice into one checkerboard-type color-set is a useful way to determine how power is distributed in a given cycle. Once again, a flatter distribution between lattices is desirable; however, it is not expected that a depleted once-burned lattice would

produce the same power-sharing factors as a feed lattice. Figures 34 and 35 represent power-sharing color-sets for UN FCM fuel and a standard PWR UO_2 fuel, respectively, at BOC.

Because the FCM fuel contains higher enriched uranium with less overall uranium mass, the fuel tends to deplete more rapidly, which results in a larger deviation of pin peaking between the first, second, and third cycles than in typical UO_2 fuel. As shown initially by Figure 26, the FCM fuel designs maintain higher levels of reactivity early in life and much lower near end of life (EOL). This is opposed to the flatter and steadier 4.5% enriched PWR pellet geometry. In Figs. 21 and 22, the standard UO_2 fuel maintains a flatter power-sharing distribution over the lattice than the FCM lattice. Although the PWR lattice shows a visibly flatter profile than the FCM fuel near the center of Figs. 21 and 22, the average PWR cells across the fresh-feed and once-burned lattice are similar to those of the FCM color-set. By weighting the pins in both batches, it was found that the FCM fuel averages 1.134 and 0.866 for the fresh and once-burned lattices, respectively, as opposed to the standard PWR pellet fuel averages of 1.109 and 0.891, respectively. As the 500-EFPD cycle continues, the PWR and FCM distributions both converge toward unity at EOC. However, the weighted average across the fresh-feed quarter lattice after depleting the color-set for one cycle is 1.148 for the FCM lattice, remaining slightly higher than the UO_2 average at 1.081.

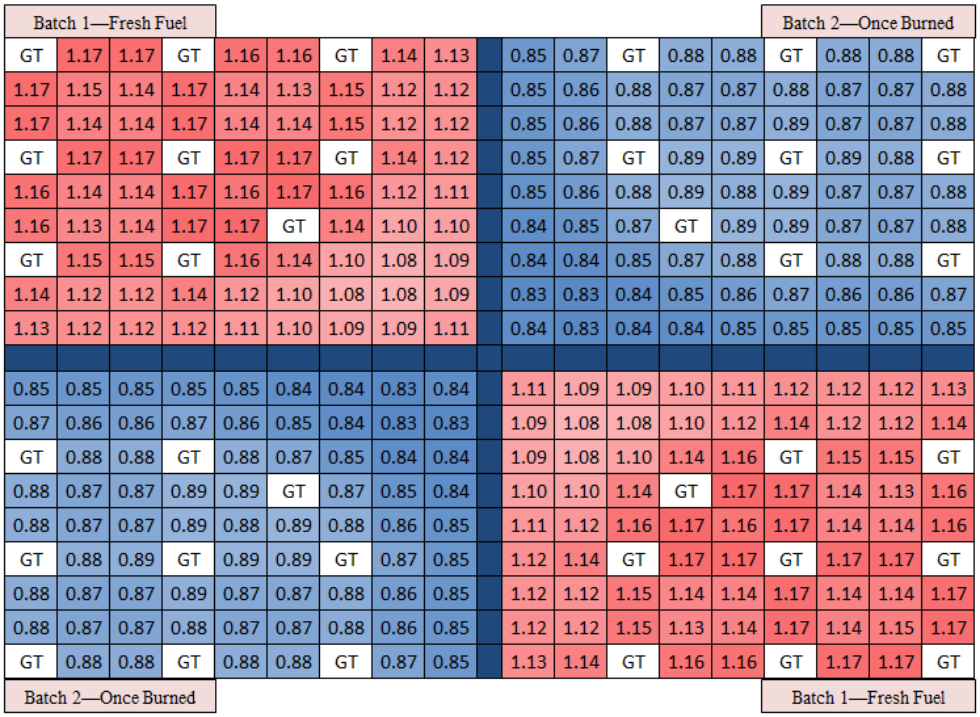


Figure 34: Uranium mononitride FCM fuel power-sharing color-set

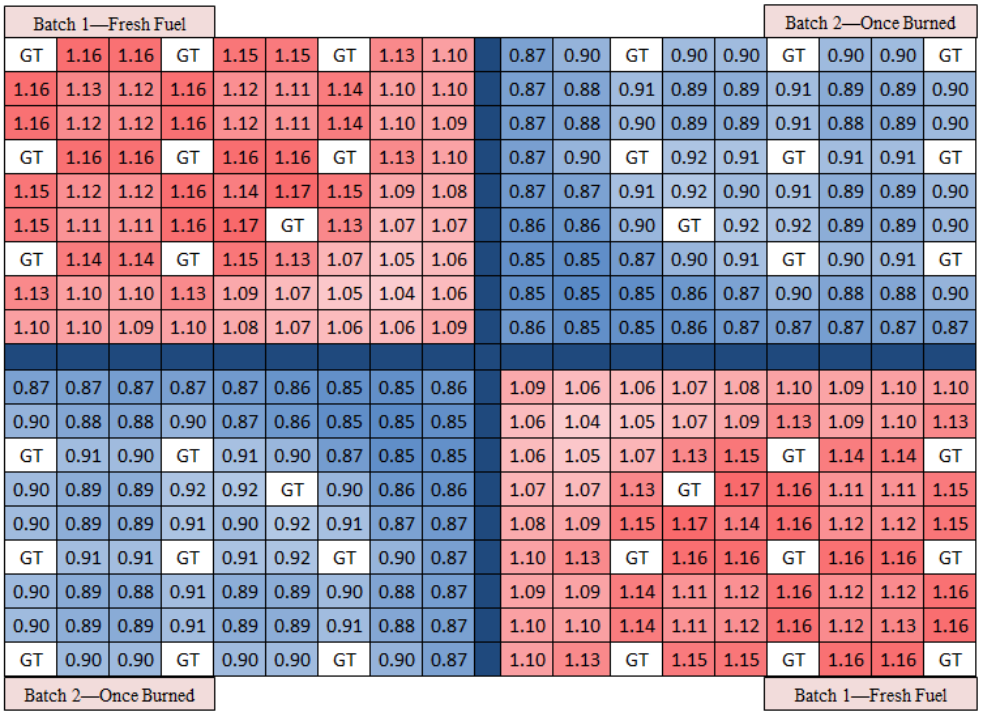


Figure 35: Standard PWR UO2 pellet-based fuel power-sharing color-set

VI. BWR RESULTS

The following section presents the neutronic, thermal hydraulic and fuel performance results for alternate cladding material in a BWR environment. Lattice physics results will demonstrate the initial reactivity penalty/advantages when replacing the Zircaloy cladding and channel box with FeCrAl and SiC. 2D parametric evaluations will determine the geometric and enrichment requirements of the FeCrAl bundles to meet an 18-month cycle length. 3D full-core models verifying the lattice physics results and an optimization of the assembly LP and CB patterns for both the FeCrAl and Zircaloy cores will be completed. Lastly, fuel performance of the FeCrAl cladding will be analyzed in order to determine whether the material can withstand the harsh core conditions similarly to that of Zircaloy.

VI.A. Preliminary BWR Lattice Physics Results

Preliminary depletion calculations were performed using a representative BWR lattice model of the 10 × 10 fuel assembly with a 40% void fraction (bottom half of the bundle). A base case lattice model was run in SCALE/TRITON with the cladding and channel box modeled as Zircaloy. Next, the cladding and channel box were replaced with candidate alternate materials (SiC and FeCrAl) and the neutronic penalty/advantage associated with each material was plotted as a function of EFPD in Figure 36. The gadolinium concentration in the gadolinia (Gd_2O_3)-containing pins found in the lattice is shown on the right ordinate.

Much as in the PWR analysis [17], FeCrAl produced a heavy neutronic penalty compared with Zircaloy due to increased neutron absorption. In fact, the penalty was greater than that recorded in the PWR pin cell calculations owing to the addition of the FeCrAl channel box. A slight increase in reactivity was found when all Zircaloy was replaced with the SiC/SiC composite, which matched PWR results.

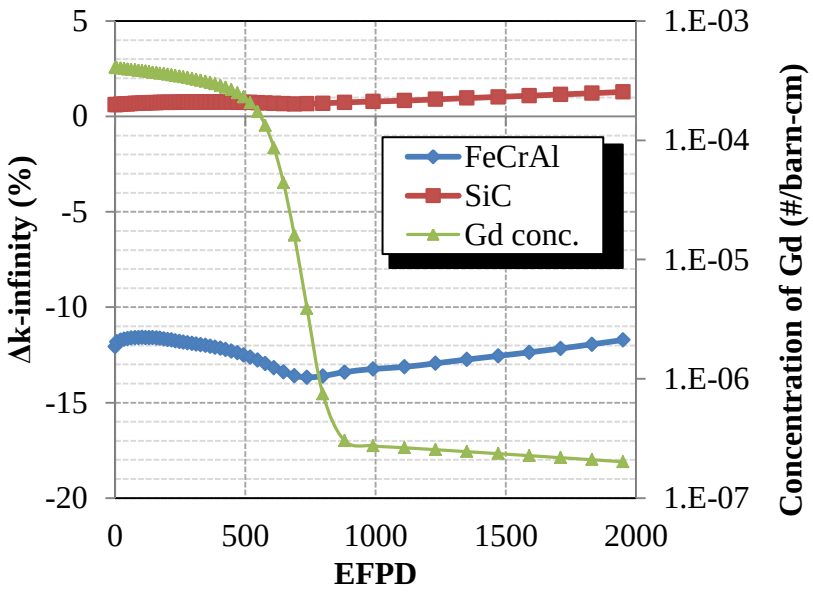


Figure 36: Δk-infinity from Zircaloy-4 cladding and channel box for FeCrAl and SiC

Used to suppress reactivity early in life, the gadolinia pins burn out at about 15 GWd/MTU, thus causing the downward slope in the FeCrAl curve to end at approximately 700 EFPD. The gadolinia pins minimize the early penalty of FeCrAl because thermal neutron absorption in gadolinia remains roughly constant regardless of the cladding material used. After the gadolinia burns out, a more profound effect on the neutron inventory surfaces for FeCrAl.

A brief analysis was done comparing the reactivity penalty of the channel box versus the cladding. Focusing on FeCrAl as the alternate cladding material, Figure 37 shows Δk-infinity (%) for three cases to understand the relative contributions of cladding and channel box to the combined reactivity penalty: 1) FeCrAl channel box and Zircaloy cladding, 2) FeCrAl cladding and Zircaloy channel box, and 3) FeCrAl cladding and channel box.

As shown in Figure 37, the summation of the Δk penalty from the channel box and cladding as individual elements is equivalent to the penalty of both elements consisting of FeCrAl. In addition, the reactivity penalty when replacing just the channel box is larger within the first 15 GWd/MTU when gadolinium is burning out. This is intuitive to the previous analysis in that the

penalty from FeCrAl is minimized in the presence of a higher absorbing material, especially when in closer proximity to the fuel regions, as is the cladding. Thus the penalty is not affected by gadolinium to the same degree when only the channel box is replaced with FeCrAl.

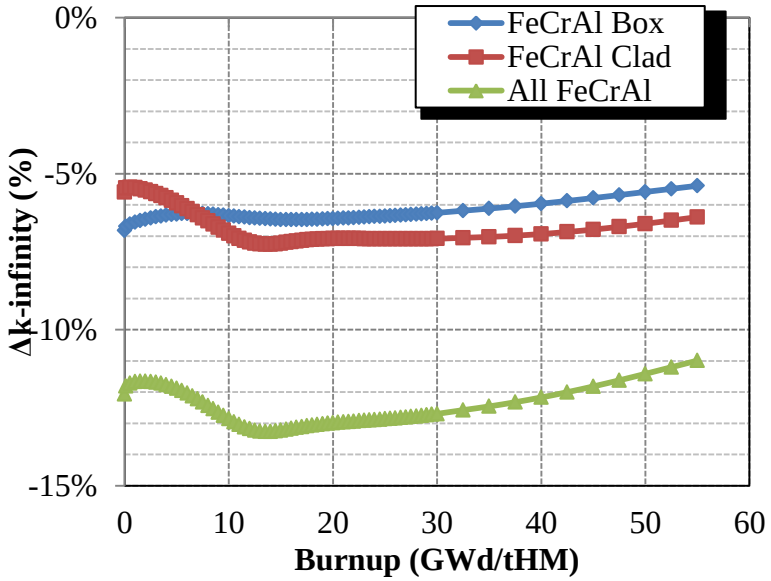


Figure 37: FeCrAl reactivity penalty of individual fuel elements

In the PWR study, the spectral hardening effect from the austenitic and ferritic materials played a major role in plutonium production near EOL. In Figure 37, the reduction in the Δk penalty as the depletion sequence nears EOL is evidence of this for BWRs as well. The addition of the channel box leads to an even harder neutron spectrum. Figure 38 plots the normalized neutron flux per unit lethargy as a function of neutron energy for the Zircaloy base case and the FeCrAl-loaded models.

The following data was taken from a CASMO simulation containing a 40-group energy structure. Because this fidelity is not as high as the PWR results containing 238 groups, the plot is slightly coarser. However the hardening of the neutron spectrum is clearly shown with the Zircaloy thermal spectrum peak significantly higher than that of the FeCrAl model. This spectral

shift leading to the production of plutonium is evident with Figure 37 displaying the reactivity penalty. As plutonium is bred more at EOL, the Δk-infinity penalty from FeCrAl is slightly minimized.

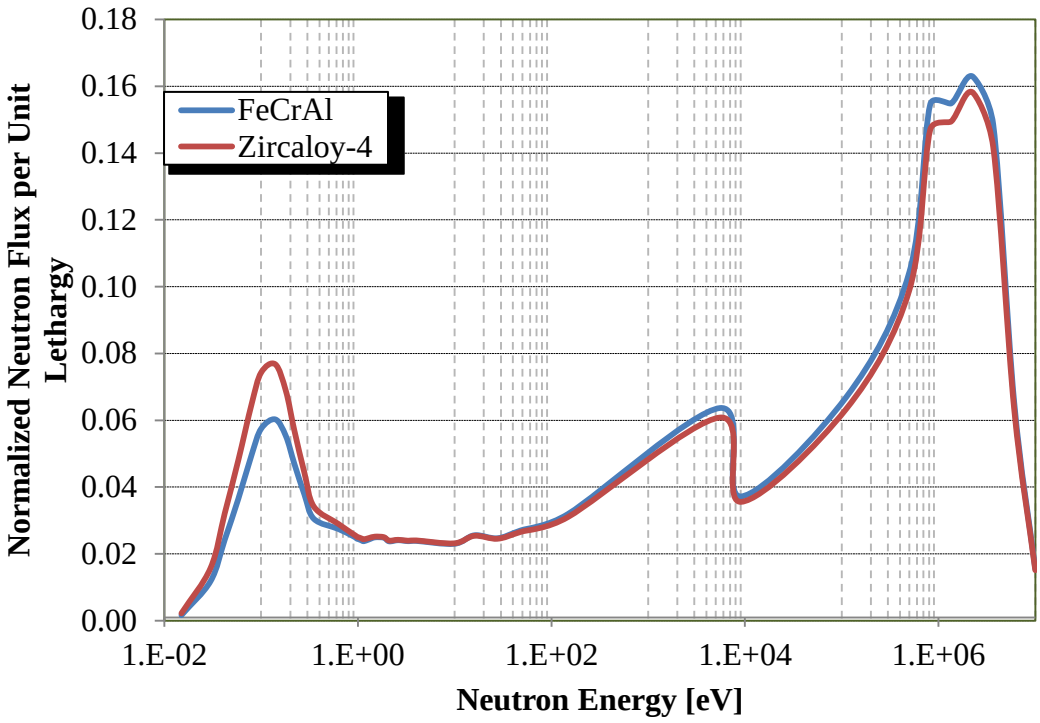


Figure 38: Neutron flux spectrum as a function of energy

VI.B. Two-Dimensional Parametric Study

As shown in Figure 36, reactivity lifetime requirements are exceeded when replacing the Zircaloy cladding and channel box with SiC. This is due to the low thermal absorption properties exhibited in the material. Therefore, the subsequent parametric study focused on meeting FeCrAl material in BWR assembly. In order to attempt to meet cycle length requirements of standard

Zircaloy bundles, ^{235}U enrichment and the pellet diameter were increased while the thickness of the FeCrAl cladding/channel box was decreased.

After a perturbation was made to the FeCrAl bundle design, the model was re-run in CASMO to determine a k-infinity value at the desired EFPD. Using the methodology in section IV.B. and equation 4.1, a new $\overline{\Delta k}_{bwr}$ could then be calculated. As aforementioned in the methodology section, a $\overline{\Delta k}_{bwr}$ value equal to or above 0.000 would be expected to meet lifetime requirements of the base case Zircaloy bundle.

Initially, the three lattices used in the model (PSZ, DOM and VAN) zones were run with the standard average weighted enrichment of 4.11% and a thinner cladding and channel box. The top plot on Figure 39 shows a larger $\overline{\Delta k}_{bwr}$ is calculated the thinner the cladding is. It should be noted that the channel box was thinned in proportion to the thinning of the cladding. The base case cladding and channel box thicknesses are 600 μm and 1600 μm, respectively. Therefore when a reduction of 75% cladding thickness was simulated (150 μm), the channel box was subsequently thinned to 400 μm. Alternatively, the bottom plot of Figure 39 displays the effect on $\overline{\Delta k}_{bwr}$ when the channel box and cladding thickness is kept constant and the ^{235}U enrichment is increased.

As shown in Figure 39, in order to meet BWR cycle length requirements of the Zircaloy base case at 4.11% U-235, a FeCrAl bundle would require a cladding thickness of 172 μm and a channel box thickness of 460 μm. Otherwise, an average enrichment of 6.46% U-235 would be required in each bundle if the cladding and channel box thickness were untouched. From an economic, fuel performance and regulatory standpoint, it is clear that these design modifications would not be acceptable for commercialization. Therefore, numerous additional cases were run perturbing the fuel enrichment and clad/channel box thickness simultaneously. All design BWR combinations equating to a $\overline{\Delta k}_{bwr}$ value of 0.000 (+/- 0.001) were plotted in Figure 40 so that the minimum design parameters necessary to meet cycle length requirements would be presented.

Similar to Figure 31 in the PWR analysis, a linear trend is shown in Figure 40 with respect to the enrichment and geometric perturbations required of the FeCrAl design. The method states that a FeCrAl bundle with the cladding and channel box cut in half to 300 μm, an average enrichment

level of approximately 4.72% ^{235}U would be required. A cladding thickness at this level was deemed as a conservative lower bound, since history austenitic alloy cladding that was previously commercialized had been manufactured with a similar thickness [22].

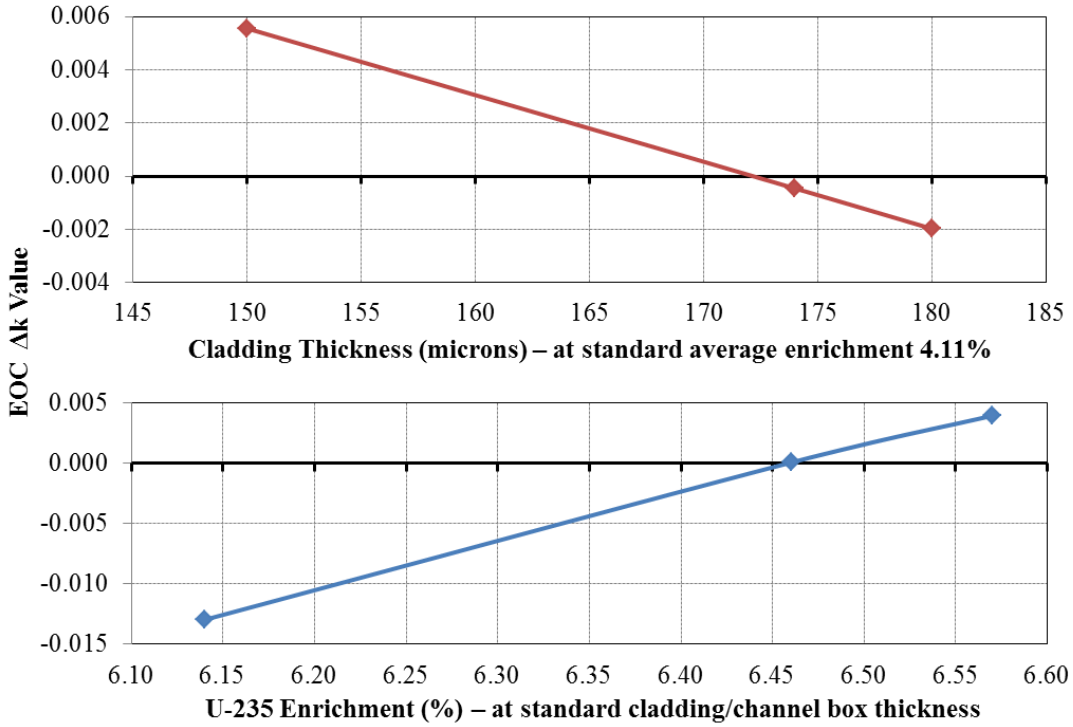


Figure 39: EOC Reactivity Values with respect to Fuel Design Changes in FeCrAl Loaded Bundles

It should be noted that although this case is below the low-enriched uranium (LEU) level, this is simply and weight average of all of the pins in the array. An enrichment of 4.72% throughout the DOM region lattice would contain fuel pins as high as 5.64% near the water holes and as low as 2.3% ^{235}U at the corners. Considering the advantages alternate cladding material exhibit, this may be a secondary concern if commercialized. Regardless, with some manipulation, the enrichment of the corner pins can be raised to reduce the burden of the hotter pins located closer to the center. Full-core models with pin power reconstruction would be needed in order to

determine whether manipulation of this fashion would severely compromise the limiting FΔh pins.

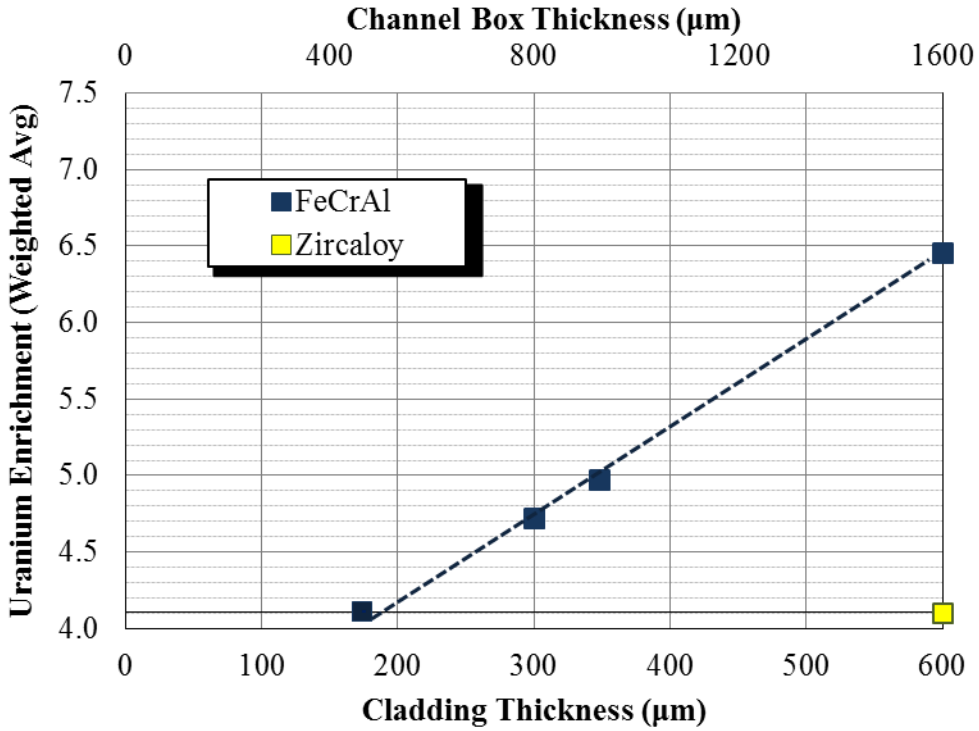


Figure 40: Fuel parameters required to match the BWR lifetime

VI.C. Full-core BWR Models

In order to develop and optimize a full-core model with FeCrAl bundles, a Zircaloy model was first established. A mid-size core (~2000 MW) that could maintain criticality for an 18-month cycle was selected as a representative base case. Therefore, the NESTLE full-core model was depleted for an 18-month cycle. The curve in Figure 41 was plotted with the CBs completely withdrawn (uncontrolled) so that the cycle length could be estimated once k-effective reached

unity. Note that for this calculation an eigenvalue bias associated with NESTLE is not being assumed, but the same approach is used for Zircaloy and FeCrAl, both, for consistency.

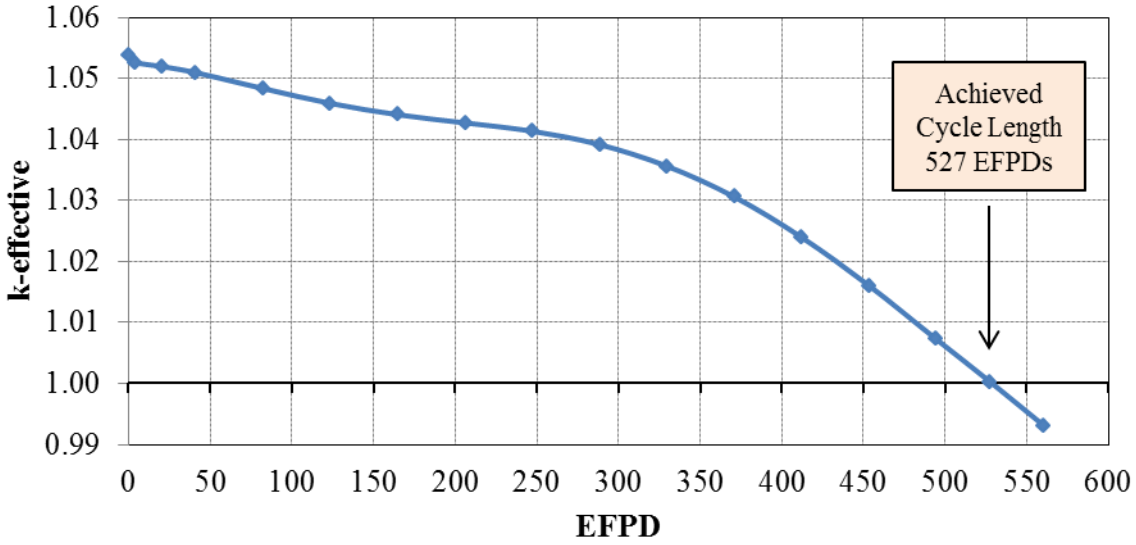


Figure 41: Full-core Zircaloy base case depletion

The depletion shown in Figure 41 indicates that the Zircaloy full-core base case model maintains criticality for a burnup of 12.8 GWd/MTU or 527 EFPD. As gadolinium burns out around 280 EFPD, the k-effective curve continues to deplete with a steeper slope and increasingly linear trend toward EOC. The following table describes the depletion results and design specifications from the NESTLE neutronics model.

For the FeCrAl loaded design to meet reactivity lifetime requirements on a full-core level, its cycle must reach or exceed that of the base case. As stated in the previous section, the EOC reactivity method provided multiple design combination of lattice enrichment and channel box/cladding thickness. From the four FeCrAl cases in Figure 40 that met lifetime requirement, only two geometric designs were carried through to the full-core analysis: Case 1) 300 μm cladding and 800 μm channel box, and Case 2) 600 μm cladding and 1600 μm channel box. Case 1) was chosen as the lower limit for thinning the cladding thickness and Case 2) was chosen

because its geometric specifications are equivalent to the Zircaloy model. The EOC reactivity method concluded that the bundles needed lattice enrichments of 4.72% and 6.35% U-235, respectively. However it is not a certainty that these exact design specifications will hold up when modeling an entire core.

Table XVI. Full-core BWR Specifications for Zircaloy Base Case

Parameter	Value	Units
Quarter Core Fuel Assemblies	111	#
Axial Fuel Nodes	24	#
Assembly Pin Configuration	10 × 10	#
Core Power	1910	MWt
Power Density	55.66	MW/L
Achieved Cycle Length	527.5	EFPD
Heavy Metal Loading	78.72	MTU
Burnup	12800	MWd/MTU

Using Cases 1 and 2, a full-core parametric study was performed in NESTLE. For each change in enrichment, lattice physics calculations were re-run in order to update the cross-section data fed into the full-core model. The full-core FeCrAl models were run for exactly 527 EFPDs to match that of the Zircaloy base case depletion sequence. The cladding thickness in Case 2 has the same pellet radius as the Zircaloy base case and thus the same heavy metal density. Therefore Case 2 was depleted for 12.80 GWd/MTU. However Case 1, containing a thinner cladding, larger fuel pellet and thus a larger heavy metal loading (91.72 MTU) was only depleted to 10.98 GWd/MTU. Starting with the U-235 settings from the EOC Reactivity Method results, enrichment was updated until the EOC k-effective values for Case 1 and 2 were equal to 1.000 (+/- 0.001). Figure 42 plots k-effective of the full-core FeCrAl models that met cycle length requirements to the Zircaloy model.

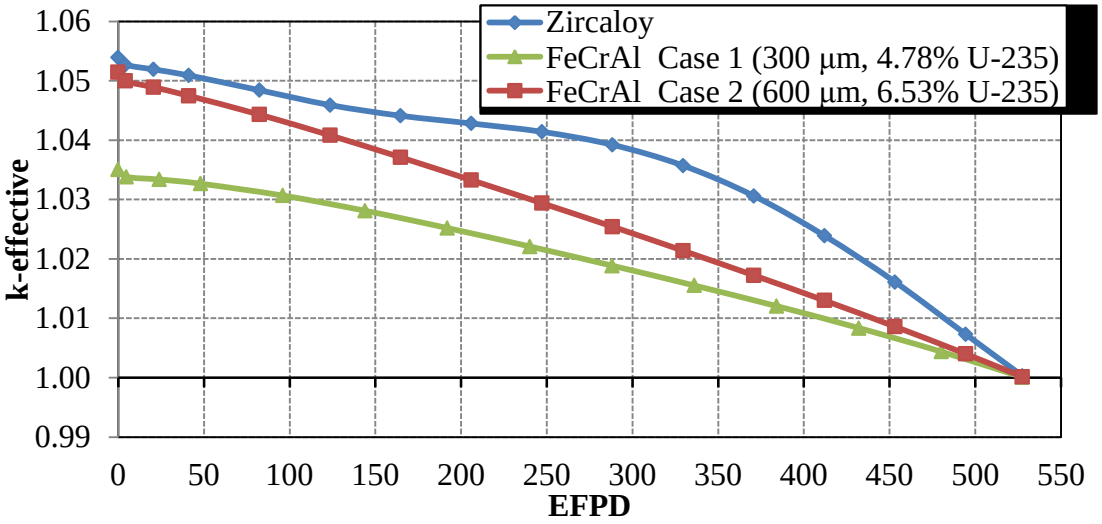


Figure 42: FeCrAl loaded core designs matching Zircaloy base case cycle length

The varying shapes shown in Figure 42 differ with respect to how each design responds to the neutron environment and the gadolinia present in the design. Case 1 (in green) maintains the flattest k-effective curve throughout the depletion cycle. This is because its heavy metal density is higher, and thus its burnup distribution is lower across the core. It is expected that Case 1 will produce lower peaking factors when optimization of the quarter core is done in a proceeding study. It is also evident that the Zircaloy base case is affected the most by the presence of the G_2O_3 rods. Since the enrichment in Case 2 is very high, the gadolinium in the system must compete for thermal absorptions with more U-235 atoms than the Zircaloy model. Similarly, there exists a small dip in the beginning of the Case 1 k-effective curve. Since it contains a marginally higher enrichment, gadolinium produces a slightly larger effect on its reactivity than that of Case 2. Lastly, the reactivity of the Zircaloy design drops much faster near EOC than both FeCrAl cases. This is due to the additional plutonium present in FeCrAl designs. Since the absorption properties of FeCrAl are much higher than Zircaloy, the neutron spectrum in the system is harder and thus is the conversion rate of plutonium.

Shown in the legend, the full-core FeCrAl design with 300 µm thick cladding would require an average lattice enrichment of 4.78% U-235. Likewise, an enrichment of 6.53% would be needed for a design with standard cladding thickness (600 µm). Plotting these combinations on the same

plot as the EOC Reactivity results produced Figure 43. Once again, all of the data points, whether 2D lattice physics or full-core models are expected to meet cycle length requirements.

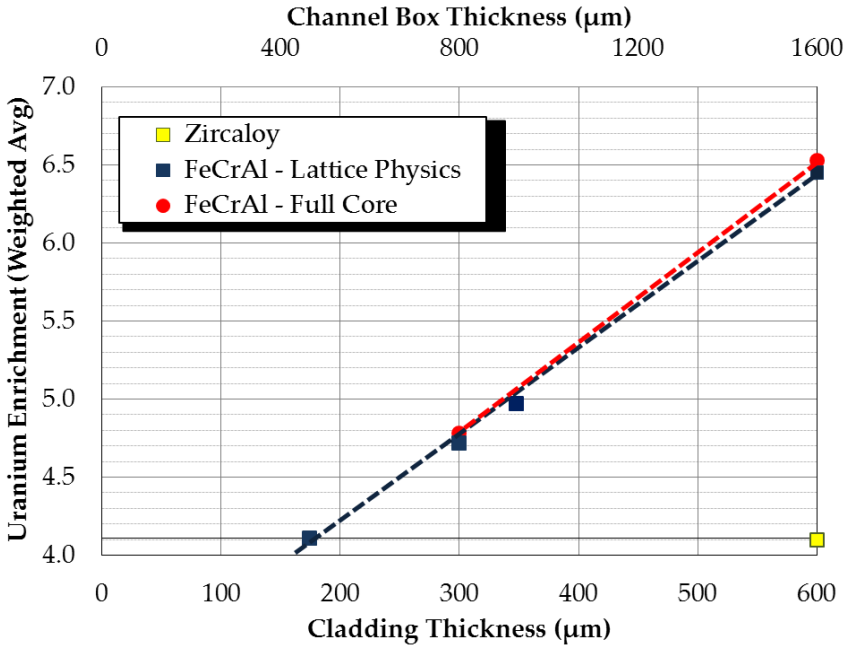


Figure 43: Parametric evaluation of lattice physics and full-core models

As shown in the Figure 43, the parametric analyses performed with the full-core models agree quite well with the lattice physics results. Design combinations of Case 1 with 300 µm thick FeCrAl cladding required almost identical fuel enrichments, while only slightly more fissile material was needed in Case 2 containing 600 µm thick cladding. Aside from a slight bias, Figure 43 strongly verifies the use of the EOC Reactivity Method as a useful approach for parametric studies to estimate cycle length impact in BWR cores as the one herein presented, by employing 2D lattice physics calculations as described. It should be noted that this methodology does not replace the usefulness of full-core 3D nodal simulators for the establishment of many other design and operational core management parameters.

VI.D. Shuffle and Control Blade Optimization

Initially, the CB pattern of the Zircaloy base case model was optimized throughout the 18-month depletion cycle with LWROpt. It was assumed that the initial LP shown in Figure 20a was optimal, and thus a LP optimization was not performed. As described in the methodology section, four different CB blanks were swapped at each timestep. Figure 44 describes the CB locations and their level of insertion/withdrawal axially into the core. The value at each CB location represents the number of notches withdrawn from the core. Consistent with commercial operation, each CB notch is equivalent to 3 inches axially, and the CB is inserted in increments of 2 notches. Thus a value of 48 represents a CB that is fully withdrawn from the 144 inch core while a value of 0 represents full insertion. The optimization as overlaid with the color-coded burnup distribution. Blue cells denote fresh assemblies while the red cells represent assemblies that have been highly exposed in the core.

Figure 44 shows the CB patterns taken at each of the optimization time steps. The low withdrawal values near BOC indicate that the CB banks are inserted more to compensate for the high reactivity. Intuitively, as the fuel depletes more throughout the cycle, less reactivity is present in the system, and thus the majority of CBs are nearly fully withdrawn near EOC.

Since radial RPF was a major OF during the optimization, the following radial powers were outputted at BOC and EOC. The maximum radial RPF allowed was 1.60, which was not violated during the optimization. Higher RPF values are shown at BOC with a max RPF of 1.54 due to the hotter, more reactive fresh feed assemblies. Alternatively, at an exposure of 12800 MWd/MTU, the radial power profile across the core flattened as the hotter assemblies depleted, leading to a max RPF of 1.50.

At various time steps early on in the depletion sequence, the nodal RPF constraints shown in Table VII were violated. As discussed in section IV.D.1., axial linear heat rates were calculated in relation to the nodal RPFs produced in the full-core model. Despite the aforementioned constraint violations, a maximum linear heat rate of 43 kW/m was recorded at the hottest node and most limiting depletion step. This value was considered a reasonably conservative value for

analyzing fuel performance, and thus the minor violation was deemed acceptable for both Zircaloy and FeCrAl models.

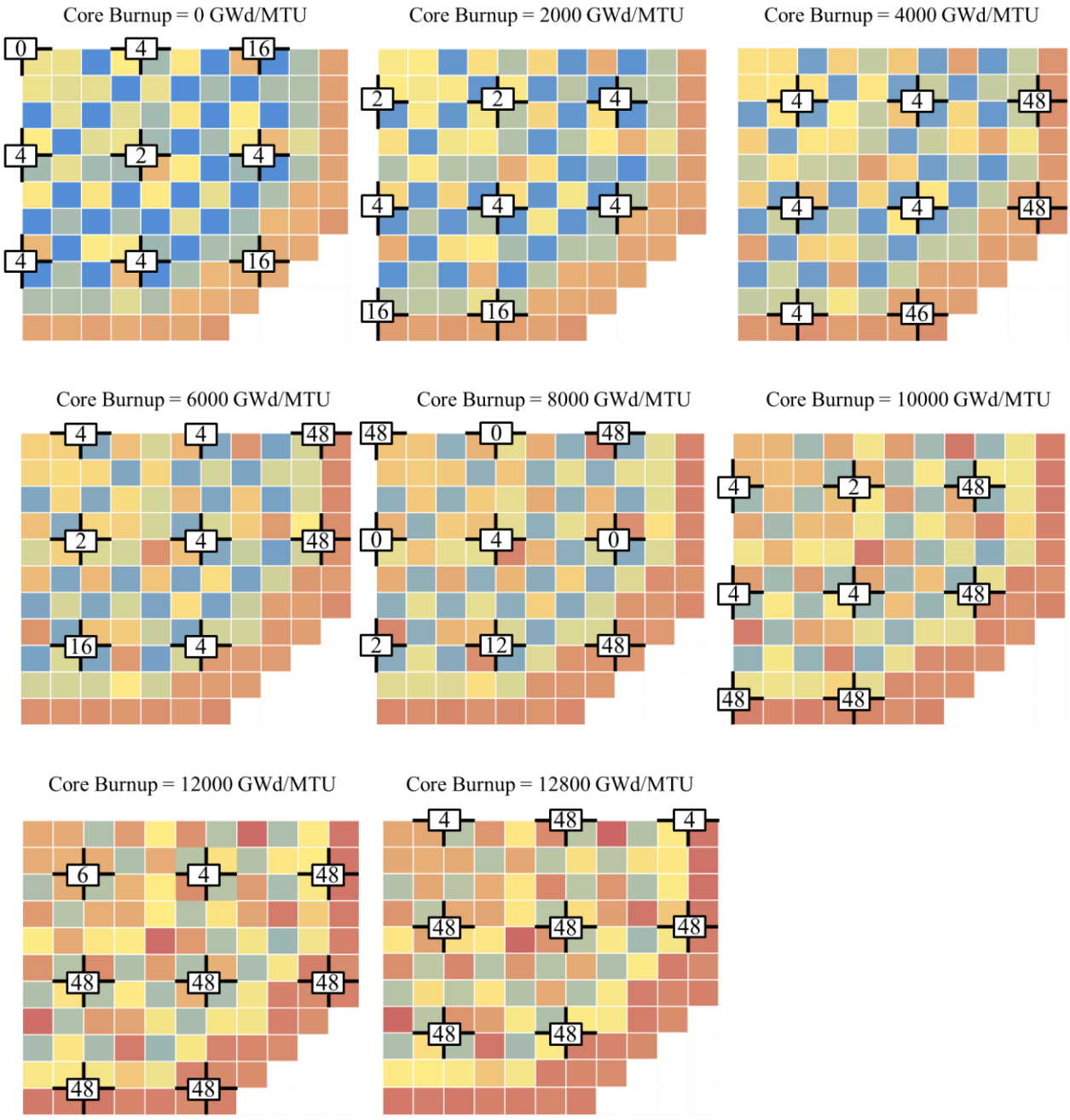


Figure 44: CB withdrawal in notches for Zircaloy base case core

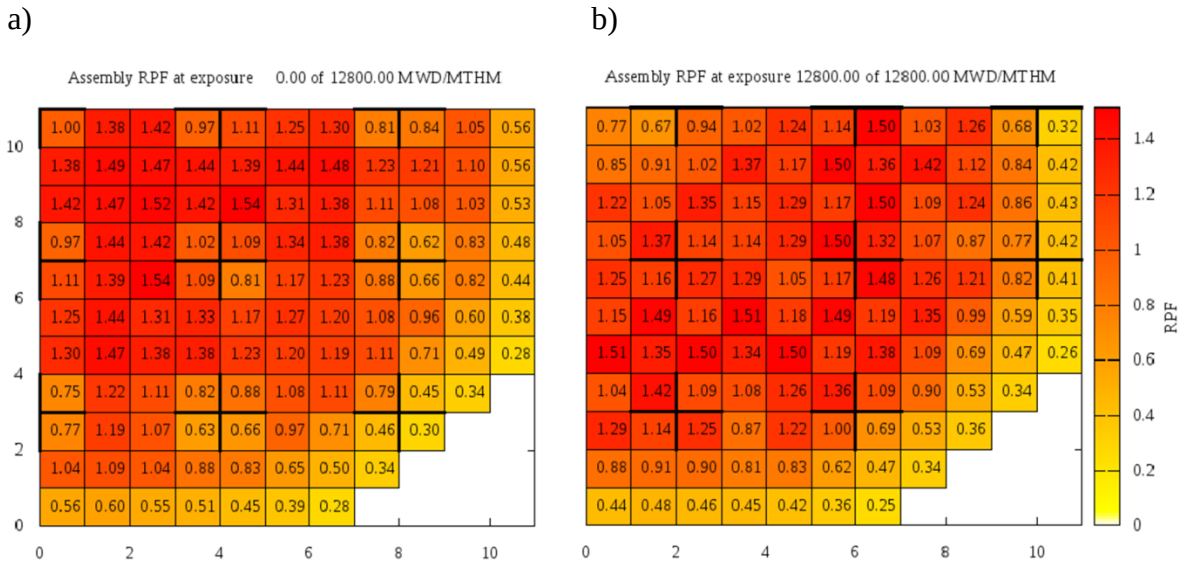


Figure 45: Relative power fraction of Zircaloy base case model at a) BOC b) EOC

Now that an optimized base case was established, loading and CB patterns for a FeCrAl-loaded BWR core could be determined for comparison purposes. Narrowing down the FeCrAl study, Case 1 was chosen for CB/LP optimization. The enrichment and cladding thickness for this case were 4.78% ^{235}U and 300 μm, respectively. This thickness level and enrichment combination was chosen by the ATF group as the most viable design for commercialization.

The LP shown in Figure 20a was ideal for Zircaloy base case but not necessarily best for FeCrAl. If the FeCrAl assemblies were shuffled radially, the cycle length of the full-core FeCrAl model could be increased. Thus a lower ^{235}U enrichment would be required than what was established in Figure 43. The shuffle pattern optimization was performed numerous times with varying RPF constraints. Figure 46 displays four of the LPs produced with radial RPFs ranging from 1.60 to 1.40. Cells labeled "-1" represent fresh feed assemblies, while the remaining assemblies are ranked in order of their exposures from lowest to highest burnup.

As shown in Figure 46, when a flatter radial power distribution across the core was requested, the EOC Δk-eff (cycle length) was reduced. Fresh assemblies lumped together near the center of the core will increase cycle length, but in turn invoke larger peaking relative to the surrounding

burnt assemblies. Although the RPF limits were maintained at EOC when using the Haling Depletion, power peaking was analyzed at each time step with a standard depletion after each LP was established. Considering all the aforementioned factors, it was determined that a LP in between Case 2 and Case 3 would be most suitable for the FeCrAl core. Thus a final optimization case was run with an EOC RPF limit of 1.47 to produce the LP in Figure 47a.

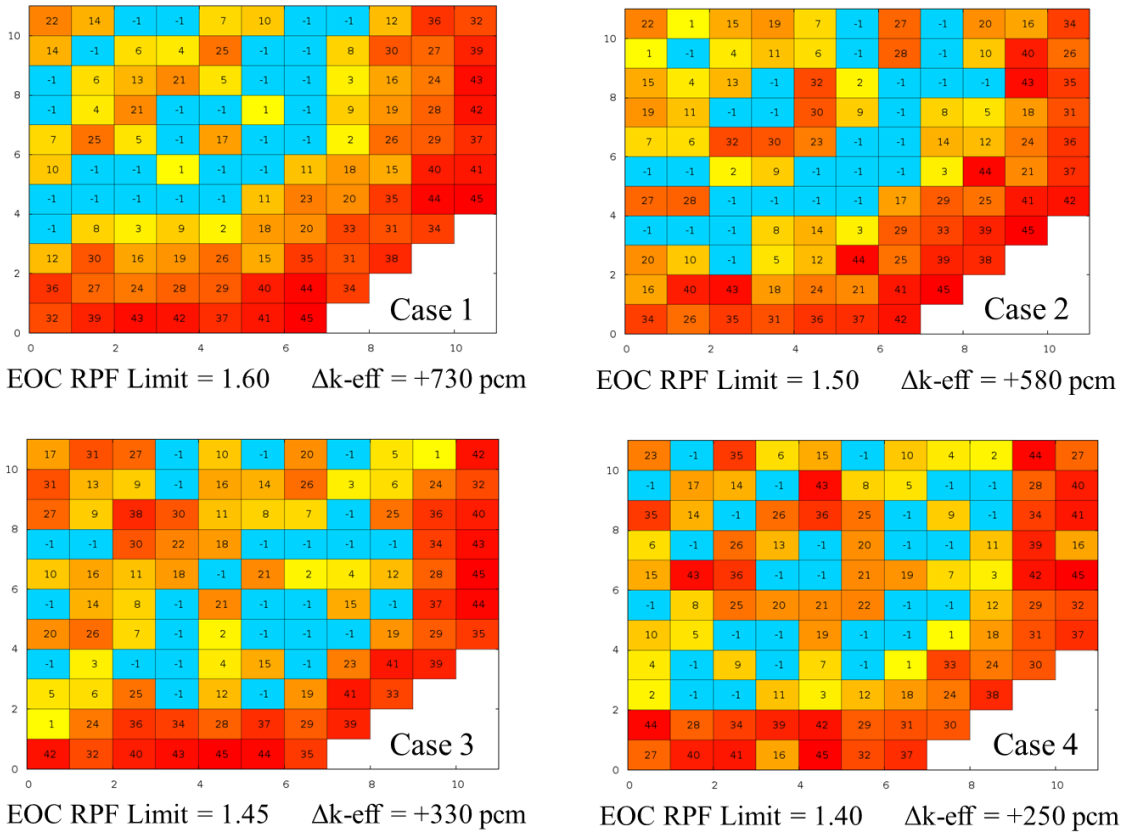


Figure 46: Loading pattern optimizations for FeCrAl core with varying RPF limits

Figure 47 also displays the CB locations that were optimized next. When considering core shutdown margins, clusters of 3 or more fresh feed assemblies around one CB, as shown in Figure 47a, would not be optimal from a commercial standpoint. Therefore, using the python GUI developed for fine-tuning of LPs, the clusters of fresh feed assemblies were dispersed. By

spreading apart one cluster at a time, the LPs were re-run in NESTLE to make sure a similar Δk-eff to that of Figure 47a was recorded at EOC. After numerous iterations, the LP shown in Figure 47b was established and used for the remainder of optimization analysis performed on the full-core FeCrAl design.

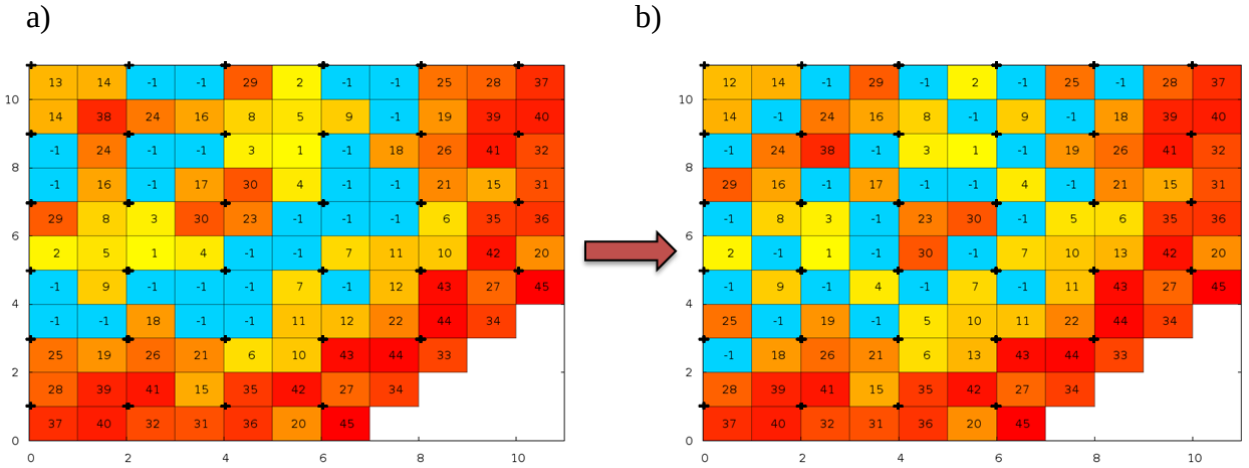


Figure 47: FeCrAl loading pattern with a) optimization code b) python GUI

Since excess reactivity was present at EOC after the LP optimization was complete, the overall enrichment in the FeCrAl bundles could be lowered even further. Therefore, after the LP in Figure 47b was established, the full-core parametric study could be re-done. First new cross-section data was obtained from CASMO, then NESLTE was re-run until the lowest enrichment was determined that could meet an EOC k-effective of 1.000. Thus, the average enrichment throughout the FeCrAl fuel bundle was reduced from 4.78 to 4.66% ^{235}U. With this enrichment and LP configuration, LWROpt was used once more to optimize the CB configuration of the FeCrAl model. The withdrawal of CB steps is indicated in Figure 48 for the entire depletion sequence.

Similar to the Zircaloy pattern shown in Figure 44, the CBs are fully withdrawn at the EOC. However when comparing the evolution of the burnup in Figure 44 and Figure 48, a major

difference in the initial placement of assemblies is evident. The base case Zircaloy LP configuration contains once burnt assemblies in light blue placed similar to that of a ring of fire. With this type of layout, radial RPFs for the Zircaloy were maintained just below 1.60. The configuration of once-burnt assemblies in the FeCrAl LP however is more centrally located. This allowed for a maximization of excess reactivity and increased cycle length. Despite the vastly different LP configuration, the design was still able to meet the same RPF limits as the base case due a flatter burnup distribution in due to its greater heavy metal loading.

Once the loading and CB patterns for the full-core FeCrAl model were optimized, the coolant properties through core were compared to the base case Zircaloy model. As described in the methodology section, thermal hydraulic specifications of both designs were made consistent in regards the fluid properties, hydraulic diameter, inlet temperature and mass flow rate. Therefore, the Zircaloy and FeCrAl models were expected to produce similar void profiles. Figure 49 plots the average void fraction of all the fuel bundles in the core at middle of cycle (MOC).

Void was plotted in Figure 49 with respect to the axial fuel nodes in the core. Node 4 represents the first fuel node moving up the core as the lower NAT zone. Consistent with standard BWR operation, the void fraction of the coolant starts near 0% (liquid phase) and peaks near the top of the core with nearing a 60% void. The plot shows that the fuel designs react similarly and no major anomalies were recorded. NESTLE does not incorporate mechanical properties of the cladding. Thus, future work must be done analyzing the different temperature distributions produced by each cladding material and how their varying thermal conductivities will affect the void distribution.

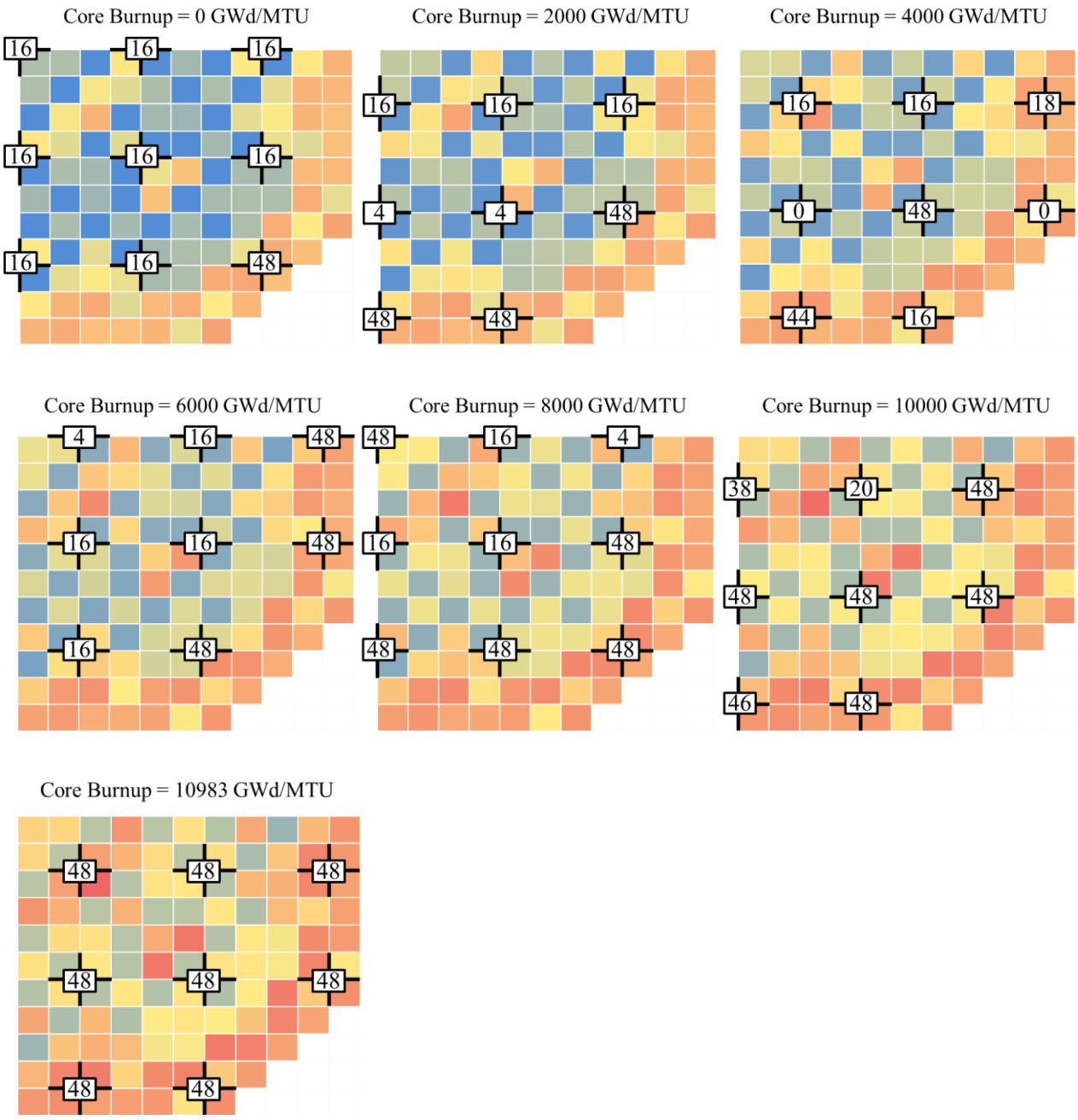


Figure 48: Control blade withdrawal in notches for FeCrAl core

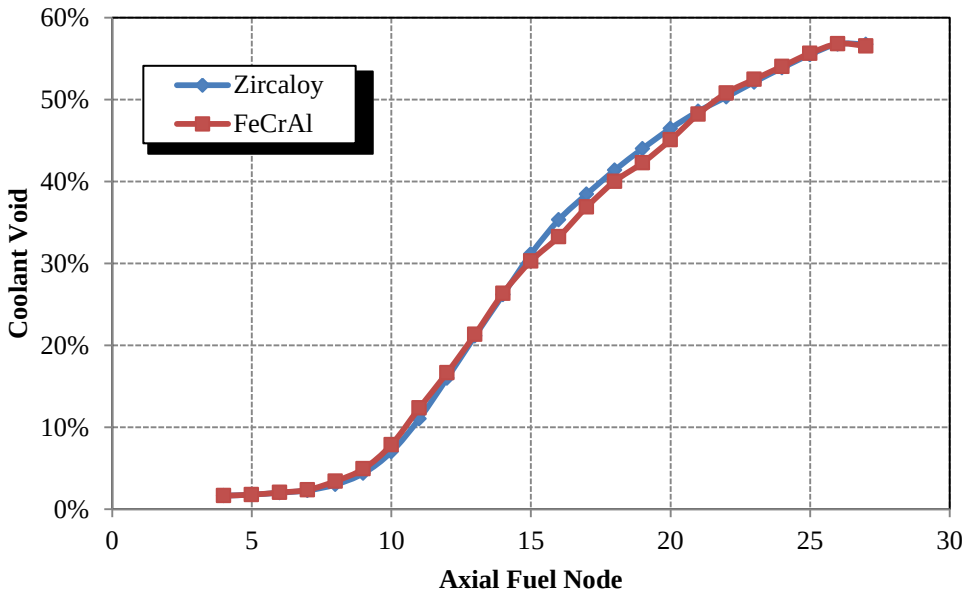


Figure 49: Bundle-averaged axial void distribution at MOC

VI.E. Hybrid SiC/FeCrAl Core

A side study was performed to investigate a hybrid ATF fuel bundle with FeCrAl cladding and a SiC channel box. To improve the waterside corrosion properties of the channel box, Ni and Cr were modeled as protective coated layers around the SiC, as shown in Figure 15. Due to parasitic neutron absorptions from FeCrAl, the thickness of the cladding was modeled at 300 μm to allow additional heavy metal loading.

Initially, the reactivity penalty from the Ni and Cr layers was quantified prior to setting up a parametric study. By quantifying each element's effect on the eigenvalue calculation, determining the appropriate enrichment requirements would be easier to pinpoint. Figure 50 displays lattice physics results from a 10 × 10 BWR fuel bundle modeled at 40% void with and without the Ni/Cr protective layers surrounding the channel box. CASMO4 was used to produce the following Δk-infinity penalty/advantage respect to EFPD. Although both models were depleted for 65 GWd/MTU, the hybrid bundles, containing a higher heavy metal loading, was depleted for a greater cycle length (EFPD). Therefore the k-infinity values from the hybrid

models were interpolated in order to match the EFPD of the Zircaloy base case prior to calculating the overall Δk penalty.

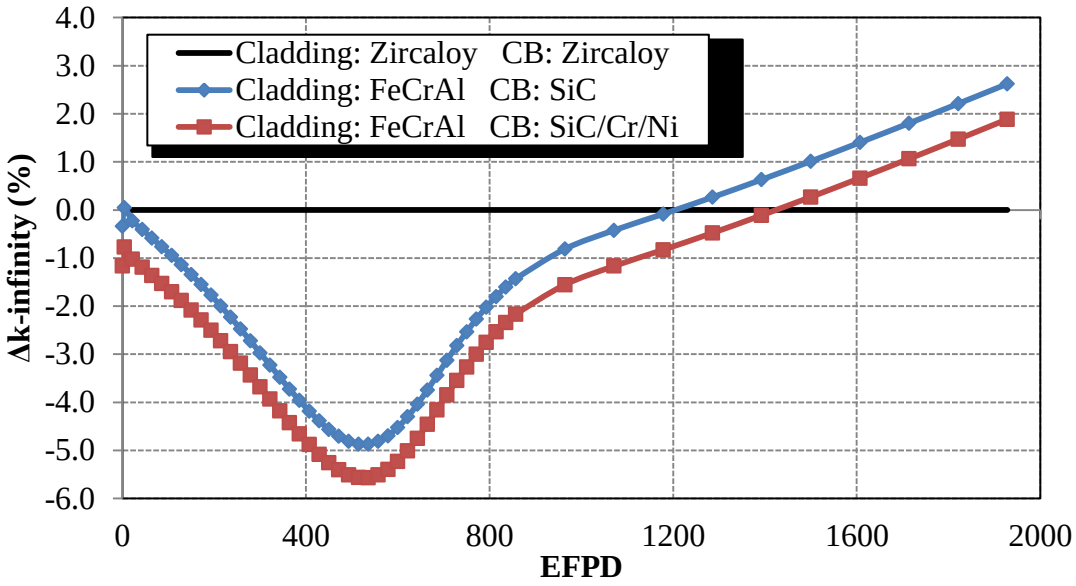


Figure 50: Δk-infinity from Zircaloy-4 cladding and channel box for hybrid bundles

Figure 50 indicates a large reactivity penalty early in life when modeling the hybrid bundle design with and without the Cr/Ni layers. Similar to Figure 36, the neutronic penalty of the FeCrAl cladding is greatly reduced in the presence of gadolinium. It does however delay the depletion of gadolinium, invoking a discontinuity at approximately 900 EFPD. Due to additional Pu bred from the harder neutron spectrum, the Δk penalty turns into an advantage near EOL.

In simulating the Cr and Ni protective layers, a 600-800 pcm Δk penalty is present due to additional parasitic neutron absorption. Despite this large penalty, manipulation of the fuel design to meet cycle length requirements of the Zircaloy design was performed. Therefore, the EOC reactivity method was utilized first to calculate the required enrichment equating to a 0.000 $\overline{\Delta k}_{bwr}$ value. Next, after cross-section data for each of the five axial slices in the bundle was obtained, a full-core calculation was performed with NESTLE. Enrichment was thus changed

until an EOC k-effective value of 1.00 was calculated. Lastly, the same was done using the LP optimized in Figure 47b for the FeCral channel box and cladded core.

Table XVII: Enrichment Requirements for Hybrid BWR Design

Method	Required Bundle Enrichment
EOC Lattice Physics	4.15%
Full-core depletion	4.13%
Shuffle Optimization	3.98%

Table XVII is consistent with the previous parametric study concluded with the results in Figure 43. The EOC reactivity method produced enrichment requirements nearly identical to what was needed in the full-core analysis. Also using an optimized LP for FeCrAl cladding, additional reactivity was found, thus reducing the enrichment requirements in the fuel bundles.

VI.F. Fuel Performance Results

VI.F.1. Fuel Rod Power History Calculations

As aforementioned in the methodology section, the hottest burning pin cell within the hottest burning assembly was chosen from the CASMO and NESTLE depletion results as the limiting fuel rod in the fuel performance model. By determining this, the linear heat rate of the hottest pin was calculated throughout the entire lifetime of the fuel. Since the full-core model was an equilibrium core, and multiple cycles were not performed, the fuel assembly with the highest radial RPF was chosen and followed for two additional cycles. This approximation was under the assumption that the equilibrium core will operate with similar exposure values for three straight cycles. Therefore, the following three assemblies were used to determine the limiting fuel rod in the reactor.

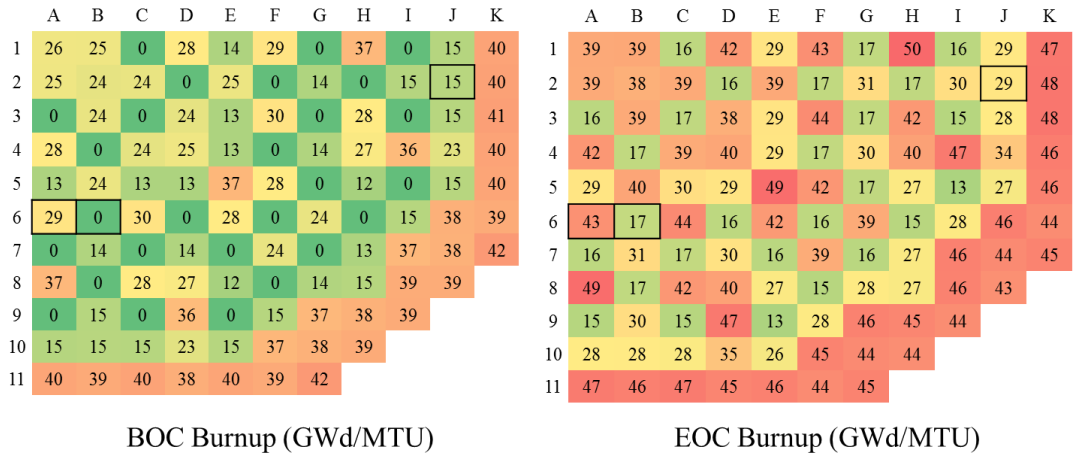


Figure 51: Equilibrium core exposure values for Zircaloy base case model

The fresh feed assembly in cell B6 contained the hottest RPF throughout the 12.8 GWd/MTU depletion cycle. Since the EOC burnup for that assembly was 17 GWd/MTU, it was assumed that it would move to cell J2 the following cycle. As the EOC burnup for assembly J2 was 29 GWd/MTU, the bundle was assumed to move to location A6. Therefore, the RPF values for these assemblies were gathered at each axial node in the reactor from birth to an exposure of 43 GWd/MTU. Transitioning to the lattice physics results, Figure 52 displays the 10 × 10 array of fuel pins at BOL with their respective relative peaking factors.

The hottest burning pin from the 10 × 10 array produced a RPF of 1.48 in relation to 92 pins in the lattice. As the array is symmetric across the diagonal center, only the bottom half was outputted. By fitting the RPFs to the hottest burning pin cell throughout the lattice physics depletion output, the hottest fuel rod was determined. Back-calculating the power of each node according to the 1910 MW core, the linear heat rate for the entire lifetime of the limiting pin was determined and exported into BISON-CASL. This method was done for case 1 and case 2 of the FeCrAl core designs as well. Each of the RPFs throughout the CASMO depletion was interpolated to match the burnup values of the full-core depletion sequence. Figure 53 displays the linear heat rates as a function of axial height. Although LHRs were recorded for at every time step, the figure tracks the power history of assembly B6 at BOL, MOL and EOL.

1.23									
1.33	1.45								
1.39	1.08	0.40							
1.48	1.14	0.73	0.45						
1.43	0.95	0.40	0.96	1.04					
1.43	0.99	1.06			1.02				
1.37	1.21	0.99			0.86	0.70			
1.36	1.07	0.43	0.90	0.39	0.70	0.37	0.62		
1.26	1.36	1.01	1.05	0.84	0.39	0.80	0.37	1.01	
1.13	1.20	1.32	1.26	1.15	1.09	1.10	1.09	1.18	0.91

Figure 52: CASMO BOL pin cell relative peaking factors

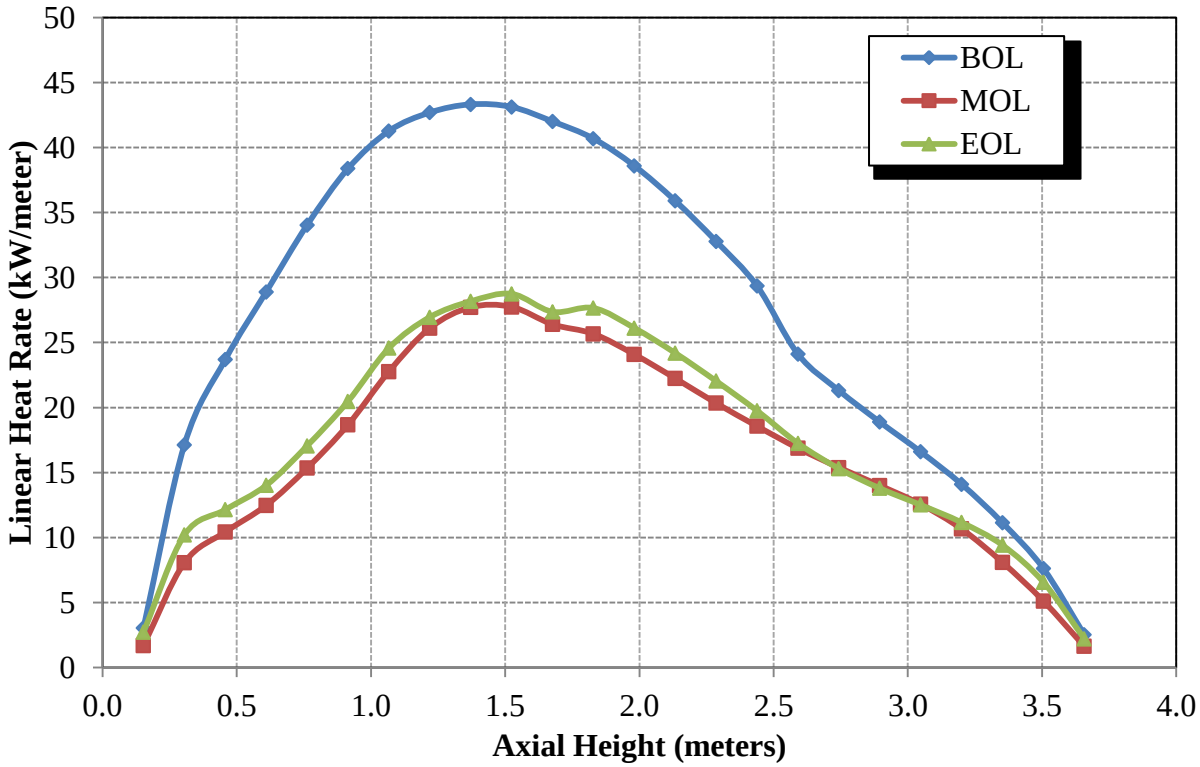


Figure 53: Axial linear heat rate for limiting Zircaloy assembly through first cycle

From BOL to EOL, the power shape of the fresh feed assembly plotted in Figure 53 flattens out to an average of approximately 20 kW/meter. Considering the extensive series of weighting factors taken from the full-core and lattice physics models, the calculated LHRs produced realistic axial power histories. Representing the peak location axially, the limiting rod at its hottest was 43.3 kW/m. The value was deemed sensible when simulating a conservative peak pin.

VI.F.2. BISON-CASL Results

Fuel performance results were performed by Ryan Sweet using the BISON-CASL software. Unfortunately, once contact of the fuel pellet and cladding began, the number of constraints applied to the BISON finite element mesh was increased, and subsequently, the solver performance degraded and the simulation slowed. Results presented herein are shown up to approximately 700 EFPD, which represents approximately half of the life of a standard fuel rod. Figure 54 plots the peak fuel centerline for FeCrAl with and without swelling. The FeCrAl cladding fuel rod with swelling has the highest temperature shown at the end of the depletion sequence. This should be expected over Zircaloy because the fuel radius of the FeCrAl models is larger and the thermal conductivity of UO_2 is low. The temperature of the FeCrAl cladding with swelling should also be larger than without swelling. This is because the cladding will slowly increase in size as it swells; opening the fuel-cladding gap and degrading the heat transfer from the fuel to the cladding [26].

In both cases (axial and radial, shown in Figure 55 and Figure 56), FeCrAl with swelling undergoes greater displacement than FeCrAl without swelling or Zircaloy. This is potentially because the thickness of the FeCrAl cladding is half that of the Zircaloy cladding, generating greater stresses on the cladding. The FeCrAl with swelling should also have greater displacements than the alloy without, simply because of the presence of isotropic volumetric swelling. Excessive clad swelling in the axial and radial directions can lead to fuel rod bowing as well as increased fretting wear. Therefore, future work will need to be done to analyze the mechanical implications from addition swelling and how it will affect reactor operation.

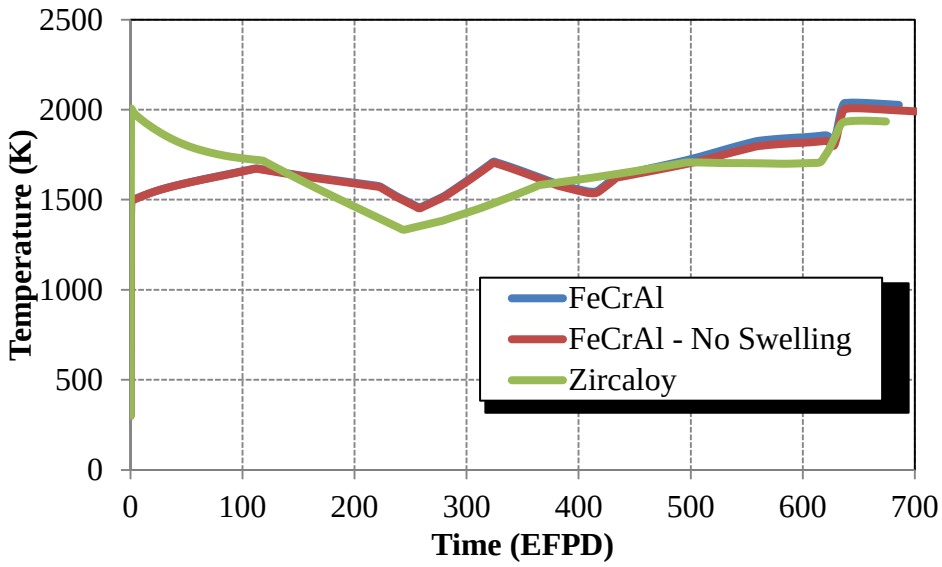


Figure 54: Peak centerline temperature

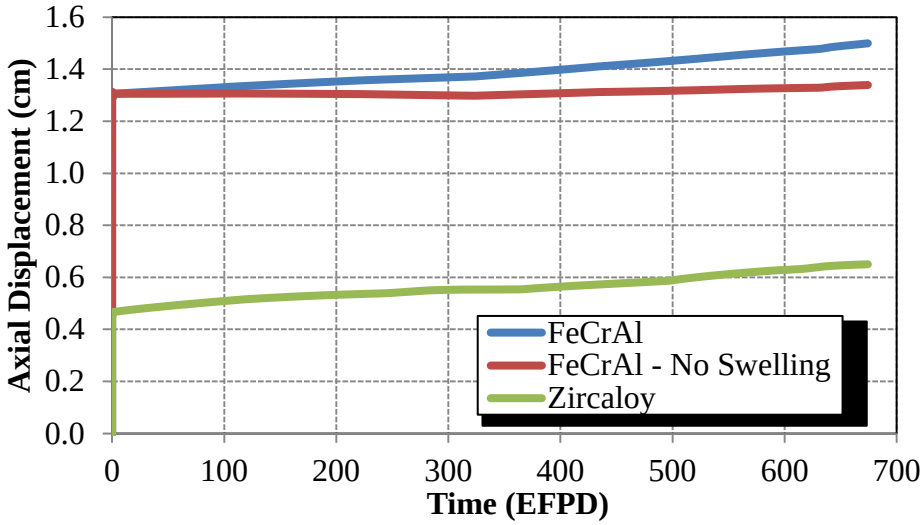


Figure 55: Axial displacement throughout depletion

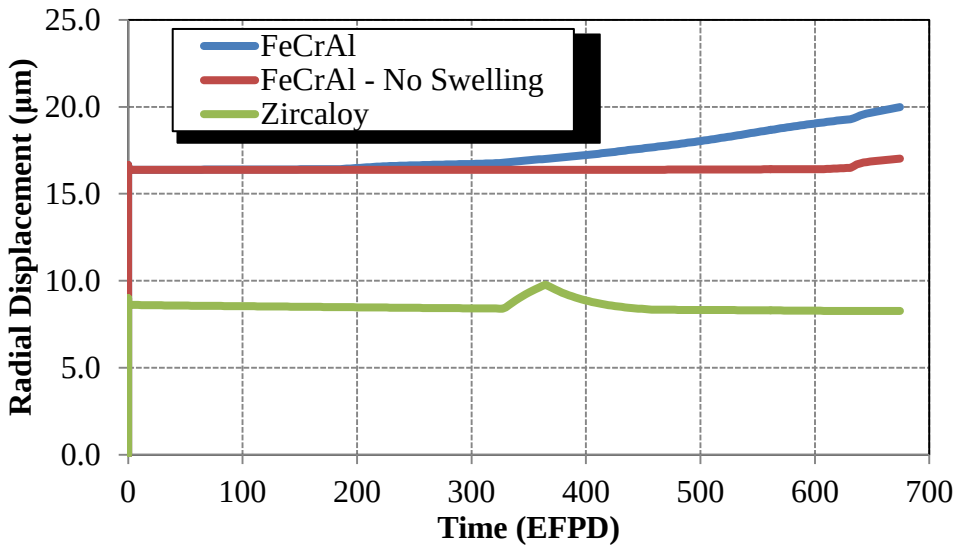


Figure 56: Radial displacement throughout depletion

Gap closure times were determined very roughly to be: 697 EFPD for FeCrAl, 700 EFPD for FeCrAl without swelling, and 278 EFPD for the Zircaloy cladding. This shows that the effect of swelling on gap closure is very small, but FeCrAl closes much later than Zircaloy due to its greater radial displacements. This is most likely an effect of the axial power profiles that are applied separately for each different type of cladding. As the FeCrAl model contained a higher heavy metal loading, the burnup distribution across the core is less than the Zircaloy core, leading to lower linear heat rates and smaller expansion of the UO_2 pellet. If the power peaks in a single area, the fuel in that area will expand faster in other areas leading to local gap closure in that area much sooner than the rest of the fuel rod [26].

VII. CONCLUSION AND FUTURE WORK

ATF designs including FCM fuel and enhanced alternate cladding concepts were analyzed in LWR systems. Some of these advanced concepts have the potential to severely reduce or entirely avoid accident outcomes similar to those of the Fukushima accident. Simulating a LWR environment, FCM fuel designs were modeled by varying the particle geometry, fuel composition, and material properties of the surrounding nuclear system while alternate cladding concepts were modeled by reducing the cladding thickness and increasing the UO_2 fuel enrichment. To determine a suitable design for use in a LWR, comparisons to a conventional LWR design were made for each ATF case.

During the FCM fuel study, uranium mononitride was chosen as an optimal uranium-based fuel for obtaining sufficient reactivity due to its increased fissile density. However, since the total fuel volume in the design is much less than that of a UO_2 pellet, manipulation of the particle and matrix was needed to obtain sufficient fissile material to sustain an 18-month operating cycle. Using the Equivalent Reactivity Method, it was determined that the amount of fissile material required for three 18-month cycles was 110% of a standard UO_2 pellet. Various particle geometry examples were shown that would supply sufficient volume to load this amount of fissile UN. Because the fuel contained 10% additional fissile material at BOL and underwent a large depletion by EOL, the flux spectrum was shown to soften significantly throughout its lifetime in comparison to conventional PWR fuel.

Creating a fresh-feed–once-burned checkerboard color-set, power sharing was analyzed for one 18-month cycle of the FCM fuel. For this non-optimized pin arrangement, the average peaking power levels across the FCM fresh and once-burned lattices at BOL were 1.134 and 0.866, respectively. This is only marginally less flat than standard UO_2 fuel at 1.109 and 0.891. When depleting the fuel to EOC, the FCM power sharing proved to be consistent with BOL.

The neutronic penalty associated with various alternate cladding materials was first quantified in comparison to zirconium alloy in a PWR system. UO_2 pin cell calculations were performed with Fe-based alloys, SiC and Zircaloy-4 cladding. The reactivity penalty in the reference PWR fuel

geometry was most noticeable with austenitic stainless steels because they contain nickel as an alloying element.

Utilizing the reactivity equivalence method, the overall reactivity difference between models during an 18-month PWR operating cycle was quantified. Various cases changing both enrichment and cladding thickness were analyzed, and the EOC values matching the standard PWR Zircaloy model were determined. To match lifetime requirements of standard UO_2 fuel, cladding thickness would need to be reduced by roughly half when holding enrichment constant. Alternately, an increase in enrichment of 1 to 1.5% would be required when using FeCrAl or 310SS with the reference cladding thickness. It should be noted that FeCrAl and 310SS requiring enrichment above 5 wt % ^{235}U would exceed the current licensed limit for fuel fabrication facilities. Because of its relatively low neutron absorption, SiC could meet lifetime requirements even with a 0.1% reduction in enrichment. Reactivity coefficients were calculated for each alternate cladding model. By perturbing the moderator temperature and density, MTC was found to be negative at BOL and over a range of fuel burnups, and it was of similar magnitude for all cladding types.

The neutronic penalty for a BWR was quantified for a transition from Zircaloy to FeCrAl for the fuel cladding and channel box. Two routes for increasing core reactivity over the fuel lifetime were examined; increasing the uranium enrichment and increasing the fuel pellet diameter while decreasing cladding thickness. A reduction in FeCrAl cladding and channel box thickness by roughly half with an average enrichment increase of approximately 0.6% resulted in an estimated cycle length matching that of reference BWR bundles with Zircaloy cladding. Historic use of iron-based cladding in commercial LWRs operated with similar cladding dimensions.

A full-core equilibrium BWR model was established with NESTLE in setting up a parametric study for the FeCrAl fuel bundles. Initial full-core BWR calculations in NESTLE verified the lattice physics results by meeting the 527-EFPD cycle length with nearly identical enrichment requirements. CB and LP optimization was performed on the FeCrAl core design which in turn increased reactivity while maintaining RPF limits. A hybrid fuel bundle was established with FeCrAl cladding and a SiC/Ni/Cr channel box. By halving the cladding thickness, the

enrichment level required was less than that of the Zircaloy base case design after performing LP optimization of the hybrid bundle core.

Fuel performance analysis of FeCrAl-cladded fuel rods was performed by Mr. Ryan Sweet, with the BISON-CASL code. By linking the linear heat rate results from NESTLE, the limiting fuel rods from the FeCrAl and Zircaloy cores were compared. Due to the lower power history profile in the FeCrAl model, the expansion of the UO_2 pellet was minimized and thus time to gap closure for FeCrAl occurred at 700 EFPD, whereas the closure for Zircaloy occurred at 278 EFPD. However, due to larger overall fuel pellet radius in the FeCrAl model, the overall thermal conductivity in the fuel rod was decreased leading to slightly higher centerline temperatures. The fuel performance calculations also showed an increase in radial and axial expansion for FeCrAl, which is herein reported and presented. Future studies will evaluate and assess operational limitations and impacts associated with the larger expansion tendencies for this material.

Future work has been proposed to optimize CB and LPs simultaneously with FeCrAl and hybrid bundle designs. Although the simultaneous optimization in LWROpt is more computationally expensive and time consuming, more realistic results are expected. Additional simulations are being performed in BISON with implementation of thermal and irradiation creep of FeCrAl. Results will be presented for the entire lifetime of each limiting fuel rod once PCI fidelity issues are resolves within the model.

REFERENCES

1. George, N.M., et al., *Neutronics studies of uranium-bearing fully ceramic microencapsulated fuel for pressurized water reactors.* Nuclear Technology, 2014. **188**(3): p. 2.
2. Azevedo, C., *Selection of fuel cladding material for nuclear fission reactors.* Engineering Failure Analysis, 2011. **18**(8): p. 1943-1962.
3. George, N.M., K.A. Terrani, and J.J. Powers, *Neutronic analysis of candidate accident-tolerant iron alloy cladding concepts*. 2013, Oak Ridge National Laboratory (ORNL).
4. Nicol, K. *America's First Civilian Nuclear Plant*. Penn State Libraries 2010.
5. Makhijani, A., *Nuclear fuel rod cladding material.* Institute for Energy and Environmental Research, 2011.
6. Koo, Y.-H., Y.-S. Yang, and K.-W. Song, *Radioactivity release from the Fukushima accident and its consequences: A review.* Progress in Nuclear Energy, 2014. **74**: p. 61-70.
7. McCurry, J. *Fukushima operator may have to dump contaminated water into Pacific*. 2014.
8. Venneri, F., et al., *Fully Ceramic Microencapsulated Fuels: A Transformational Technology for Present and Next Generation Reactors-Preliminary Analysis of FCM Fuel Reactor Operation.* Transactions of the American Nuclear Society, 2011. **104**.
9. Olander, D., *Nuclear fuels–Present and future.* Journal of Nuclear Materials, 2009. **389**(1): p. 1-22.
10. Powers, J.J. and B.D. Wirth, *A review of TRISO fuel performance models.* Journal of Nuclear Materials, 2010. **405**(1): p. 74-82.
11. Hanson, D., *A review of radionuclide release from HTGR cores during normal operation.* Electric Power Research Institute, Report, 2004. **1009382**.
12. Terrani, K.A., L.L. Snead, and J.C. Gehin, *Microencapsulated fuel technology for commercial light water and advanced reactor application.* Journal of Nuclear Materials, 2012. **427**(1): p. 209-224.
13. Was, G.S., *Fundamentals of radiation materials science*. 2007: Springer.
14. Snead, L.L., et al., *Handbook of SiC properties for fuel performance modeling.* Journal of Nuclear Materials, 2007. **371**(1): p. 329-377.
15. Minato, K., et al., *Improvements in quality of as-manufactured fuels for high-temperature gas-cooled reactors.* Journal of Nuclear Science and Technology, 1997. **34**(3): p. 325-333.
16. Hofmann, P., *Current knowledge on core degradation phenomena, a review.* Journal of nuclear materials, 1999. **270**(1): p. 194-211.
17. George, N.M., et al., *Neutronic analysis of candidate accident-tolerant cladding concepts in pressurized water reactors.* Annals of Nuclear Energy, 2015. **75**: p. 703-712.
18. Cathcart, J., et al., *Zirconium metal-water oxidation kinetics. IV. Reaction rate studies*. 1977, Oak Ridge National Lab., Tenn.(USA).
19. Pint, B.A., et al., *High temperature oxidation of fuel cladding candidate materials in steam–hydrogen environments.* Journal of Nuclear Materials, 2013. **440**(1): p. 420-427.
20. Terrani, K., S. Zinkle, and L. Snead, *Advanced oxidation-resistant iron-based alloys for LWR fuel cladding.* Journal of Nuclear Materials, 2014. **448**(1): p. 420-435.
21. Terrani, K.A., et al., *Silicon Carbide Oxidation in Steam up to 2 MPa.* Journal of the American Ceramic Society, 2014. **97**(8): p. 2331-2352.

22. Strasser, A., et al., *An Evaluation of Stainless Steel Cladding for Use in Current Design LWRs, NP-2642*. 1982, Electric Power Research Institute: Palo Alto, CA.
23. Ben-Belgacem, M., et al., *Thermo-mechanical analysis of LWR SiC/SiC composite cladding.* Journal of Nuclear Materials, 2014. **447**(1-3): p. 125-142.
24. Yueh, K. and K.A. Terrani, *Silicon carbide composite for light water reactor fuel assembly applications.* Journal of Nuclear Materials, 2014. **448**(1): p. 380-388.
25. Permann, C.J., *Multidimensional Multisale Fuels Modeling and Simulation*, in *Nuclear Fuels & Materials Spotlight*. Idaho National Laboratory.
26. George, N.M., et al., *Full-core Evaluation of Enhanced Alternate Cladding Concepts in BWRs (in review).* 2015.
27. Gaston, D., et al., *MOOSE: A parallel computational framework for coupled systems of nonlinear equations.* Nuclear Engineering and Design, 2009. **239**(10): p. 1768-1778.
28. Hales, J., et al., *Verification of the BISON fuel performance code.* Annals of Nuclear Energy, 2014. **71**: p. 81-90.
29. Williamson, R. and S. Novascone, *Application of the BISON Fuel Performance Code of the FUMEX-III Coordinated Research Project.* 2013.
30. Hales, J., et al., *BISON Theory Manual The Equations Behind Nuclear Fuel Analysis.* 2013.
31. Smith, K. and J. Rhodes, *CASMO-4 characteristics method for two-dimensional PWR and BWR core calculations.* Trans. Am. Nucl. Soc, 2000. **83**: p. 294.
32. Kucukboyaci, V.N., M. Ouisloumen, and F. Franceschini. *Two-dimensional whole core transport calculations using PARAGON*. in *Proc. Int. Conf. on Mathematics, Computational Methods & Reactor Physics (M&C 2009)*. 2009.
33. Driscoll, M.J., T.J. Downar, and E.E. Pilat, *The linear reactivity model for nuclear fuel management*. 1990: American Nuclear Society La Grange Park.
34. Downar, T., et al., *PARCS v2. 6 US NRC core neutronics simulator theory manual.* Purdue University/NRC, 2004.
35. Maldonado, G., et al., *Integration of the NESTLE Core Simulator with SCALE.* Transactions of the American Nuclear Society, 2009. **100**: p. 619-620.
36. DeHart, M.D. and S.M. Bowman, *Reactor physics methods and analysis capabilities in SCALE.* Nuclear Technology, 2011. **174**.
37. Bowman, S.M., *SCALE 6: comprehensive nuclear safety analysis code system.* Nuclear technology, 2011. **174**(2): p. 126-148.
38. Chadwick, M., et al., *ENDF/B-VII. 0: Next generation evaluated nuclear data library for nuclear science and technology.* Nuclear data sheets, 2006. **107**(12): p. 2931-3060.
39. Godfrey, A., *VERA Core Physics Benchmark Progression Problem Specifications*. 2013, Revision.
40. Kim, Y. and M. Baek, *Elimination of double-heterogeneity through a reactivity-equivalent physical transformation.* 2005.
41. Kanthal, A., *APMT Tube Material datasheet.* AB Sandvik group, Sandviken, Sweden.
42. *Fuel design data.* Nuclear Engineering International, 2004. **49, Sept.**(September): p. 26-35.
43. Bloore, D.A., *Reactor physics assessment of thick silicon carbide clad PWR fuels*. 2013, Massachusetts Institute of Technology.

44. Smith, H.J., *Analysis of Experimental Data for High Burnup BWR Spent Fuel Isotopic Validation - SVEA-96 and GE14 Assembly Designs.* ORNL/TM-2013/18, 2013.
45. Fensin, M.L., *Optimum Boiling Water Reactor Fuel Design Strategies to Enhance Reactor Shutdown by the Standby Liquid Control System*. 2004, M.S. Thesis, University of Florida.
46. Watford, G. *Advanced 10× 10 GE BWR fuel design*. in *Proceedings of ANS Topical Meeting on Advances in Fuel Management II, Myrtle Beach, South Carolina*. 1997.
47. Asgari, M., et al., *Application of the N-Streaming SM concept to Peach Bottom 2 Cycle 17.* 2006.
48. Larsen, N., *Core Design and Operating Data for Cycles 1 and 2 of Peach Bottom 2*. 1978, General Electric Co., San Jose, CA (USA). Nuclear Energy Engineering Div.
49. Turinsky, P.J., *Few-Group Neutron Diffusion Equation Solver Utilizing the Nodal Expansion Method for Eigenvalue, Adjoint, Fixed-Source Steady-State and Transient Problems.* Electric Power Research Center, North Carolina State University, Raleigh, NC, USA, 1994.
50. N.P. Luciano, e.a., *"The NESTLE 3D Nodal Core Simulator: Modern Reactor Models," accepted*, in *ANS MC2015 Joint International Conference on Mathematics and Computation (M&C)*. ANS: Nashville, TN, USA, April 2015.
51. Galloway, J., et al., *BWR modeling capability and Scale/Triton lattice-to-core integration of the Nestle nodal simulator-331*, in *Proc. of Physor*. 2010: Pittsburgh, PA.
52. Galloway, J.D., *Boiling Water Reactor Core Simulation with Generalized Isotopic Inventory Tracking for Actinide Management*. 2010, PhD Dissertation, University of Tennessee.
53. Ottinger, K.E., *Multi-cycle boiling water reactor fuel cycle optimization.* 2014.
54. Lemmon, E., et al., *NIST12 Thermodynamic and Transport Properties of Pure Fluids-NIST Standard Reference Database 23*. 2007, Version.
55. Luciano, N., *The Drift Flux Model as Implemented in NESTLE.* 2012.
56. Hunn, J.D. and R.A. Lowden, *Data compilation for AGR-1 baseline coated particle composite LEU01-46T*. 2006, Oak Ridge National Laboratory (United States).
57. Morris, R.N. and P. Pappano, *Estimation of maximum coated particle fuel compact packing fraction.* Journal of nuclear materials, 2007. **361**(1): p. 18-29.
58. Shapiro, R., I. Younker, and M. Fratoni, *Neutronic performance of accident tolerant fuels.* Trans. Am. Nucl. Soc, 2013. **109**: p. 1351-1353.

APPENDIX

Appendix A: Sample 10 × 10 BWR Lattice Physics SCALE Input

```
=t-depl parm=(centrm, addnux=2)
BWR GE 10 × 10-8, 2D full assembly model
xsLib
' ------------------------------------------------------------------
'  template to generate libraries for ORIGEN-S
'  parameters are: u235wt%      - wt% U235
'                  u234wt%      - wt% U234
'                  u236wt%      - wt% U236
'                  u238wt%      - wt% U238
'                  ddd          - coolant density (g/cc)
'                  dancoff1     - dancoff factor 1
'                  dancoff2     - dancoff factor 2
'                  namelibrary  - name of generated ORIGEN library
'                  specpow      - average specific power
'                  daystoburn   - depletion interval in days
'  options are:    name         - g10_
'                  enrichment   - 1.5, 2.0, 3.0, 4.0, 5.0, 6.0
'                  mod. density - 0.1, 0.3, 0.5, 0.7, 0.9
'                  dancoff1     - 0.5125, 0.4042, 0.3302, 0.2762,
'                                 0.2351
'                  dancoff2     - 0.3335, 0.2664, 0.2203, 0.1864,
'                                 0.1603
'                  spec. power  - 40.0
'                  burnups      - 0, 1.5, 3, 4.5, 6, 7.5, 9, 10.5,
'                                 12, 13.5, 15, 16.5, 18, 19.5,
'                                 21, 24, 27, 30, 33, 36, 39, 42,
'                                 45, 48, 51, 54, 57, 60, 63, 66,
'                                 69, 72
' ------------------------------------------------------------------
' Documentation and Notes (empty fields are auto-populated):
'  [Change Log]
'    Rev 0: Generated by J. Doe |
'    Rev 1: Generated by B. R. Betzler, June 2014
'  [Author(s)] B. R. Betzler
'  [SCALE Version] SCALE 6.2
'  [Reactor Type] Boiling Water Reactor General Electric 10 × 10-8
'  [Model Info] 2D t-depl full assembly model (see Figure \ref{fi:ge10 × 10-
8}), xsLib cross-section library
'  [Sources]
'    1. B. J. Ade, ``Generation of Collapsed Cross Sections for Hatch 1
Cycles 1-3 and Generation of Generic BWR Reflector Cross Sections'',
ORNL/LTR-2012/559, Oak Ridge National Laboratory, 2012. |
'    2. H. Smith, J. Peterson, and J. Hu, ``Fuel Assembly Modeling for the
Modeling and Simulation Toolset'', ORNL/LTR-2012-555 Rev. 1, Oak Ridge
National Laboratory, 2013.
'  [Data Range]
'  [Libraries]
'  [Power]
'  [Other Info]
'    Channel box data, fuel/gap/channel moderator densities, and temperatures
from Reference 1.
'    All other dimensions, materials, etc. from Reference 2.
'  figure{ge10 × 10-8.pdf: BWR GE 10 × 10-8.}
' ------------------------------------------------------------------
read alias
  $fuel 1 11 21 end
  $clad 2 12 22 32 end
  $mod  3 13 23 33 end
  $gap  4 14 24 34 end
```

```
  $fgad 311 312 313 314 315 316 317 end
end alias
'
' ------------------------------------------------------------------
read comp
'
' fuel
  uo2 $fuel den=10.42 1 948.45 92234 u234wt%
                               92235 u235wt%
                               92236 u236wt%
                               92238 u238wt% end
'
' fuel - with 5.0% Gd2O3
  gd2o3 $fgad den=10.24 0.05 948.45 end
  uo2   $fgad den=10.24 0.95 948.45 92234 u234wt%
                                    92235 u235wt%
                                    92236 u236wt%
                                    92238 u238wt% end
'
' clad
  zirc2 $clad 1 636.06 end
'
' moderator/coolant - water
  h2o   $mod den=ddd 1 560.29 end
'
' gap - helium
  he-4  $gap den=0.00011 1 792.26 end
'
' moderator/coolant - water in rod/channel
  h2o   5 den=0.7373 1 560.29 end
'
' channel/flow tube
  zirc2 6 1 560.29 end
'
end comp
'
' ------------------------------------------------------------------
read celldata
  latticecell squarepitch fueld=0.876  1
                          gapd= 0.894  4
                          cladd=1.026  2
                          pitch=1.295  3 end
  latticecell squarepitch fueld=0.876 11
                          gapd= 0.894 14
                          cladd=1.026 12
                          pitch=1.295 13 end
  centrmdata dan2pitch(11)=dancoff1 end centrmdata
  latticecell squarepitch fueld=0.876 21
                          gapd= 0.894 24
                          cladd=1.026 22
                          pitch=1.295 23 end
  centrmdata dan2pitch(21)=dancoff2 end centrmdata
  multiregion cylindrical left_bdy=reflected right_bdy=white end
      311   0.16555
      312   0.23412
      313   0.28674
      314   0.33110
      315   0.37018
      316   0.40551
      317   0.43800
       34   0.44700
       32   0.51300
```

```
       33   0.73063
    end zone
end celldata
'
' ---------------------------------------------------------------
read depletion
  $fuel flux $fgad
end depletion
'
' ---------------------------------------------------------------
read burndata
  power=specpow burn=daystoburn down=0 end
end burndata
'
' ---------------------------------------------------------------
read model
  BWR GE 10 × 10
'
read parm
  cmfd=1
  drawit=yes
  echo=yes
  epsinner=-1e-4
  fillmix=5
  run=yes
  xycmfd=4
end parm
'
read materials
  mix=$fuel pn=1 com='fuel'         end
  mix=2     pn=1 com='clad'         end
  mix=3     pn=2 com='coolant'      end
  mix=4     pn=0 com='gap'          end
  mix=5     pn=2 com='coolant'      end
  mix=6     pn=1 com='channel tube' end
  mix=$fgad pn=1 com='fuel with 5.0% Gd2O3' end
end materials
'
read geom
unit 1
com='fuel rod'
  cylinder 10 0.438
  cylinder 20 0.447
  cylinder 30 0.513
  media 1 1 10
  media 4 1 20 -10
  media 2 1 30 -20
  boundary 30
unit 2
com='fuel rod - edge'
  cylinder 10 0.438
  cylinder 20 0.447
  cylinder 30 0.513
  media 11 1 10
  media  4 1 20 -10
  media  2 1 30 -20
  boundary 30
unit 3
com='fuel rod - corner'
  cylinder 10 0.438
  cylinder 20 0.447
  cylinder 30 0.513
```

```
  media 21 1 10
  media  4 1 20 -10
  media  2 1 30 -20
  boundary 30
unit 4
com='fuel rod - with 5.0% Gd2O'
  cylinder  10 0.16555
  cylinder  20 0.23412
  cylinder  30 0.28674
  cylinder  40 0.33110
  cylinder  50 0.37018
  cylinder  60 0.40551
  cylinder  70 0.438
  cylinder  80 0.447
  cylinder  90 0.513
  media 311 1 10
  media 312 1 20 -10
  media 313 1 30 -20
  media 314 1 40 -30
  media 315 1 50 -40
  media 316 1 60 -50
  media 317 1 70 -60
  media   4 1 80 -70
  media   2 1 90 -80
  boundary 90
unit 5
com='water rod'
  cylinder 10 1.161
  cylinder 20 1.261
  media 5 1 10
  media 6 1 20 -10
  boundary 20
global unit 10
com='assembly'
  cuboid   10 14.32305 0.91695 14.32305 0.91695
  cuboid   20 14.52625 0.71375 14.52625 0.71375
  cuboid   30 15.24 0 15.24  0
' for rounded corners, bottom right to top left
  cylinder 11 0.9652 chord -x=1.88215 chord -y=1.88215 origin x=1.88215
y=1.88215 sides=16
  cylinder 12 1.1684 chord -x=1.88215 chord -y=1.88215 origin x=1.88215
y=1.88215 sides=16
  cuboid   13 1.88215  0.71375  1.88215  0.71375
  cylinder 21 0.9652 chord +x=13.35785 chord -y=1.88215 origin x=13.35785
y=1.88215 sides=16
  cylinder 22 1.1684 chord +x=13.35785 chord -y=1.88215 origin x=13.35785
y=1.88215 sides=16
  cuboid   23 14.52625 13.35785  1.88215  0.71375
  cylinder 31 0.9652 chord -x=1.88215 chord +y=13.35785 origin x=1.88215
y=13.35785 sides=16
  cylinder 32 1.1684 chord -x=1.88215 chord +y=13.35785 origin x=1.88215
y=13.35785 sides=16
  cuboid   33 1.88215  0.71375 14.52625 13.35785
  cylinder 41 0.9652 chord +x=13.35785 chord +y=13.35785 origin x=13.35785
y=13.35785 sides=16
  cylinder 42 1.1684 chord +x=13.35785 chord +y=13.35785 origin x=13.35785
y=13.35785 sides=16
  cuboid   43 14.52625 13.35785 14.52625 13.35785
' pin-by-pin construction
  hole 3 origin x= 1.79250 y= 1.79250
  hole 2 origin x= 3.08750 y= 1.79250
  hole 2 origin x= 4.38250 y= 1.79250
```

```
hole 2 origin x= 5.67750 y= 1.79250
hole 2 origin x= 6.97250 y= 1.79250
hole 2 origin x= 8.26750 y= 1.79250
hole 2 origin x= 9.56250 y= 1.79250
hole 2 origin x=10.85750 y= 1.79250
hole 2 origin x=12.15250 y= 1.79250
hole 3 origin x=13.44750 y= 1.79250
hole 2 origin x= 1.79250 y= 3.08750
hole 4 origin x= 3.08750 y= 3.08750
hole 1 origin x= 4.38250 y= 3.08750
hole 1 origin x= 5.67750 y= 3.08750
hole 4 origin x= 6.97250 y= 3.08750
hole 1 origin x= 8.26750 y= 3.08750
hole 4 origin x= 9.56250 y= 3.08750
hole 1 origin x=10.85750 y= 3.08750
hole 4 origin x=12.15250 y= 3.08750
hole 2 origin x=13.44750 y= 3.08750
hole 2 origin x= 1.79250 y= 4.38250
hole 1 origin x= 3.08750 y= 4.38250
hole 4 origin x= 4.38250 y= 4.38250
hole 1 origin x= 5.67750 y= 4.38250
hole 1 origin x= 6.97250 y= 4.38250
hole 1 origin x= 8.26750 y= 4.38250
hole 1 origin x= 9.56250 y= 4.38250
hole 1 origin x=10.85750 y= 4.38250
hole 1 origin x=12.15250 y= 4.38250
hole 2 origin x=13.44750 y= 4.38250
hole 2 origin x= 1.79250 y= 5.67750
hole 1 origin x= 3.08750 y= 5.67750
hole 1 origin x= 4.38250 y= 5.67750
hole 1 origin x= 8.26750 y= 5.67750
hole 1 origin x= 9.56250 y= 5.67750
hole 1 origin x=10.85750 y= 5.67750
hole 4 origin x=12.15250 y= 5.67750
hole 2 origin x=13.44750 y= 5.67750
hole 2 origin x= 1.79250 y= 6.97250
hole 4 origin x= 3.08750 y= 6.97250
hole 1 origin x= 4.38250 y= 6.97250
hole 1 origin x= 8.26750 y= 6.97250
hole 1 origin x= 9.56250 y= 6.97250
hole 1 origin x=10.85750 y= 6.97250
hole 1 origin x=12.15250 y= 6.97250
hole 2 origin x=13.44750 y= 6.97250
hole 2 origin x= 1.79250 y= 8.26750
hole 1 origin x= 3.08750 y= 8.26750
hole 1 origin x= 4.38250 y= 8.26750
hole 1 origin x= 5.67750 y= 8.26750
hole 1 origin x= 6.97250 y= 8.26750
hole 1 origin x=10.85750 y= 8.26750
hole 4 origin x=12.15250 y= 8.26750
hole 2 origin x=13.44750 y= 8.26750
hole 2 origin x= 1.79250 y= 9.56250
hole 4 origin x= 3.08750 y= 9.56250
hole 1 origin x= 4.38250 y= 9.56250
hole 1 origin x= 5.67750 y= 9.56250
hole 1 origin x= 6.97250 y= 9.56250
hole 1 origin x=10.85750 y= 9.56250
hole 1 origin x=12.15250 y= 9.56250
hole 2 origin x=13.44750 y= 9.56250
hole 2 origin x= 1.79250 y=10.85750
hole 1 origin x= 3.08750 y=10.85750
hole 1 origin x= 4.38250 y=10.85750
```

```
  hole 1 origin x= 5.67750 y=10.85750
  hole 1 origin x= 6.97250 y=10.85750
  hole 1 origin x= 8.26750 y=10.85750
  hole 1 origin x= 9.56250 y=10.85750
  hole 4 origin x=10.85750 y=10.85750
  hole 1 origin x=12.15250 y=10.85750
  hole 2 origin x=13.44750 y=10.85750
  hole 2 origin x= 1.79250 y=12.15250
  hole 4 origin x= 3.08750 y=12.15250
  hole 1 origin x= 4.38250 y=12.15250
  hole 4 origin x= 5.67750 y=12.15250
  hole 1 origin x= 6.97250 y=12.15250
  hole 4 origin x= 8.26750 y=12.15250
  hole 1 origin x= 9.56250 y=12.15250
  hole 1 origin x=10.85750 y=12.15250
  hole 4 origin x=12.15250 y=12.15250
  hole 2 origin x=13.44750 y=12.15250
  hole 3 origin x= 1.79250 y=13.44750
  hole 2 origin x= 3.08750 y=13.44750
  hole 2 origin x= 4.38250 y=13.44750
  hole 2 origin x= 5.67750 y=13.44750
  hole 2 origin x= 6.97250 y=13.44750
  hole 2 origin x= 8.26750 y=13.44750
  hole 2 origin x= 9.56250 y=13.44750
  hole 2 origin x=10.85750 y=13.44750
  hole 2 origin x=12.15250 y=13.44750
  hole 3 origin x=13.44750 y=13.44750
' water rods
  hole 5 origin x=8.915 y=8.915
  hole 5 origin x=6.325 y=6.325
  media 3 1 10 -13 -23 -33 -43
  media 3 1 13  11
  media 3 1 23  21
  media 3 1 33  31
  media 3 1 43  41
  media 6 1 20 -10 -13 -23 -33 -43
  media 6 1 13  12 -11
  media 6 1 23  22 -21
  media 6 1 33  32 -31
  media 6 1 43  42 -41
  media 5 1 30 -20
  media 5 1 13 -12
  media 5 1 23 -22
  media 5 1 33 -32
  media 5 1 43 -42
  boundary 30 48 48
end geom
'
read bnds
  all=mirror
end bnds
'
end data
end
'
=shell
  cp ft33f001.cmbined $RTNDIR/namelibrary
end
```

Appendix B: Representative BWR NESTLE Input

```
Representative BWR Zircaloy Core
read parameter
  xsecfile=XsecFile.xsec
  thfeedback=yes
  bocexpfile=ShuffleExp.txt
  geometry=cart
  thsolver=dfm
  quality=epri
  void=zf
  powerden=50.66
  t2n=yes
  longedit=yes
  depl_update=3
  accel=cheby
  chebymax=5
  diffusionmethod=fdm
  outers=100
  demand_conv=yes
  specshiftcorr=no
  therms=1
  deplete=yes
  thupdate=5
  microdeplete=no
  ratiohmfuel=0.881481
  sym=fourth
  eps_pres=5E-5
  inputedit=no
  printscreen=no
  output_format=new
  output_conv_data=no
end parameter

read edit
  kinf
  coolantden
  coolanttemp
  prel
  exp
  power  visit=yes gap=0.2 0.2 end visit
end edit

read heattransfer
  redistributeflow=mass
' total core flow rate Mlbm/hr
  mcore=15.375

' Bypass (Mlbm/hr) = 0.0205 * Massflow
  bypass=0.315

' Inlet coolant mass velocity (lb/hr-ft2) entering bottom fuel
' Calculated using PB mass flow rate and representative wetted area
  g=1474217

' At Pressure of 1035 psia from NIST
  rhovsat=2.3299
  tsat=548.84
  tinlet=527.485
  tinletmin=500
  tinletmax=550
```

```
' Saturation Energy of Coolant BTU/lbm from NIST
  uvsat=1192.0

' FITTING COEFFICIENTS FOR COOLANT LIQUID DENSITY VS. INTERNAL ENERGY
(COF_RHOWC)
  rho_vs_ufit  96.45734  -0.1949999 3.0895701E-4  -2.1894648E-7  end
rho_vs_ufit
' FITTING COEFFICIENTS FOR COOLANT LIQUID TEMP VS. INTERNAL ENERGY (COF_TCOL)
  t_vs_ufit  341.7741  -0.7333801  3.3770057E-3  -2.4074573E-6  end t_vs_ufit
' FITTING COEFFICIENTS FOR COOLANT INTERNAL ENERGY VS. TEMP (COF_UCOL)
  u_vs_Tfit  -4712.978  25.73904  -4.3827321E-2  2.6161042E-5  end u_vs_Tfit

end heattransfer

read fuelmech

' Density = 10.45 g/cc
  wc=1.0 wp=0.85 fiss_frac=0.975
  fuelden=652.37

'############## Peach Bottom TH parameters ########

  heff_vs_t 0.78363116E-01 -0.19203380E-04 0.73696720E-08 end heff_vs_t
  tavg_vs_lpd  530.2 99.429 0.0075 end tavg_vs_lpd
  tsurf_vs_lpd  530.2 99.429 0.0075 end tsurf_vs_lpd
  cp_vs_tfit 0.8110000193E-01 end cp_vs_tfit

'####################################################

  lattice_ids   1 2 3 4 5 6 7 end lattice_ids

'########## Lattices: ############
' 1: Peach Bottom Reflector (bottom + peripheral)
' 2: Peach Bottom Reflector (top)
' 3: Lower Natural Zone
' 4: Power Shaping Zone
' 5: Dominant Region
' 6: Vanishing Region (14 empty locations)
' 7: Upper Natueral Zone (14 empty locations)

  numfrods      2r0.0  3r92            2r78            end numfrods
  fuelfrac      2r0.0  3r0.23864       2r0.20232       end fuelfrac
  fpinrad       2r0.0  3r0.1732        2r0.1732        end fpinrad
  frodrad       2r0.0  3r0.2008        2r0.2008        end frodrad
  bunarea       2r0.25 3r0.25621       2r0.25621       end bunarea
  hydiam        2r0.5  3r0.03575       2r0.03575       end hydiam
  eqdiam        2r0.5  3r0.03575       2r0.03575       end eqdiam

  wtfri         2r1.0   3r0.57325      2r0.57325       end wtfri
  wtfro         2r1.0   3r0.57325      2r0.57325       end wtfro


'####################################################

' **** Orifice Loss Coefficient from Coolant Hydraulics Handbook *******

  losscoeffs 7r1.0 end losscoeffs
  losscoeffs_loc 0 0 0 0 0 0 0 end losscoeffs_loc
  orificecoeff  15.836  15.836  end orificecoeff
  orificecoeff_ids 1 2  end orificecoeff_ids
```

```
end fuelmech

' ########### Percent Power/Flow from Design Report ################

read burndata
pres=1035

burnup= 0    sm=eq xe=eq crod_id=1 pctpwr=100 bypass=0.315 tinlet=527.485 end
burnup= 2000 sm=eq xe=eq crod_id=2 pctpwr=100 bypass=0.315 tinlet=527.485 end
burnup= 4000 sm=eq xe=eq crod_id=3 pctpwr=100 bypass=0.315 tinlet=527.485 end
burnup= 6000 sm=eq xe=eq crod_id=4 pctpwr=100 bypass=0.315 tinlet=527.485 end
burnup= 8000 sm=eq xe=eq crod_id=5 pctpwr=100 bypass=0.315 tinlet=527.485 end
burnup=10000 sm=eq xe=eq crod_id=6 pctpwr=100 bypass=0.315 tinlet=527.485 end
burnup=12000 sm=eq xe=eq crod_id=7 pctpwr=100 bypass=0.315 tinlet=527.485 end
burnup=12800 sm=eq xe=eq crod_id=8 pctpwr=100 bypass=0.315 tinlet=527.485 end

end burndata

read geom
' BOUNDARY CONDITIONS
  inner=cyclic
  outer=zero
  up=zero
  down=zero
  orifice_id=117

' BUNDLE PITCHES
  bpitchx=6.0
  bpitchy=6.0

' X/Y/Z meshes
  deltax 13r6.0 end deltax
  deltay 13r6.0 end deltay
  bottomfuelnode=4
  topfuelnode=27
  deltaz 3r3.0 24r6.0 3r3.0 end deltaz
  figure 3r6 1r1 8r2 7r3 7r4 1r5 3r7 end figure

' Rotation for nodal ADF's
  rotation=217


' CRODS
  crload=bottomup

  crbank 1 17
  14.4  144   14.4  144   30.6  144
  144   144   144   144   144   144
  14.4  144   8.6   144   14.4  144
  144   144   144   144   144   144
  22.5  144   14.4  144   52.9
  144   144   144   144
  end crbank

  crbank 2 17
  144   144   144   144   144   144
  14.4  144   8.6   144   14.4  144
  144   144   144   144   144   144
  14.4  144   8.6   144   10.8  144
  144   144   144   144   144
  36.7  144   144.0 144
  end crbank
```

```
  crbank 3 17
  144   144   144   144   144   144
  144   14.4  144   8.6   144   144.0
  144   144   144   144   144   144
  144   8.6   144   14.4  144   144.0
  144   144   144   144   144
  144   14.4  144   144.0
  end crbank

  crbank 4 17
  144   14.4  144   8.6   144   144.0
  144   144   144   144   144   144
  144   14.4  144   14.4  144   144.0
  144   144   144   144   144   144
  144   14.4  144   46.8  144
  144   144   144   144
  end crbank

  crbank 5 17
  144.0 144   14.4  144   30.6  144
  144   144   144   144   144   144
  14.4  144   14.4  144   30.6  144
  144   144   144   144   144   144
  14.4  144   14.4  144   144.0
  144   144   144   144
  end crbank

  crbank 6 17
  144   144   144   144   144   144
  14.4  144   14.4  144   14.4  144
  144   144   144   144   144   144
  144.0 144   14.4  144   144.0 144
  144   144   144   144   144
  144.0 144   144.0 144
  end crbank

  crbank 7 17
  144   144   144   144   144   144
  144   137.9 144   0.0   144   126.7
  144   144   144   144   144   144
  144   144.0 144   144.0 144   144.0
  144   144   144   144   144
  144   8.6   144   144.0
  end crbank

  crbank 8 17
  144   119.7 144   14.4  144   38.7
  144   144   144   144   144   144
  144   137.9 144   144.0 144   119.7
  144   144   144   144   144   144
  144   137.9 144   144.0 144
  144   144   144   144
  end crbank


end geom


' FUEL TYPE <0--6><6----54><54----96><96----138><138--144>
'  1:         3       4         5         6         7
'  2:         3       5         5         6         7
```

```
read arrays
'###### Lower Blanket Region 0 - 6 inches ########
ara=1 nux=13 nuy=13 fill
  3 3 3 3 3 3 3 3 3 3 1 1
  3 3 3 3 3 3 3 3 3 3 1 1
  3 3 3 3 3 3 3 3 3 3 1 1
  3 3 3 3 3 3 3 3 3 3 1 1
  3 3 3 3 3 3 3 3 3 3 1 1
  3 3 3 3 3 3 3 3 3 3 1 1
  3 3 3 3 3 3 3 3 3 3 1 1
  3 3 3 3 3 3 3 3 3 1 1 0
  3 3 3 3 3 3 3 3 3 1 1 0 0
  3 3 3 3 3 3 3 3 1 1 0 0 0
  3 3 3 3 3 3 3 1 1 0 0 0 0
  1 1 1 1 1 1 1 0 0 0 0 0 0
  1 1 1 1 1 1 1 0 0 0 0 0 0 end fill

'###### PSZ/DOM Region 6 - 54 inches ########
ara=2 nux=13 nuy=13  fill
  5 5 5 5 5 5 5 5 5 5 4 1 1
  5 5 5 5 5 5 5 5 5 5 4 1 1
  5 5 5 5 5 5 5 4 5 5 4 1 1
  5 5 5 5 5 5 5 5 5 4 5 4 1 1
  5 5 5 5 4 5 5 5 5 5 5 1 1
  5 5 5 5 5 5 5 5 5 5 5 5 1 1
  5 5 5 5 5 5 5 5 5 5 5 4 1 1
  5 5 4 5 5 5 5 5 4 5 1 1 0
  5 5 5 4 5 5 5 4 5 1 1 0 0
  5 5 5 5 5 5 5 5 5 1 1 0 0 0
  4 4 4 4 5 5 4 1 1 0 0 0 0 0
  1 1 1 1 1 1 1 1 0 0 0 0 0 0
  1 1 1 1 1 1 1 0 0 0 0 0 0 0 end fill

'###### DOM Region 54 - 96 inches ########
ara=3 nux=13 nuy=13  fill
  5 5 5 5 5 5 5 5 5 5 5 1 1
  5 5 5 5 5 5 5 5 5 5 5 5 1 1
  5 5 5 5 5 5 5 5 5 5 5 5 1 1
  5 5 5 5 5 5 5 5 5 5 5 5 1 1
  5 5 5 5 5 5 5 5 5 5 5 5 1 1
  5 5 5 5 5 5 5 5 5 5 5 5 1 1
  5 5 5 5 5 5 5 5 5 5 5 5 1 1
  5 5 5 5 5 5 5 5 5 5 5 1 1 0
  5 5 5 5 5 5 5 5 5 5 1 1 0 0
  5 5 5 5 5 5 5 5 5 1 1 0 0 0
  5 5 5 5 5 5 5 5 1 1 0 0 0 0
  1 1 1 1 1 1 1 1 0 0 0 0 0 0
  1 1 1 1 1 1 1 1 0 0 0 0 0 0  end fill

'###### Vanishing Rod Region 96 - 138 inches ########
ara=4 nux=13 nuy=13  fill
  6 6 6 6 6 6 6 6 6 6 6 1 1
  6 6 6 6 6 6 6 6 6 6 6 6 1 1
  6 6 6 6 6 6 6 6 6 6 6 6 1 1
  6 6 6 6 6 6 6 6 6 6 6 6 1 1
  6 6 6 6 6 6 6 6 6 6 6 6 1 1
  6 6 6 6 6 6 6 6 6 6 6 6 1 1
  6 6 6 6 6 6 6 6 6 6 6 6 1 1
  6 6 6 6 6 6 6 6 6 6 6 1 1 0
  6 6 6 6 6 6 6 6 6 6 1 1 0 0
  6 6 6 6 6 6 6 6 6 1 1 0 0 0
```

```
  6 6 6 6 6 6 6 1 1 0 0 0 0
  1 1 1 1 1 1 1 1 0 0 0 0 0
  1 1 1 1 1 1 1 1 0 0 0 0 0 0  end fill

'###### Upper Blanket Region 138 - 144 inches ########
ara=5 nux=13 nuy=13  fill
  7 7 7 7 7 7 7 7 7 7 7 1 1
  7 7 7 7 7 7 7 7 7 7 7 1 1
  7 7 7 7 7 7 7 7 7 7 7 1 1
  7 7 7 7 7 7 7 7 7 7 7 1 1
  7 7 7 7 7 7 7 7 7 7 7 1 1
  7 7 7 7 7 7 7 7 7 7 7 1 1
  7 7 7 7 7 7 7 7 7 7 7 1 1
  7 7 7 7 7 7 7 7 7 7 1 1 0
  7 7 7 7 7 7 7 7 7 1 1 0 0
  7 7 7 7 7 7 7 7 1 1 0 0 0
  7 7 7 7 7 7 7 1 1 0 0 0 0
  1 1 1 1 1 1 1 1 0 0 0 0 0
  1 1 1 1 1 1 1 1 0 0 0 0 0 0 end fill

'###### Bottom Reflector Region ########
ara=6 nux=13 nuy=13  fill
  1 1 1 1 1 1 1 1 1 1 1 1 1
  1 1 1 1 1 1 1 1 1 1 1 1 1
  1 1 1 1 1 1 1 1 1 1 1 1 1
  1 1 1 1 1 1 1 1 1 1 1 1 1
  1 1 1 1 1 1 1 1 1 1 1 1 1
  1 1 1 1 1 1 1 1 1 1 1 1 1
  1 1 1 1 1 1 1 1 1 1 1 1 1
  1 1 1 1 1 1 1 1 1 1 1 1 0
  1 1 1 1 1 1 1 1 1 1 1 0 0
  1 1 1 1 1 1 1 1 1 1 0 0 0
  1 1 1 1 1 1 1 1 1 0 0 0 0
  1 1 1 1 1 1 1 1 0 0 0 0 0
  1 1 1 1 1 1 1 1 0 0 0 0 0 0  end fill

'###### Top Reflector Region ########
ara=7 nux=13 nuy=13  fill
  2 2 2 2 2 2 2 2 2 2 2 1 1
  2 2 2 2 2 2 2 2 2 2 2 1 1
  2 2 2 2 2 2 2 2 2 2 2 1 1
  2 2 2 2 2 2 2 2 2 2 2 1 1
  2 2 2 2 2 2 2 2 2 2 2 1 1
  2 2 2 2 2 2 2 2 2 2 2 1 1
  2 2 2 2 2 2 2 2 2 2 2 1 1
  2 2 2 2 2 2 2 2 2 2 1 1 0
  2 2 2 2 2 2 2 2 2 1 1 0 0
  2 2 2 2 2 2 2 2 2 1 1 0 0 0
  2 2 2 2 2 2 2 2 1 1 0 0 0 0
  1 1 1 1 1 1 1 1 1 0 0 0 0 0
  1 1 1 1 1 1 1 1 0 0 0 0 0 0 end fill

ara=17 nux=13 nuy=13 fill
 1  2  2  3  3  4  4  5  5  6  6 0 0
 7  8  8  9  9 10 10 11 11 12 12 0 0
 7  8  8  9  9 10 10 11 11 12 12 0 0
13 14 14 15 15 16 16 17 17 18 18 0 0
13 14 14 15 15 16 16 17 17 18 18 0 0
19 20 20 21 21 22 22 23 23 24 24 0 0
19 20 20 21 21 22 22 23 23 24 24 0 0
25 26 26 27 27 28 28 29 29  0  0 0 0
25 26 26 27 27 28 28 29 29  0  0 0 0
```

```
30 31 31 32 32 33 33  0  0  0  0 0 0
30 31 31 32 32 33 33  0  0  0  0 0 0
 0  0  0  0  0  0  0  0  0  0  0 0 0
 0  0  0  0  0  0  0  0  0  0  0 0 0 end fill

ara=117 nux=13 nuy=13 fill
' Orifice Loss Coeff Array
  1 1 1 1 1 1 1 1 1 1 1 0 0
  1 1 1 1 1 1 1 1 1 1 1 0 0
  1 1 1 1 1 1 1 1 1 1 1 0 0
  1 1 1 1 1 1 1 1 1 1 1 0 0
  1 1 1 1 1 1 1 1 1 1 1 0 0
  1 1 1 1 1 1 1 1 1 1 1 0 0
  1 1 1 1 1 1 1 1 1 1 1 0 0
  1 1 1 1 1 1 1 1 1 1 0 0 0
  1 1 1 1 1 1 1 1 1 0 0 0 0
  1 1 1 1 1 1 1 1 0 0 0 0 0
  1 1 1 1 1 1 1 0 0 0 0 0 0
  0 0 0 0 0 0 0 0 0 0 0 0 0
  0 0 0 0 0 0 0 0 0 0 0 0 0 end fill

ara=217 nux=13 nuy=13 fill
' No Rotation
  0 1 0 1 0 1 0 1 0 1 0 0 0
  3 2 3 2 3 2 3 2 3 2 3 0 0
  0 1 0 1 0 1 0 1 0 1 0 0 0
  3 2 3 2 3 2 3 2 3 2 3 0 0
  0 1 0 1 0 1 0 1 0 1 0 0 0
  3 2 3 2 3 2 3 2 3 2 3 0 0
  0 1 0 1 0 1 0 1 0 1 0 0 0
  3 2 3 2 3 2 3 2 3 2 0 0 0
  0 1 0 1 0 1 0 1 0 0 0 0 0
  3 2 3 2 3 2 3 2 0 0 0 0 0
  0 1 0 1 0 1 0 0 0 0 0 0 0
  0 0 0 0 0 0 0 0 0 0 0 0 0
  0 0 0 0 0 0 0 0 0 0 0 0 0 end fill

end arrays
```

Appendix C: Sample LWROpt Input

```
'DEBUG' 0 0 1 0 1 2 / debug_sample_flag, debug_archive_flag, debug_OF_flag,
debug_cost_flag, nes_iter_flag, crp_stat_flag
'CR.OUT' 2 1 / cr_output_flag (0 = nothing, 1 = summary to screen, 2 =
everything to screen, 3 = everything process output file), cr_plot_flag (1 =
plot, 0 = don't plot)

'REAC.TYP' 'BWR'
'CYC' 1 13 1/ Cycle Data [# of cycles to optimize (n_cyc_opt), first cycle #,
first_cyc_opt_flag (1 = yes, 0 = no)]

'OPT' 'CRP' / Optimization Method [PSA (Parallel Simulated Annealing), MAN,
CRP, RUN]

'DEP.CYC' 1 / Depletion option for optimized cycles (n_cyc_opt) [0 = use
original depletion, 1 = CR optimization, 2 = Haling depletion]
'EXP.STP' 2000. / Depletion step size for each cycle optimized if CR
optimization used

'NES.ITER' 250 0 / max_nes_iter (maximum number of iterations used for NESTLE
calculations), use nonconverged solutions [0=no, 1=yes]

'INP.EDT' 2 / Input edit flag (0 = none, 1 = just in summary file, 2 = all)
'RES' 1 / Use restart files flag  for each cycle to be optimized (0 = don't
use, 1 = use)

'CHG'     1 2 3 4 5 6 7 8 9 10 / Change Types to Use [old shuffle, new old
swap, # fresh change, new type (switch, change, add),CRP change]
'CHG.GRP' 1 2 3 4 5 6 7 8 9 10 / Groups used for variable sample
probabilities (if a change type converges the probability is distributed
among the other change types in the group if there are any)

'OF' 1 0 / OF_nan_flag, OF_mix_opt (0 = dont use initial solutions in ST_DEV
calc, 1 = use initial solutions)

'CON' 7 0 2.0/ # of constraints, constraint weight multiplier flag, target
T=0 constraint weight multiplier
     '$    '  0.0       10.0   / Constraints Parameters
[constraint,limit,weight] constraints ($,A_EX,N_EX,RPF,K) CPR,TMOL,STAB
     'K-   '  1.0      150.0   /
     'K+   '  1.001    130.0   /
     'A_EX'  55.0       1.0   / (GWD/MTU)
     'N_EX'  65.0       1.0   / (GWD/MTU)
     'RPF2'  1.6       30.0   /
     'RPF3'  2.0       10.0   /

'CYC.LEN' 30  / shutdown length (days) for each cycle being optimized
'COST' .34 .15/ efficiency, carrying charge (annual interest rate)

'NEW.TYP' 9 2 0/ [max # new types, cycle 1 new type, max assembly number for
sampling new fuel from (0 = # of new types entered)]

'CR.NOTCH' 48 2 1 /

/ calculate energy of 18 mo cycle
'ENERGY' 251860.01 / Energy production for cycles to be optimized (MWD) (1
number followed by '/' -> all cycles same, otherwise specify for each cycle)
```

```
'POWER' 100.0 100.0 0.315 527.485 / Parameters used in cr optimization and
haling depletion cases (pctpwr, pctflow, bypass, tinlet)

'SORT' 'EXP' / Parameter to use for sort to generate original LP_oper ['KIN'
or 'EXP']

'ARCHIVE' 'NEW' 20 20 40 30 / Archive method ('NEW' = new inventory),
[idividual and combined] archive size (width, depth)

'RAND' 1000 1000000 /# to add to all random seeds, number of random numbers
to generate per process

'SOL.INI' 0 0 / Initial Solution Parameters [# of fresh to add, number of
changes to make to LP, # to add to all random seeds]

'DIR'
'/home/ngeorge3/ATF_BWR/Optimize_BWR/TheDesign/ControlBladeOpt/Zirc/Zirc_notc
h3/' 'representative_bwr/'
'/tmp/ngeorge3/ATF_BWR/Optimize_BWR/TheDesign/ControlBladeOpt/Zirc/Zirc_notch
3/Run_Files_representative/' / [project dir, model dir, run cycle dir,
process base run dir name]
'INP' 'representative' 'representative.inp' 0 0/ [reactor name, Input File
for Cycle N-1, assembly input (1 = yes), cr_input_flag]
'NES.EXE' '/home/ngeorge3/NESTLE/scale_dev/build_scale_dev/src/nestle/'
'nestle' 1 18 / Path for Nestle Executable [original path, exe name, copy
flag (0 = no copy, 1 = run path, 2 = path_proc),output_num_len]
'OUT' 2
'/home/ngeorge3/ATF_BWR/Optimize_BWR/TheDesign/ControlBladeOpt/Zirc/Zirc_notc
h3/Output_ representative /' 'scr_out' / [screen print option, base output
file location, name, ]
'SUMMARY'
'/home/ngeorge3/ATF_BWR/Optimize_BWR/TheDesign/ControlBladeOpt/Zirc/Zirc_notc
h3/Output_ representative /' 'Summary.out' 'Summary_full.out' 'T_stats_out.m'
'hist_stats_out.m' 'archive.out' / [summary_path, summary file name]

'PLOT.INFO' 1 'gnuplot'
'/home/ngeorge3/ATF_BWR/Optimize_BWR/TheDesign/ControlBladeOpt/Zirc/Zirc_notc
h3/plot_dir_ representative /' 'plot_script' 'plot_data'
'/home/kottinge/BWR_OPT/LiberationSerif-Regular.ttf,11'
'/home/kottinge/BWR_OPT/LiberationSerif-Regular.ttf,12' 2 / [plot flag,
gnuplot path, script base name, data file base name, font, mp_font,
mp_update]

'DEL.FILE' 0 / Output file delete flag (1 = delete, 0 = keep)

'PSA.STP' 10 10 0 0 / n_init_iter, n_iter, Cooling step length flag (0 = each
process runs n trials, 1 = average of n trials run over all processes)
[Cooling step 1, >1]
'PSA.CONV' 1 0 100 1 / PSA convergence criteria [1 (# consecutive CS, # of
accepts per CS), 2 (# of steps without OF decrease), 3 (maximum # cooling
steps)]
'PSA.TEMP' 2. 1.  .5   5  .3 .25 .2 .15 .1  / alpha, lambda, std_cutoff,
n_std_avg, (std_weights if n_std_avg > 1)
'PSA.INI' 1 -1 / init flag, dist flag [-1 = keep current solution, 0 = all
procs get best, 1 = dist n_procs best solutions (duplicate if necessary)]
'PSA.RES' 1000000 / n_step_res, # of iterations between restarts (sampling
from best solutions instead of current solutions)
'PSA.MIX' 0  1.05  .25 -1.  2 1 1/ [psa_mix_flag (0= standard, 1 = limits, 2
= always), mix_percent_lim, mix_acc_lim, mix_inc_lim, n_archive_samp (array
of # of solutions to select from each archive level) ]
```

```
'SAMP.PR' 0 / sample prob flag [0 = use constant sample prob [sample
probabilities for each change type (equal if not entered) will be weighted to
sum to 1]
                                  1 = decrease prob as accept prob --> 0 (#
cooling steps with 0 accepts for convergence, # step used to decrease prob to
0 linearly),
                                  2 = fully variable based on input parameters]

'SAMP.CYC' 1. / Sample probabilty for each cycle being optimized (one number
> all same)

'TIME' 1 / time flag (0 = runtime for each iteration given, 1 = runtime since
start of cooling step given)

*'TYP.REP'     / specify types to replace and replacing type for future
cycles (old type, new type)

'FUEL.TIME' 15. 12. 9. 3.   15./ Time before cycle starts for expense
(months) [ore, conv, enr, fab (and gad)]; carrying charge (%)
'FUEL.COST' 42.25  10.50 10.0  100000. 10000. / ore cost ($/lb U3O8),
conversion cost ($/kg UF6), SWU cost ($/SWU), fab cost ($/assembly), gad cost
($/kg)
'FUEL.LOSS' 0.0 .5 0.0 .5 / Fuel losses (%) (mining, conversion, enrichment,
fabrication
'FUEL.ENR' .711 .25/ feed enrichment, tails enrichment

'CR.OPT' 0 1/ cr_opt_flag (0 = old method, 2 = new method, 1 = haling (don't
use)), cr_ini_flag (1 = always start all rods out, otherwise use previous CR
positions)
'CR.ITER' 200 200 / max cr calc iter (initial, noninitial)
'CR.KEFF' 1.0000 1.0010 1.0000 1.0010

'CR.PARM' 2 3 / [cr_ini_flag (only 2), cr_manual_flag (1 = enter entire CRP
every step, 2 = Change 1 CR at a time, 3 = check 'crd_flag' file each
iteration for cr_manual_flag, 4 = 3 and prompt for cr_manual_flag if solution
not found)]

*'CR.PREF' 7 8 8 8 / not used

'CR.STEP' .04 .5 / (min, max) CR move size, fraction of range
'CR.DEEP' 0.1 / fraction withdrawn for preferred deep insertion

'CR.BND' .3333 .6667 / Fractional values for boundaries between shallow,
intermediate, deep insertions

'CR.RING' 1.0 1.0 1.0 /

'CRD.1ST' 3

'CRD.CVC' 3.01100  2.01100  3.02100  2.03100  3.05100  2.07100
          4.01100  1.01100  4.02100  1.02100  4.05100  1.05100
          3.03100  2.02100  3.04100  2.04100  3.07100  2.08100
          4.03100  1.03100  4.04100  1.04100  4.06100  1.07100
          3.06100  2.05100  3.08100  2.06100  3.09100     0
          4.07100  1.06100  4.08100  1.08100     0        0   /

'END'
```

VITA

Nathan Michael George was born March 16th, 1988 in Erie, Pennsylvania to the parents of Michael and Kathi George. He is the youngest of four siblings including one older brother, Andrew, and two older sisters, Rachel and Maura. Nathan graduated from McDowell High School in 2006 and proceeded to attend The Pennsylvania State University in University Park, Pennsylvania. In May of 2010, he completed his Bachelor of Science in nuclear engineering with a minor in Spanish language and culture. After obtaining an internship at Oak Ridge National Laboratory in the summer of 2010, Nathan began graduate school at The University of Tennessee in Knoxville, Tennessee as a research assistant under Dr. Ivan Maldonado. His research, in the field of accident tolerant fuel, was funded jointly by Oak Ridge National Laboratory and The University of Tennessee. Nathan completed his Master of Science in December of 2011 and Doctor of Philosophy in May of 2015, both in nuclear engineering.